

ELECTROSPUN CARBON NANOFIBERS DECORATED NiO/C FOR
HIGH-PERFORMANCE SUPERCAPACITOR ELECTRODES



SUCHUNYA WONGPRASOD

A Thesis Submitted in Partial Fulfillment of the Requirements for the

Degree of Master of Science in Applied Physics

Suranaree University of Technology

Academic Year 2024

การเพิ่มประสิทธิภาพขั้วไฟฟ้าที่เป็นเส้นในนาโนคาร์บอนด้วยอนุภาค
นิกเกิลออกไซด์สำหรับขั้วไฟฟ้าตัวเก็บประจุยิ่งยวดประสิทธิภาพสูง



นางสาวสุชัญญา วงษ์ประเสริฐ

วิทยานิพนธ์นี้เป็นส่วนหนึ่งของการศึกษาตามหลักสูตรปริญญาวิทยาศาสตรมหาบัณฑิต

สาขาวิชาฟิสิกส์

มหาวิทยาลัยเทคโนโลยีสุรนารี

ปีการศึกษา 2567

ELECTROSPUN CARBON NANOFIBERS DECORATED NiO/C FOR HIGH-PERFORMANCE SUPERCAPACITOR ELECTRODES

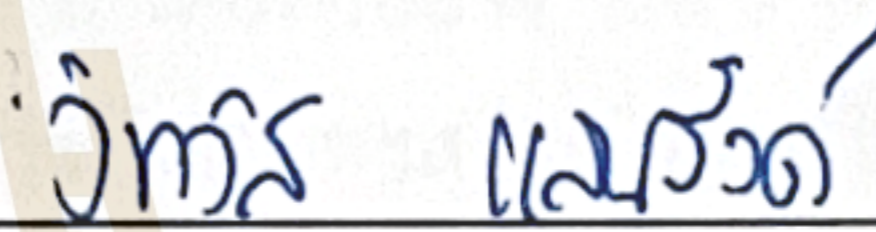
Suranaree University of Technology has approved this thesis submitted in partial fulfillment of the requirements for a Master's degree.

Thesis Examining Committee



(Dr. Wiwat Nuansing)

Chairperson



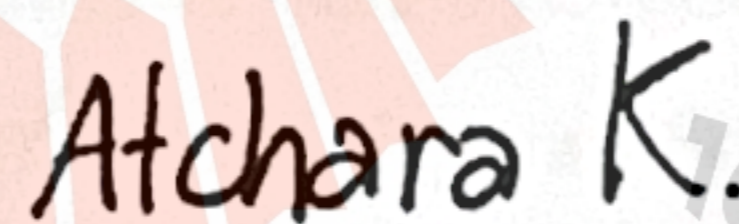
(Assoc. Prof. Dr. Wittawat Saenrang)

Member (Thesis Advisor)



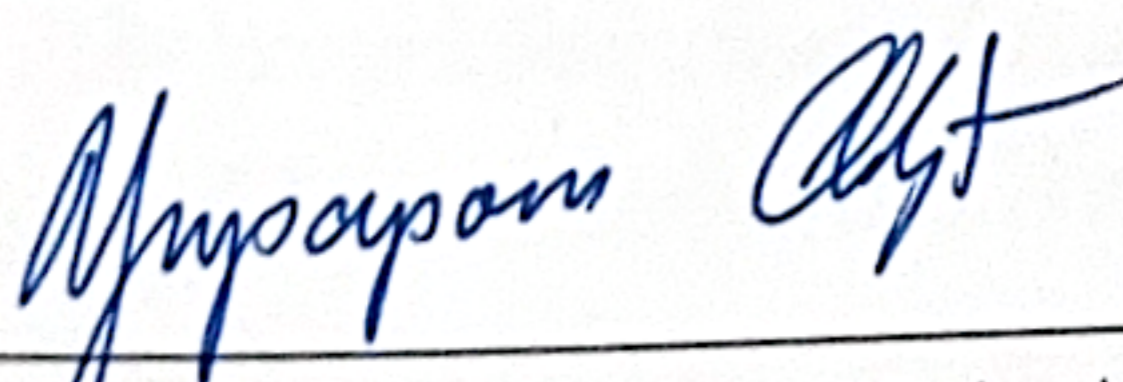
(Dr. Monchai Jitvisate)

Member



(Dr. Atchara Khamkongkaeo)

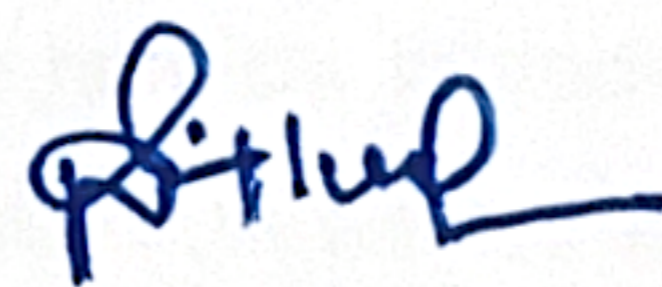
Member



(Assoc. Prof. Dr. Yupaporn Ruksakulpiwat)

Vice Rector for Academic Affairs

and Quality Assurance



(Prof. Dr. Santi Maensiri)

Dean of Institute of Science

สุชัญญา วงษ์ประเสริฐ : การเพิ่มประสิทธิภาพขั้วไฟฟ้าที่เป็นเส้นใยนาโนคาร์บอนด้วยอนุภาคนิกเกิลออกไซด์สำหรับขั้วไฟฟ้าของตัวเก็บประจุยิ่งยวดประสิทธิภาพสูง (ELECTROSPUN CARBON NANOFIBERS DECORATED NiO/C FOR HIGH-PERFORMANCE SUPERCAPACITOR ELECTRODES)

อาจารย์ที่ปรึกษา : รองศาสตราจารย์ ดร.วิทวัส แสนรงค์, หน้า 75 หน้า.

คำสำคัญ : ตัวเก็บประจุยิ่งยวด/ เส้นใยนาโนคาร์บอน/ นิกเกิลออกไซด์/ นาโนคอมโพสิต/ อิเล็กโตรสปินนิง

งานวิจัยนี้มุ่งเน้นการพัฒนาขั้วไฟฟ้าสำหรับตัวเก็บประจุยิ่งยวดที่มีสมรรถนะสูง โดยการสังเคราะห์เส้นใยนาโนคาร์บอน (Carbon nanofibers (CNFs)) ที่ผสมร่วมกับคอมโพสิตของนิกเกิลออกไซด์, โลหะนิกเกิล และคาร์บอน (NiO/C NPs) โดยตัวอย่าง CNFs ที่ตกแต่งด้วยอนุภาคนาโน NiO/C NPs (CNFs-NiO/C NPs) ถูกผลิตด้วยวิธีอิเล็กโตรสปินนิงของโพลีอะคริโลไนไตรล์ (Polyacrylonitrile (PAN)) และผ่านกระบวนการให้ความร้อนต่อเนื่อง สำหรับการเตรียม NiO/C NPs ใช้วิธีโซลโวเทอร์มอล และนำมาผสมลงในโครงสร้างของเส้นใยนาโนคาร์บอน ในอัตราส่วนโดยน้ำหนักที่แตกต่างกัน ได้แก่ 0 5 10 และ 15 %wt เทียบกับน้ำหนักของ PAN ซึ่งคุณสมบัติทางโครงสร้าง รูปร่างสัณฐานวิทยา และองค์ประกอบต่าง ๆ ของวัสดุถูกวิเคราะห์โดยใช้เทคนิคต่าง ๆ ได้แก่ กล้องจุลทรรศน์อิเล็กตรอนแบบส่องกราดชนิดปล่อยอิเล็กตรอนด้วยสนามไฟฟ้า (Field Emission Scanning Electron Microscopy (FESEM)), กล้องจุลทรรศน์อิเล็กตรอนแบบส่องผ่าน (Transmission Electron Microscopy (TEM)), การวิเคราะห์การเลี้ยวเบนของรังสีเอกซ์ (X-ray Diffraction (XRD)), การวิเคราะห์ด้วยสเปกโทรสโกปีอินฟราเรดแบบฟูเรียร์ทรานส์ฟอร์ม (Fourier-Transform Infrared Spectroscopy (FTIR)), การวิเคราะห์สเปกโทรสโกปีรามาน (Raman Spectroscopy), สเปกโทรสโกปีโฟโตอิเล็กตรอนรังสีเอกซ์ (X-ray Photoelectron Spectroscopy (XPS)), การวิเคราะห์สเปกโทรสโกปีการดูดกลืนรังสีเอกซ์ (X-ray Absorption Spectroscopy (XAS)) และการวิเคราะห์พื้นที่ผิวเฉพาะด้วยวิธีบรุนเนาเออร์-เอมเมตต์-เทลเลอร์ (Brunauer-Emmett-Teller (BET)) โดยผลการวิเคราะห์ยืนยันการรวมตัวกันของนิกเกิลออกไซด์และโลหะนิกเกิลภายในโครงข่ายของเส้นใยนาโนคาร์บอน ซึ่งนำไปสู่การเพิ่มพื้นที่ผิวจำเพาะ ความพรุน และพื้นที่ที่สามารถเกิดปฏิกิริยารีดอกซ์ได้สำหรับการประเมินคุณสมบัติทางไฟฟ้าเคมีได้ดำเนินการโดยใช้เทคนิคไซคลิกโวลแทมเมตรี (Cyclic Voltammetry (CV)), กัลวานอสแตติก ชาร์จ-ดิสชาร์จ (Galvanostatic Charge-Discharge (GCD)) และอิเล็กโตรเคมีคัลอิมพีแดนซ์สเปกโทรสโกปี (Electrochemical Impedance Spectroscopy (EIS)) ภายใต้ระบบสามขั้ว พร้อมใช้สารละลายอิเล็กโทรไลต์เป็นโพแทสเซียมไฮดรอกไซด์ (KOH) ที่มีความเข้มข้น 2 โมลาร์ ผลการทดลองพบว่า ขั้วไฟฟ้าเส้นใยนาโนคาร์บอนที่มี NiO/C NPs อยู่ 15 %wt (CNFs-15NiO/C NPs) แสดงค่าความจุจำเพาะสูงสุดที่ 474 F g^{-1} ที่ความหนาแน่นกระแส 0.5 A g^{-1} ในขณะที่ขั้วไฟฟ้าเส้นใยนาโนคาร์บอนที่ไม่มี NiO/C NPs รวมอยู่ด้วย แสดงค่าความจุจำเพาะที่ต่ำที่สุด

SUCHUNYA WONGPRASOD : ELECTROSPUN CARBON NANOFIBERS DECORATED
NiO/C FOR HIGH-PERFORMANCE SUPERCAPACITOR ELECTRODES, THESIS AD-
VISOR : ASSOCIATE PROFESSOR WITTAWAT SAENRANG, Ph.D. 75 PP.

Keywords: SUPERCAPACITOR/ CARBON NANOFIBERS/ NiO/ NANOCOMPOSITE/
ELECTROSPINNING

This study focuses on the development of high-performance supercapacitor electrodes through the synthesis of carbon nanofibers (CNFs) integrated with a composite of nickel oxide, metallic nickel, and carbon (NiO/C NPs). The CNFs decorated with NiO/C nanoparticles (CNFs–NiO/C NPs) were fabricated via electrospinning of polyacrylonitrile (PAN), followed by thermal treatment. NiO/C NPs were prepared using a solvothermal method and incorporated into the CNFs at varying weight ratios of 0, 5, 10, and 15 wt% relative to the PAN weight. Structural, morphological, and compositional properties were examined using Field Emission Scanning Electron Microscopy (FESEM), Transmission Electron Microscopy (TEM), X-ray Diffraction (XRD), Fourier-Transform Infrared Spectroscopy (FTIR), Raman Spectroscopy, X-ray Photoelectron Spectroscopy (XPS), X-ray Absorption Spectroscopy (XAS), and Brunauer–Emmett–Teller (BET) surface area analysis. The results confirmed the incorporation of crystalline NiO and metallic Ni within the CNFs, resulting in increased surface area, porosity, and redox-active sites. For electrochemical characterization, Cyclic Voltammetry (CV), Galvanostatic Charge and Discharge (GCD), and Electrochemical Impedance Spectroscopy (EIS) were constructed in a three-electrode system with 2 M KOH electrolyte. The CNFs with NiO/C NPs 15 %wt (CNFs-15NiO/C NPs) composite electrode shows the highest specific capacitance, achieving a specific capacitance of 474 F g^{-1} , whereas the CNFs-Bare electrode, which lacked NiO/C incorporation, showed the lowest specific capacitance of 266 F g^{-1} at a current density of 0.5 A g^{-1} . In addition, the CNFs-15NiO/C NPs electrode demonstrated outstanding cycling stability with 103% capacitance retention after 1000 cycles. These superior electrochemical behaviors are attributed to the combination of electric double-layer capacitance from CNFs, pseudocapacitance from NiO enhanced conductivity from metallic Ni, and enhanced porosity and surface area within CNFs-15NiO/C NPs. These findings demonstrate the potential of CNFs–NiO/C nanocomposites as efficient and durable electrode materials for next-generation energy storage applications.

School of Physics
Academic Year 2024

Student's Signature _____
Advisor's Signature _____

ACKNOWLEDGEMENTS

Initially, I wish to convey my sincere appreciation to Associate Professor Dr. Wittawat Saenrang, my project supervisor, for affording me with the opportunity to work on this project, as well as guidance, support, and encouragement that motivates me to complete this project. In addition, he has also assisted me in improving my critical thinking, time management, cooperation, and presentation skills.

I would like to extend my heartfelt thanks to Prof. Santi Maensiri and Assoc. Prof. Worawat Meevasana for their support and for facilitating access to laboratory facilities and electrochemical measurement systems, all of which were essential to the successful execution of this research.

Thank you to Mr. Nantawat Tanapongpisit and Dr. Peerawat Laohana, members of the "WSRG", who assisted me, provided me with guidance on all the equipment for this project, and supported me whenever I felt discouraged. I am very fortunate to have the chance to work with both of you.

I would like to express my sincere gratitude to Prof. Chung Wung Bark and his research team for synthesizing and providing the samples used in this study. I am also thankful for the valuable opportunity to participate in a two-month (from 10 April - 14 June 2025) research training program in South Korea, where I was able to gain hands-on experience in the synthesis of materials under their guidance.

I would also like to extend my appreciation to the Development and Promotion of Science and Technology (DPST) scholarship, which helps fund research in Thailand. I would never have been able to do this without their generous financial support.

Finally, I wish to acknowledge my family members who have always been by my side. Thank you, Mr. Rapeepat Yodsungnoen, for facilitating work and providing me with so much assistance and support. Thank you to all of my friends who have assisted me in reducing work-related stress. I would not be able to exist without them, and I would not be here today if it were not for them.

Suchunya Wongprasod

CONTENTS

	Page
ABSTRACT IN THAI	I
ABSTRACT IN ENGLISH	III
ACKNOWLEDGEMENTS	IV
CONTENTS	VII
LIST OF TABLES	IX
LIST OF FIGURES	X
CHAPTER	
I INTRODUCTION	1
II LITERATURE REVIEW	5
2.1 Supercapacitors	5
2.1.1 Electric Double Layer Capacitors (EDLCs)	7
2.1.2 Pseudocapacitors (PCs)	7
2.1.3 Hybrid Capacitors	8
2.2 Active Material	9
2.2.1 Materials with Electric Double-Layer Capacitance	10
2.2.2 Materials with Pseudocapacitance	10
2.3 Carbon Nanofibers (CNFs)	11
2.4 Transition Metal Oxide-Based Electrode Material	14
2.5 Electrospinning method	18
2.6 Electrolyte	19
III RESEARCH METHODOLOGY	22
3.1 Synthesis of Nickel Oxide Composite with Carbon Nanoparticles (NiO/C NPs)	22
3.2 Preparation of Carbon Nanofibers Decorated with NiO/C (CNFs- NiO/C NPs)	23
3.3 Preparation of Working Electrode	24
3.4 Basic characterization.	25
3.4.1 Field Emission Scanning Electron Microscope (FE-SEM)	25
3.4.2 Transmission Electron Microscope (TEM)	26

CONTENTS (Continued)

	Page
3.4.3 X-ray Diffraction (XRD)	27
3.4.4 Fourier-Transform Infrared Spectroscopy (FTIR)	27
3.4.5 Raman Spectroscopy (Raman)	28
3.4.6 X-ray Absorption Spectroscopy (XAS)	28
3.4.7 X-ray Photoelectron spectroscopy (XPS)	29
3.4.8 Brunauer-Emmett-Teller (BET)	30
3.5 Electrochemical characterization	30
3.5.1 Cyclic voltammetry (CV)	31
3.5.2 Galvanostatic charge-discharge (GCD)	32
3.5.3 Electrochemical impedance spectroscopy (EIS)	33
IV RESULTS AND DISCUSSION	35
4.1 Basic Characterization	35
4.2 Electrochemical Characterizations	48
V CONCLUSION AND RECOMMENDATION	57
REFERENCES	60
CURRICULUM VITAE	78

LIST OF TABLES

Table		Page
2.1	Recent CNFs and CNFs/TMO composite Electrode materials for EDLC supercapacitors.	15
2.2	Recent NiO-carbon composite for supercapacitor electrode materials.	17
4.1	Interplanar distances (d-spacings) for electron diffraction patterns of NiO/C NPs and CNFs-10NiO/C NPs.	39
4.2	Specific surface area and average pore size of sample.	48
4.3	the specific capacitance value of CNFs-Bare, CNFs-5NiO/C NPs, CNFs-15NiO/C NPs, and CNFs-15NiO/C NPs electrode at various current densities of 0.5–5 A g ⁻¹	53

LIST OF FIGURES

Figure		Page
2.1	The Ragone energy storage device plot (Permatasari et al., 2021)	5
2.2	Diagram of supercapacitor components (Smith et al., 2020). . .	6
2.3	Diagram of electric double layer formation on the interfaces of both electrodes (Beguin et al., 2014).	7
2.4	Diagram of charge storage mechanism of pseudocapacitors (Tyagi and Gupta, 2015).	8
2.5	Diagram of different active materials used as electrode for supercapacitors (C. Lee et al., 2019).	9
2.6	Frequently used polymer as precursors for carbon nanofibers (B.-S. Lee and Yu, 2020).	12
2.7	Stabilization and carbonization mechanism of PAN nanofibers (Konstantopoulos et al., 2020).	14
2.8	Electrospinning diagram (Mori et al., 2015).	19
2.9	Type of electrolytes for supercapacitors (B.-S. Lee and Yu, 2020).	20
3.1	Schematic of NiO/C MPs and NPs preparation (Nguyen and Bark, 2020).	23
3.2	Schematic of carbon nanofibers decorated with NiO/C preparation.	24
3.3	Schematic of CNFs-NiO/C NPs electrode preparation.	25
3.4	A schematic of scanning electron microscope (SEM) and transmission electron microscope (TEM) diagram	26
3.5	Infrared spectroscopy measures the interaction of infrared radiation with matter (Bruker Corporation, n.d.).	28
3.6	Schematic of the principle of XAS (Fracchia et al., 2018).	29
3.7	Schematic of the principle of XPS (Vandenbroucke, 2015).	30
3.8	Principles of the BET methods (Particle Technology Labs, n.d.). .	31
3.9	The CV curves of NiO/C NPs electrode at various scan rates of 5–70 mV s ⁻¹	32

LIST OF FIGURES (Continued)

Figure		Page
3.10	The GCD curves of NiO/C nanoparticles (NiO/C NPs) and microparticles (NiO/C MPs) electrodes at a current density of 0.5 A g^{-1}	33
3.11	Specific capacitance calculated from galvanostatic charge-discharge.	33
3.12	The Nyquist plot diagram with key regions labelled (Mevada and Mukhopadhyay, 2023).	34
4.1	FE-SEM images of (a) CNFs-Bare, (b) CNFs-5NiO/C NPs, (c) CNFs-10NiO/C NPs and (d) CNFs-15NiO/C NPs at a magnification of 10 kx with the insets of (a)-(d) representing their FESEM images at 50kx magnification.	35
4.2	Histogram of diameter distribution of (a) CNFs-Bare, (b) CNFs-5NiO/C NPs, (c) CNFs-10NiO/C NPs and (d) CNFs-15NiO/C NP.	36
4.3	TEM images of (a) CNFs-Bare, (b) CNFs-5NiO/C NPs, (c) CNFs-10NiO/C NPs and (d) CNFs-15NiO/C NP with the insets of (a)-(d) representing their higher magnification of TEM images.	37
4.4	(a) The TEM image of CNFs-15NiO/C NPs at the magnification of 120kx, and (b) the HRTEM image of CNFs-15NiO/C NPs along with the lattice spacing.	38
4.5	SAED rings of (a) NiO/C NPs, (b) CNFs-Bare, (c) CNFs-5NiO/C NPs, (d) CNFs-15NiO/C NPs, and (e) CNFs-15NiO/C NPs.	39
4.6	EDS spectra of a) CNFs-Bare, and CNFs-15NiO/C NPs with their element.	40
4.7	EDS mapping of CNFs-15NiO/C NPs with their element.	40
4.8	XRD pattern of NiO/c NPs, CNFs-Bare, CNFs-5NiO/C NPs, CNFs-10NiO/C NPs and CNFs-15NiO/C NPs.	41
4.9	FT-IR spectra of NiO/c NPs, CNFs-Bare, CNFs-5NiO/C NPs, CNFs-10NiO/C NPs and CNFs-15NiO/C NPs.	42
4.10	Raman spectra of NiO/c NPs, CNFs-Bare, CNFs-5NiO/C NPs, CNFs-10NiO/C NPs and CNFs-15NiO/C NPs.	43
4.11	the survey XPS spectra of CNFs-Bare, and CNFs-15NiO/C NPs.	44

LIST OF FIGURES (Continued)

Figure		Page
4.12	XPS high resolution spectra at (a) Ni 2p, and (b) O 1s (c) N 1s, and (d) C 1s regions of CNFs-Bare, CNFs-5NiO/C NPs, CNFs-10NiO/C NPs and CNFs-15NiO/C NPs.	46
4.13	Ni K-edge XANES of NiO/C NPs, CNFs-Bare, CNFs-5NiO/C NPs, CNFs-10NiO/C NPs and CNFs-15NiO/C NPs compare with Ni foil and NiO standard.	47
4.14	The N ₂ adsorption–desorption isotherms of CNFs-Bare, and CNFs-15NiO/C NPs.	48
4.15	CV curves of (a) CNFs-Bare, (b) CNFs-5NiO/C NPs, (c) CNFs-10NiO/C NPs, and (d) CNFs-15NiO/C NPs electrode at various scan rates of 2–100 mV s ⁻¹	49
4.16	CV curves of CNFs-Bare, CNFs-5NiO/C NPs, CNFs-15NiO/C NPs, and CNFs-15NiO/C NPs electrode at a scan rate of 10 mV s ⁻¹	50
4.17	GCD charge and discharge curves of (a) CNFs-Bare, (b) CNFs-5NiO/C NPs, (c) CNFs-10NiO/C NPs, and (d) CNFs-15NiO/C NPs electrode at various current densities of 0.5–5 A g ⁻¹	51
4.18	CV curves of CNFs-Bare, CNFs-5NiO/C NPs, CNFs-10NiO/C NPs, and CNFs-15NiO/C NPs electrode at a current density of 0.5 A g ⁻¹	52
4.19	Specific capacitance of CNFs-Bare, CNFs-5NiO/C NPs, CNFs-10NiO/C NPs, and CNFs-15NiO/C NPs electrode at various current densities of 0.5–5 A g ⁻¹	53
4.20	Nyquit plot of (a) CNFs-Bare, CNFs-5NiO/C NPs, CNFs-10NiO/C NPs, and CNFs-15NiO/C NPs electrode with (b) their high to low frequency region, where the solid lines represent the fitted data and the dashed lines correspond to the raw experimental data.	55
4.21	Cyclic stability for 1000 cycles of all electrodes at a current density of 3 A g ⁻¹	56

CHAPTER I

INTRODUCTION

The growing global demand for clean and sustainable energy has significantly increased interest in advanced energy storage devices. Among the various energy storage technologies, supercapacitors (SCs) stand out as an attractive choice due to their superior energy and power density, lightweight, prolonged cyclic lifespan, and rapid charge and discharge rates (Candelaria et al., 2012; Seo et al., 2012). Supercapacitors can be primarily categorized into two distinct types on the basis of their energy storage mechanisms. The first category is electric double-layer capacitors (EDLCs), which accumulate energy through the creation of electrical double layers at the electrode-electrolyte interface, thereby enabling rapid charging and discharging processes. The second category is pseudocapacitors (PCs), which employ the Faradaic mechanism to achieve higher specific capacitance and energy density. Consequently, PCs demonstrate superior capacitance and energy density when compared to EDLCs. While, EDLCs provide highly porous electrode structures, which result in elevated power density and extended operational cycling capability, although they possess comparatively lower specific capacitance values (Simon and Gogotsi, 2008; Stoller and Ruoff, 2010).

To address the substantial challenges that continue to impede the practical applications of supercapacitors, which are primarily attributed to the absence of high-performance electrode materials, current research is dedicated to developing high-performance electrodes that can deliver elevated energy density while simultaneously preserving high power density and exceptional cyclic stability. Various active materials are employed to create electrodes for SCs, including carbon-based materials, polymers, and transition metal oxides. Conventionally, materials that exhibit double-layer capacitance, including activated carbon (AC), carbon nanotubes (CNT), graphene, and carbon nanofibers (CNFs), are preferred due to their superior electrical conductivity properties, robust chemical and electrochemical stability characteristics, and extensive surface area attributed to their inherently porous structure (Saswata et al., 2012). These properties make them ideal for EDLCs. Conversely, materials such as metal hydroxides, transition metal oxides, and conducting polymers are utilized in pseudocapacitor (PCs) for their environmental friendliness, low cost, high voltage window, and substantial energy den-

sity (Fan and Maier, 2006; M. Liu et al., 2019; Prasad et al., 2004). To capitalize on the strengths of both material types, hybrid electrodes that combine carbon-based materials with transition metal oxides have been developed. These hybrid structures are designed to combine the high pseudocapacitance offered by transition metal oxides with the double-layer capacitance provided by carbon-based materials.

Recent advances in nanotechnology have further enhanced the potential of carbon nanostructures such as CNTs, CNFs, and graphene as active materials for supercapacitors electrode due to their potential to achieve high specific capacitance (Zhou and Wu, 2013). Among these carbon-based materials, CNFs have attracted significant attention due to their large specific surface area, intricate porous structure, robust electrical conductivity, strong mechanical stability, low density, and environmental benignity (Endo et al., 2001; P. Jiang et al., 2017; S.-J. Zhang et al., 2006). However, despite their advantage, CNFs alone exhibit lower energy density compared to pseudocapacitive materials. Thus, integrating CNFs with pseudocapacitive materials presents a viable strategy for enhancing the capacitive performance and energy density of CNF-based electrodes.

Among various transition metal oxides (MnO_2 , NiO , MoO_3 , Co_3O_4) (Abouali et al., 2015), NiO stands out for its high theoretical capacitance (3750 F g^{-1}) (G. Wang et al., 2012), cost effectiveness, thermal and chemical stability, and environmentally friendly (J. Li et al., 2011). However, its restricted electrical conductivity results in reduced electron transport kinetics, which subsequently affects the electrochemical performance of the electrode. Consequently, the formation of composites between carbon materials and transition metal oxides frequently leads to a reduction in the conductivity of the carbon materials (M. Liu et al., 2013). To address this limitation, recent research endeavors have primarily focused on enhancing electrical conductivity. One approach involves the fabrication of hybrid nanostructures comprising pseudocapacitive materials integrated within conductive matrix frameworks (Z. Lu et al., 2011). Therefore, the NiO/Ni composite is particularly notable. In this composite, NiO functions as the active material and has demonstrated superior electrochemical performance. This enhanced performance is attributed to effective charge storage capabilities. While, the conductive metallic Ni facilitates electron transport, thereby accelerating Faradaic reactions and improving the accessibility of the NiO (M. Liu et al., 2013).

The primary objective of this research is to develop and optimize carbon nanofibers (CNFs) decorated with NiO/Ni -carbon composites as high-performance elec-

trode materials for supercapacitors. This study aims to enhance the electrochemical performance, porosity, and specific surface area of supercapacitor electrodes through the innovative use of electrospinning and heat treatment techniques. Nevertheless, the fabrication of CNFs-NiO/Ni-Carbon composite nanostructures often involves complex, environmentally unfriendly and high-cost processes. The electrospinning method offers a simpler, cost-effective, and environmentally benign alternative for producing CNFs-NiO/Ni-Carbon nanocomposites for supercapacitor electrodes.

In this study, a simple and controlled approach was developed to prepare porous carbon nanofibers (CNFs) embedded with NiO/Ni-carbon composite nanoparticles (NiO/C NPs) for use as supercapacitor electrodes through electrospinning followed by heat treatment. This method is intended to increase the porosity and surface area of CNFs through the incorporation of NiO/C NPs, thereby enhancing the specific capacitance of the electrodes (Sajjad et al., 2021; M. Wang et al., 2019). By utilizing both charge storage mechanisms of PCs and EDLCs, this process enables the development of high-performance electrodes characterized by improved electrical conductivity, higher power and energy densities, and extended operational cycling life. The fundamental and electrochemical properties of the electrodes were investigated. Transmission electron microscopy (TEM), field emission scanning electron microscopy (FESEM), and Brunauer-Emmett-Teller (BET) analysis were employed to examine the microstructure, morphology, pore diameter, surface area, and pore volume properties of the samples. Additionally, X-ray diffraction (XRD), Fourier-transform Infrared spectroscopy (FTIR), Raman spectroscopy (Raman), X-ray Photoelectron spectroscopy (XPS), and X-ray Absorption spectroscopy (XAS) were used to determine the lattice structures, functional groups, elemental composition and oxidation state of the samples. The electrochemical properties were evaluated using cyclic voltammetry (CV), galvanostatic charge-discharge (GCD) testing, and electrochemical impedance spectroscopy (EIS) to study the redox behavior, specific capacitance values, and impedance characteristics of the electrodes, respectively. Electrochemical analysis revealed that the specific capacitance of CNFs-NiO/C NPs electrodes was significantly improved compared to CNFs without NiO/C NPs. Specifically, the CNFs-NiO/C NPs electrode containing 15 wt% of NiO/C NPs shows the highest specific capacitance of 474 F g^{-1} at a current density of 0.5 A g^{-1} in 1 M KOH electrolyte, while the CNFs without NiO/C NPs shows a specific capacitance of 266 F g^{-1} under the same conditions. These results demonstrate that the incorporation of NiO/C NPs effectively improves the performance of supercapac-

itor electrode systems, indicating their viability for application in the preparation of high-performance flexible supercapacitor devices.



CHAPTER II

LITERATURE REVIEW

This section covers topics that readers should know about this work. The first topic is a brief explanation of the meaning, components, types, and energy storage mechanism of supercapacitors. The second topic describes the types of active materials that affect the energy storage mechanisms of supercapacitors. The third and fourth topics discuss the active materials that we use in this work, which are NiO and carbon nanofibers, respectively. In addition, these topics will explain the properties, advantages, and reasons for choosing these two materials. The fifth topic describes the method used to fabricate our active material, namely the electrospinning method, and explains the advantages and working principle of this method. Finally, the sixth topic addresses the electrolyte selection process, emphasizing its critical role in determining supercapacitor performance and the criteria used to select an appropriate electrolyte for this study.

2.1 Supercapacitors

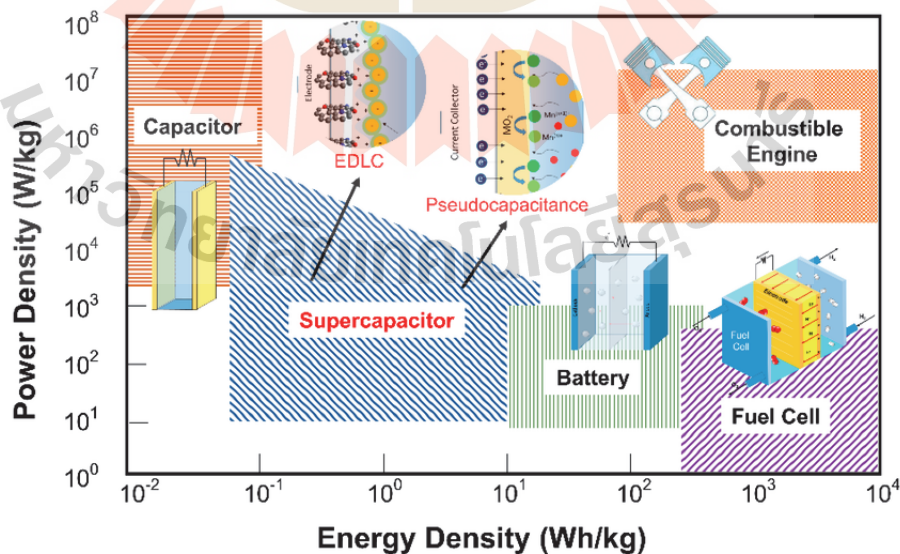


Figure 2.1 The Ragone energy storage device plot (Permatasari et al., 2021)

Energy remains a critical global concern, as energy resources are essential for both industrial and residential use. However, conventional fossil fuel-based energy production significantly contributes to environmental degradation and economic instability. These challenges have accelerated the aim of high-performance, cost-effective, and environmentally friendly. Among various energy storage devices, supercapacitors (SCs) have received significant attention as promising clean energy storage technologies.

A supercapacitor (or ultracapacitor), functions as an bridge between batteries and conventional capacitors. It provides greater power density relative to batteries and greater energy density compared to conventional capacitors, as shown in Figure 2.1. While supercapacitors store electrical energy through electrostatic charge accumulation, similar to conventional capacitors, they differ significantly in performance characteristics. Notably, they exhibit extended cycle life, rapid charge and discharge capabilities, and enhanced power and energy densities. A typical supercapacitor consists of four primary components: current collectors, electrodes, an electrolyte, and a separator, as illustrated in Figure 2.2.

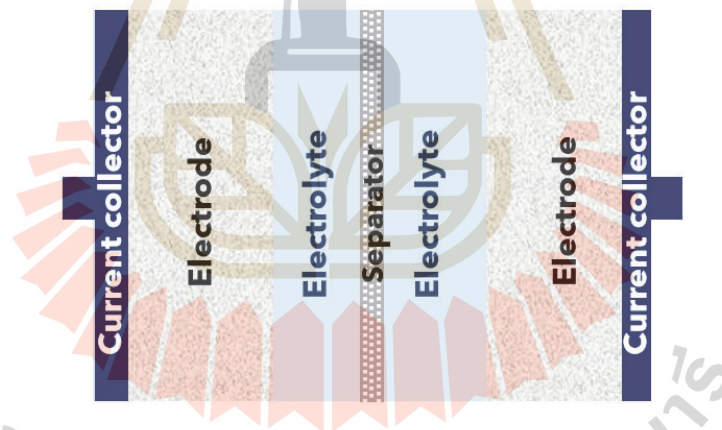


Figure 2.2 Diagram of supercapacitor components (Smith et al., 2020).

The electrode stores charges through capacitive or faradaic mechanisms involving interactions between the electrolyte ions and the electrode material. The electrolyte supplies the ions necessary for the charging and discharging operations. The separator acts as an insulating barrier, preventing short circuits within the device. The current collector provides a conductive pathway that facilitates the flow of electrons into the external circuit (Kar, 2020b).

A supercapacitor is generally categorized into three types based on their mechanisms of charge storage, which consist of electric double-layer capacitors (EDLCs),

pseudocapacitors (PCs), and hybrid capacitors (Tahir et al., 2020). Each type is discussed briefly as follows.

2.1.1 Electric Double Layer Capacitors (EDLCs)

An electrical double-layer capacitor (EDLC) is an energy storage system that stores energy by depositing ions in the electrolyte in the form of an extremely thin layer to balance the charge of the oppositely charged electrode layers. Therefore, it creates a double layer at the electrode–electrolyte interface (Fic et al., 2018), as shown in the Figure 2.3. Additionally, the energy storage mechanism of EDLCs enables high power output, and rapid energy uptake. Due to their non-Faradaic process, EDLCs exhibit excellent power density and extended operational lifespans. Unlike batteries, which typically endure only a few thousand charge-discharge cycles, EDLCs can withstand millions of cycles, making them particularly suitable for long-term energy storage applications (Kötz and Carlen, 2000; Shiraishi and Tanaike, 2015).

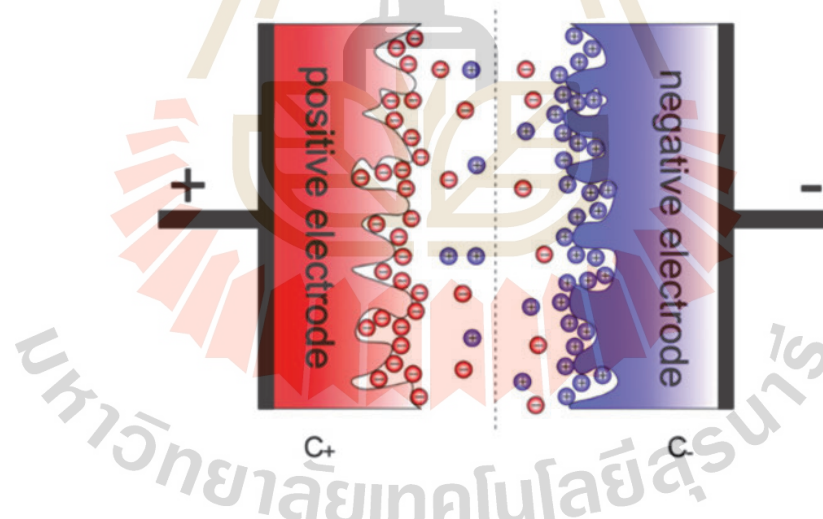


Figure 2.3 Diagram of electric double layer formation on the interfaces of both electrodes (Beguin et al., 2014).

2.1.2 Pseudocapacitors (PCs)

A pseudocapacitor (PC) is a category of supercapacitors that stores electrical energy through a mechanism distinct from those of electrical double-layer capacitors

(EDLCs), as shown in the Figure 2.4. It stores energy through highly reversible redox reactions rather than charge electrostatic attraction (Goswami et al., 2023), which involve the electron transfer between electrode and electrolyte (Shao et al., 2018). Moreover, pseudocapacitors outperform EDLCs in terms of energy density due to the reversible redox reaction at the electrode–electrolyte interface (Miao and Liu, 2019).

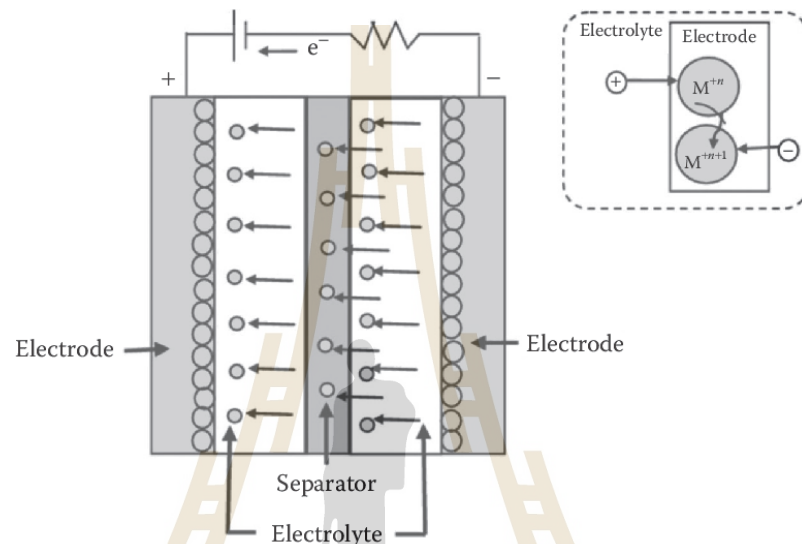


Figure 2.4 Diagram of charge storage mechanism of pseudocapacitors (Tyagi and Gupta, 2015).

2.1.3 Hybrid Capacitors

A hybrid capacitor is a form of supercapacitor that integrates the charge storage mechanisms of both EDLCs and PCs. This design was developed to achieve significantly higher energy density compared to conventional EDLCs, while maintaining high power performance and extended cycle life. Early configurations of hybrid capacitors combined a Faradaic oxide electrode with an activated carbon electrode, resulting in the development of a high-performance energy storage device (Muzaffar et al., 2019).

One important component of a supercapacitor is the electrode, which participates in electrochemical processes to generate energy and power. Moreover, the type of active material utilized in the electrode significantly influences charge storage within the supercapacitor. To attain a high-performance supercapacitor, the electrodes should exhibit high surface area, well-developed porosity, excellent chemical and thermal stability, electrical conductivity, effective adsorption-desorption properties, and ro-

rust redox activity (Kar, 2020b). The active materials within the electrode impact the occurrence of capacitive and Faradaic charge storage mechanisms. Carbon-based materials provide high surface area, excellent conductivity, and material stability, whereas redox-active materials such as metal oxides and conducting polymers offer numerous electrons, thereby enhancing capacitance (Kar, 2020a). Composite electrodes, which incorporate both EDLC and PC charge storage mechanisms, can potentially reduce electrode costs while enhancing specific capacitance and electrical properties.

2.2 Active Material

In section 2.2, we explored the importance of active materials in determining electrode performance. This section shifts focus to the diversity of active materials employed across different supercapacitor electrodes. These materials are categorized into two primary types based on their charge storage mechanisms: (I) materials exhibiting double-layer capacitance and (II) materials demonstrating pseudocapacitance (Kar et al., 2015). Figure 2.5 provides an overview of active materials in supercapacitor electrodes.

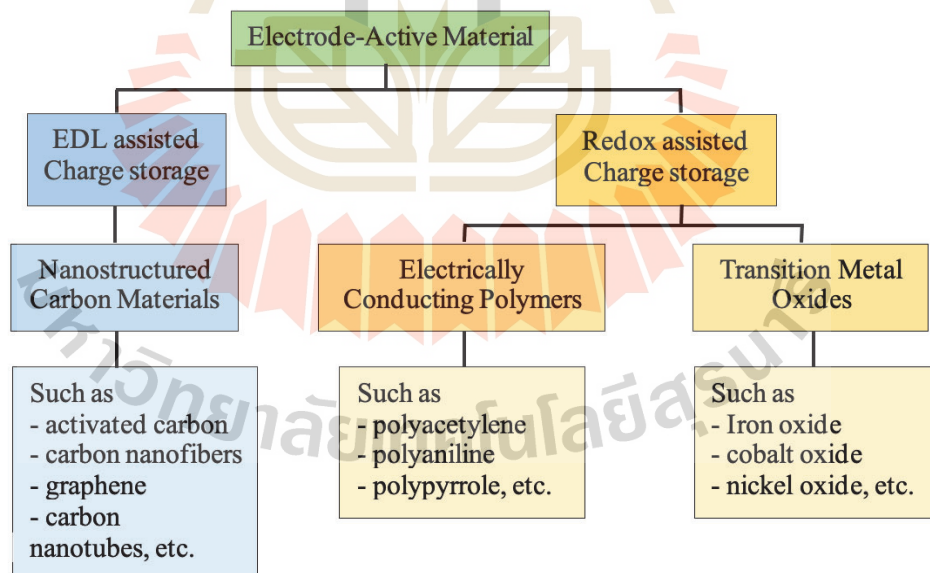


Figure 2.5 Diagram of different active materials used as electrode for supercapacitors (C. Lee et al., 2019).

2.2.1 Materials with Double-Layer Capacitance

The active materials with electric double-layer capacitance are generally carbon-based materials, such as activated carbon (AC), carbon nanotubes (CNTs), graphene, and carbon nanofibers. The characteristic properties of this type of supercapacitor electrode include superior electrical conductivity, remarkable chemical and electrochemical stability, and a high specific surface area resulting from their highly porous structure (Ahankari and Kar, 2017; Zan et al., 2017). In addition, the presence of a porous structure can enhance ion absorption in the electrolyte, thereby improving the properties of the electrode for supercapacitors (Tran and Kalra, 2013).

2.2.2 Materials with Pseudocapacitance

Metal hydroxides, transition metal oxides, metal oxides, and conducting polymers are prime materials used as active materials for pseudocapacitors. The high-efficiency characteristics of pseudocapacitive materials are utilized in the charge storage mechanism, as indicated by devices with high energy density (Kar, 2020b). However, these materials have some disadvantages, such as limited conductivity and a low electrolyte-accessible surface area. These disadvantages hinder efficient ion transfer, thus reducing their ability to store ions. However, when compared to double-layer capacitive materials, they have higher energy density and specific capacitance values. In summary, PCs have higher energy density, while EDLCs have higher power density. Notably, both mechanisms can operate concurrently within a hybrid electrode design, effectively integrating the high energy characteristics of PCs with the high power characteristics of EDLCs. Therefore, the development of nanocomposite materials based on double-layer capacitive materials and pseudocapacitive materials for supercapacitors electrode is a good choice to improve storage efficiency (Tai et al., 2012).

In this study, we aim to develop an electrode that incorporates both pseudocapacitance and electric double-layer capacitance by using a nanocomposite of carbon nanofibers (CNFs) decorated with NiO/C to enhance electrode performance. In the next section, we provide an in-depth analysis of CNFs and NiO/C, emphasizing, why these materials were chosen as active materials for high-performance supercapacitor electrodes.

2.3 Carbon Nanofibers (CNFs)

Among various carbon-based materials, carbon nanofibers (CNFs) have attracted considerable attention over the past decade. CNFs are one-dimensional (1D) nanostructures characterized by their nanoscale diameters, tunable architectures, high length-to-diameter ratio (LDR), and efficient charge transport along their longitudinal axis. They also exhibit excellent mechanical flexibility and are readily adaptable for integration into wearable electronic devices (Han et al., 2014; X. Lu et al., 2017). Owing to these advantageous properties, CNFs are regarded as promising candidates for a wide range of applications, including catalyst supports, supercapacitors, and hydrogen storage systems (Karuppanan et al., 2018). Additionally, CNFs possess favorable thermal and electrical conductivities, electromagnetic shielding capabilities, and mechanical resilience (Tibbetts et al., 2007). Their widespread use in composite materials is further supported by the abundance and cost-effectiveness of carbon resources (Hammel et al., 2004). As a result, CNFs serve a critical role in the development of advanced supercapacitor electrodes systems, offering large surface area, tunable conductivity, and ease of fabrication (Tai et al., 2012).

Currently, several techniques are available for the synthesis of carbon nanofibers (CNFs), including electrospinning followed by calcination, self-assembly, template-assisted synthesis, hydrothermal conversion, and catalytic thermal chemical vapor deposition (CVD) (Kang et al., 2013; Liang et al., 2012; X. Lu et al., 2017; K. Wang et al., 2007). Among these, electrospinning has emerged as one of the most widely employed and effective methods for producing CNFs. Notably, electrospinning is regarded as a simple and highly controllable technique capable of yielding CNFs with tailored morphologies and freestanding architectures (X. Lu et al., 2019; Z. Zhu, Ji, et al., 2017; Z. Zhu, Xu, et al., 2017). Therefore, this study focuses exclusively on the fabrication of CNFs using the electrospinning process followed by calcination. To fabricate CNFs via the electrospinning process, polymeric nanofibers are first fabricated as precursors for CNFs. The properties of CNFs depend on the type of polymer precursor solution used and the operational parameters of the electrospinning process (Lichao et al., 2014). Therefore, selecting the appropriate precursor materials for CNFs is crucial to achieving the desired properties. There is an extensive variety of carbon-based molecules are utilized as precursors of CNFs, as shown in Figure 2.6, due to their ability to form graphite or turbostructured microstructures (B.-S. Lee and Yu, 2020). Examples of precursors containing carbon-based molecules include poly (acrylonitrile) (PAN) (Padmavathi and

Sangeetha, 2013), poly (vinyl alcohol) (PVA) (Barakat et al., 2012; Ghouri et al., 2015; Motlak et al., 2015) polyamide 6 (PA6) (Karacan and Meşeli, 2016), and silk (Q. Wang et al., 2017). After low-temperature heat treatment, aromatic rings are formed in a linear polymer structure. In contrast, materials such as pitch (Cervo and Thies, 2007), coal (Guo et al., 2015), tar (K. Song et al., 2015), polyimide (PI) (K. Yang et al., 2003), propylene glycol monomethyl ether acetate (PGMEA; SU-8) (Steach et al., 2010), and phenolic resin (Huang et al., 2009; Tian et al., 2015) require higher temperatures, where intermolecular crosslinking converts aromatic rings into graphitic or turbostratic structures (B.-S. Lee and Yu, 2020).

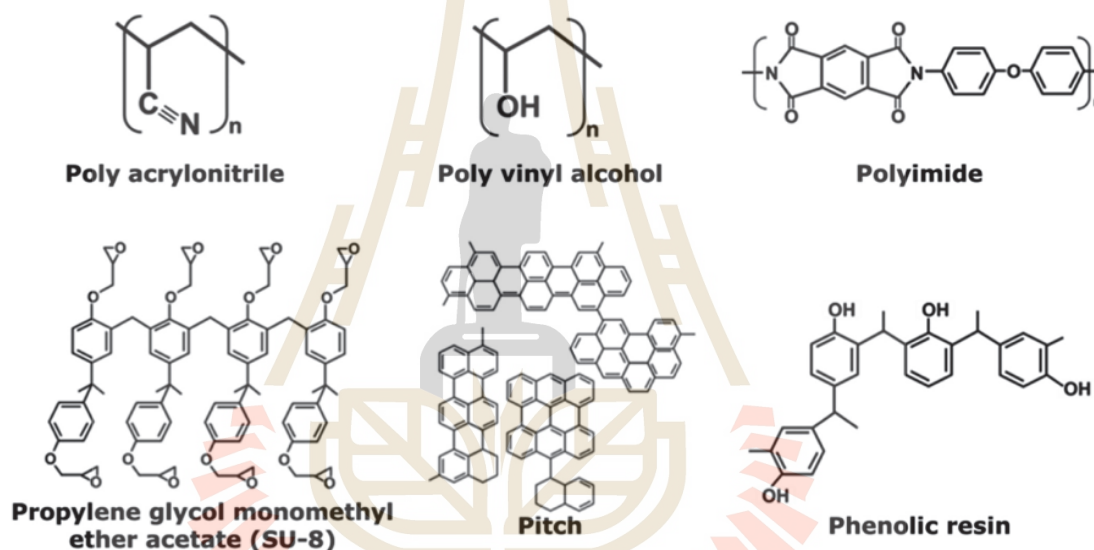


Figure 2.6 Frequently used polymer as precursors for carbon nanofibers (B.-S. Lee and Yu, 2020).

Some of the precursors mentioned above are unique characteristics. For instance, polyvinyl pyrrolidone (PVP) is water-soluble, and PVA can enhance the environmental friendliness of the electrospinning process. The heteroatoms in poly (norbornyldecaborane), and melamine resin can be adjust the microstructure, and properties of the material. PGMEA has the photoresist characteristics, resulting in the generation of patterned CNFs (B.-S. Lee and Yu, 2020). Additionally, PAN is one of the most extensively studied and commonly used precursors for CNFs due to its high carbon yield, ease of fiber formation, and excellent thermal stability (Inagaki et al., 2012; Padmavathi and Sangeetha, 2013).

When the nanofibers are successfully prepared through electrospinning process (The electrospinning process is discussed in section at 2.5), the thermal treatment involves heating the as-spun nanofibers to form CNFs, as shown in Figure 2.7. The transformation of PAN nanofibers into CNFs involves two sequential thermal treatment steps: stabilization and carbonization, both of which play a critical role in determining the structural and functional characteristics of the resulting CNFs. During the stabilization process, temperatures between 200 to 300°C in air induce a series of chemical transformations, including oxidation, aromatization, cyclization, dehydrogenation, and crosslinking (Bashir, 1991; J. Chen and Harrison, 2002; Flöck et al., 1999). This step serves as a crucial precondition for the carbonization process and has a significant impact on the structural and properties of the resulting CNFs. In the carbonization step, the stabilized PAN fibers are subjected to thermal treatment in an inert gas atmosphere at temperatures typically ranging from 800 - 1200°C. Although various temperatures can be applied, 800°C is most commonly used to effectively eliminate non-carbon elements from the fiber structure (Rahaman et al., 2007; Storck et al., 2021). Graphitization of the fibers occurs under an inert atmosphere at temperatures reaching up to 3000°C, producing CNFs with a carbon content exceeding 99% and well-developed graphitic layers, which contribute to enhanced electrical conductivity (D. Zhu et al., 2002). Therefore, the parameters of the heat treatment process, including gas atmosphere, stabilization, and carbonization temperatures, significantly impact the porosity, morphology, crystallinity, purity, and diameter of the resulting CNFs. Generally, the volume and weight of nanofibers change during carbonization, leading to a reduction in CNF diameter. In most cases, CNFs produced via the electrospinning process tend to form a web-like structure, which is highly suitable for application as an active material in supercapacitor electrodes.

The overall efficiency of a supercapacitor largely depends on the effectiveness of ion transport processes between the electrolyte and electrode. Therefore, the presence of a porous structure is critical for optimizing supercapacitor performance by facilitating ion movement within the electrolyte (Lichao et al., 2014). Although CNFs electrode materials provide high surface area, pore volume, power density, and a long cycle lifetime, they exhibit lower energy density compared to materials with pseudocapacitance (Hu et al., 2012). Consequently, nanocomposites of CNFs and transition metal oxides are a promising choice for improving the charge storage efficiency of supercapacitor electrodes, as shown in Table 2.1. Transition metal oxides are frequently

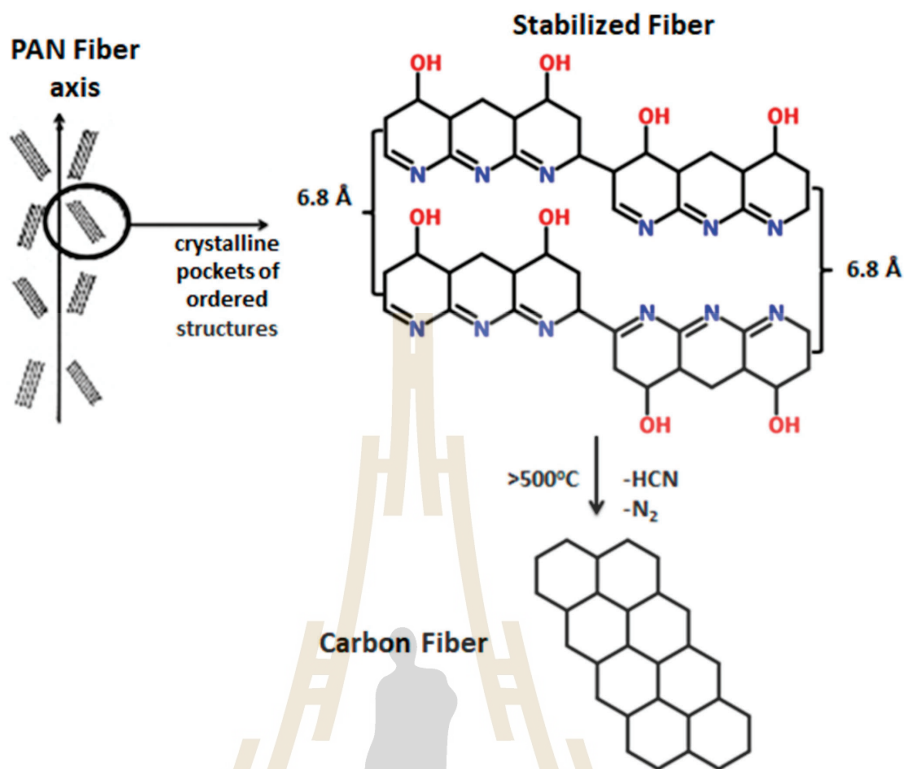


Figure 2.7 Stabilization and carbonization mechanism of PAN nanofibers (Konstantopoulos et al., 2020).

utilized as electrode materials in pseudocapacitors because of their higher energy density, and specific capacity compared to EDLCs (C. H. Kim and Kim, 2015). In the next section, we discuss the oxides of transition metals used as nanocomposites with CNFs in this study.

2.4 Transition Metal Oxide-Based Electrode Material

Transition metal oxides (TMOs), used as electrode materials are divided into two types. One is noble transition metal oxides such as RuO_2 , and IrO_2 . The other is base transition metal oxides such as MnO_2 , Co_3O_4 , and NiO (Kar, 2020a; Z. Wu et al., 2016). Noble transition metal oxides are relatively costly. In contrast, base transition metal oxides are inexpensive and environmentally friendly, making them suitable for supercapacitor applications. Due to their excellent electrical, mechanical, and redox properties, TMOs are widely used in various energy storage applications (Kar, 2020a).

Table 2.1 Recent CNFs and CNFs/TMO composite Electrode materials for EDLC supercapacitors.

Material	Specific Capacitance (SC)	Electrolyte	Reference
Pure electrospun CNF (baseline)	130 F g ⁻¹ at 0.5 A g ⁻¹	1 M Na ₂ SO ₄	(S. K. Kim et al., 2024)
CNF + Ti ₃ C ₂ MXene (M-CNF)	514 F g ⁻¹ at 0.5 A g ⁻¹	1 M Na ₂ SO ₄	(S. K. Kim et al., 2024)
f-CNFs/PEDOT/MnO ₂	537 F g ⁻¹ at 5 mV s ⁻¹	1 M KCl	(Mohd Abdah et al., 2019)
PANI/Fe ₂ O ₃ /CNFs	603 F g ⁻¹ at 1 A g ⁻¹	1 M Na ₂ SO ₄	(Gu et al., 2024)
core-shell CNFs@Ni(OH) ₂ /NiO	695 F g ⁻¹ at 1 A g ⁻¹	6 M KOH	(Fan and Maier, 2006)
NiO-coated activated CNFs	870 F g ⁻¹ at 1 A g ⁻¹	6 M KOH	(X. Yang et al., 2023)

The development of suitable electrode materials is crucial for enhancing the electrochemical performance of supercapacitors. Commonly utilized electrode materials include RuO₂, MnO₂, NiO, MoOx, and Ni(OH)₂ (Abouali et al., 2015). Among various pseudocapacitive materials, RuO₂ has garnered significant research attention due to its facile synthesis, high theoretical specific capacitance, excellent electrical conductivity, and exceptional redox activity (Kar, 2020a; Venkatachalam et al., 2004; W. Wang et al., 2014; C. (Zhang et al., 2014). However, the disadvantages of RuO₂ are its toxicity and high cost (Abouali et al., 2015). Therefore, there is a need to identify materials that are both cost-effective and high-performing. Nickel oxide (NiO) nanostructures have emerged as promising electrode materials for electrochemical energy storage devices, attributed to their high theoretical capacitance (2584 F g⁻¹)(Prabhu et al., 2024), affordability, excellent chemical and thermal stability, non-toxicity, and environmental

friendliness (J. Li et al., 2011). Consequently, NiO is an attractive option for supercapacitor electrodes. Nonetheless, original oxide materials typically suffer from poor specific surfaces, rapid charge generation, and limited reactive sites, which can lead to suboptimal electrochemical properties. When oxide materials are used alone to synthesize an electrode, the resulting electrode exhibits poor storage capacity (Reddy et al., 2021).

The specific capacitance of electrodes is primarily influenced by the porosity and conductivity of the active materials, crucial for ion adsorption, penetration, and rapid transport (Daubert et al., 2015). To enhance the performance of supercapacitors, it is essential to incorporate materials with excellent conductivity and large surface areas into the electroactive material. Creating a nanocomposite of NiO with other materials that possess large surface areas and good conductivity can address the active site limitations of the NiO structure. Therefore, the synthesis of NiO-carbon nanocomposites can serve as an effective strategy to overcome the active site limitations inherent in NiO structures for use in supercapacitor electrodes.

In recent years, various research efforts have focused on synthesizing different forms of NiO-carbon nanocomposites, as shown in Table 2.2. For instance, Liu et al. synthesized NiO/C nanofibers by an electrospinning method for supercapacitors with a specific capacitance value of 461 F g^{-1} at current density of 1 A g^{-1} (X. Liu et al., 2022). Similarly, Fayed et al. synthesized NiO/AC nanocomposite structures for supercapacitor electrode with a specific capacitance value of 325 F g^{-1} at current density of 1 A g^{-1} (Fayed et al., 2025). Meanwhile, Zhang et al. prepared reduced graphene oxide@NiO composites for supercapacitor applications with a specific capacitance value of 1093 F g^{-1} at current density of 1 A g^{-1} (Y. Zhang et al., 2020). Moreover, Jiang et al. achieved NiO/Ni@C calcination temperature at 500°C as electrode materials for supercapacitor application with a specific capacitance value of 805.3 F g^{-1} at current density of 0.5 A g^{-1} (X. Jiang et al., 2021), while Muduli et al. synthesized carbon framework decorated NiO nanorods (NiO@C) via one-pot hydrothermal synthesis method for supercapacitor electrode with a specific capacitance value of 1360 F g^{-1} at current density of 1 A g^{-1} (Muduli et al., 2023). Furthermore, Jiang et al. fabricated NiO@-Co₃O₄ core/shell nanofibers for high-performance supercapacitors with a specific capacitance value of 437 F g^{-1} at current density of 1 A g^{-1} (P. Jiang et al., 2017). In addition, Yang et al. prepared Self-supporting NiO-coated activated carbon nanofibers (NiO-coated activated CNFs) via atomic layer deposition for supercapacitor applications with a specific capacitance value of 870 F g^{-1} at current density of 1 A g^{-1} (X. Yang et al., 2023). These studies not only

demonstrate the versatility of NiO/carbon hybrids in tailoring electrochemical behavior but also highlight the critical role of synthesis technique, composite architecture, and nanostructuring in unlocking superior energy storage performance.

Table 2.2 Recent NiO-carbon composite for supercapacitor electrode materials.

Material	Specific Capacitance (SC)	Electrolyte	Reference
NiO/C nanofibers	461 F g ⁻¹ at 1 A g ⁻¹	2 M KOH	(X. Liu et al., 2022)
NiO/AC nanocomposite	325 F g ⁻¹ at 1 A g ⁻¹	6 M KOH	(Fayed et al., 2025)
Reduced graphene oxide @NiO composites	1093 F g ⁻¹ at 1 A g ⁻¹	6 M KOH	(Y. Zhang et al., 2020)
NiO/Ni@C composites	805.3 F g ⁻¹ at 0.5 A g ⁻¹	6 M KOH	(X. Jiang et al., 2021)
Carbon framework decorated NiO nanorods	1360 F g ⁻¹ at 1 A g ⁻¹	1 M KOH	(Muduli et al., 2023)
NiO-coated activated CNFs	870 F g ⁻¹ at 1 A g ⁻¹	6 M KOH	(X. Yang et al., 2023)

In this work, we synthesized carbon nanofibers decorated with a nickel oxide composite with carbon nanoparticles using the electrospinning method, followed by heat treatment. NiO/C was chosen as the nanocomposite material due to its ability to significantly enhance the specific surface area and increase pore density, thereby facilitating efficient diffusion of electrolyte ions throughout the porous network. Furthermore, this structural design promotes enhanced permeability of electrolyte ions into the electrode matrix, thereby increasing the number of ions participating in redox reactions. As a result, the overall charge storage capacity of the supercapacitor is improved.

2.5 Electrospinning method

There are many processes to create nanofibers such as phase separation , drawing, and electrospinning (Pham, 2022). Among these, the electrospinning method stands out as one of the simplest, straightforward, and cost-effective techniques for rapidly producing nano- and micro-sized fibers. Consequently, it is one of the most widely utilized methods for nanofiber production. Nanofibers created by the electrospinning method exhibit superior physical properties compared to larger-sized fibers. In the electrospinning method, electrostatic forces alone are used to create the nanofibers, with shearing forces arising from the interaction of an electrostatic field applied to an electric charge carried by the polymer jet (Asmatulu and Khan, 2019).

Figure 2.8 illustrates a schematic diagram of the electrospinning process. In the electrospinning process, an electric field is applied to stretch the polymeric jet. This stretching is a result of the repulsive forces acting on the surface of the jet. The electrostatic repulsion between the charges on the surface of the polymeric solution droplet at the tip of the needle increases until it overcomes the tension force on the surface of the polymeric solution. This action causes a solution jet to shoot out from the tip towards the collector in a constant flow. When the jet reaches the point of bending, it starts whipping towards the collector. Subsequently, the solvent contained in the polymer solution completely evaporates, causing the jet to harden and form fibers on the collector. These fibers, synthesized by electrospinning, typically have diameters in the nanometer range, and thus commonly referred to as nanofibers (Inagaki et al., 2012).

Factors that affect the morphology and spinnability of a polymeric solution include the properties of the polymeric solution, processing settings, and surrounding conditions. First, polymeric solution properties include surface tension, electrical conductivity, and viscosity of the polymeric solution. These properties depend on several factors: (i) the precursor of polymeric solution, including its concentration, molecular weight, and structure; (ii) the solvents, considering aspects such as vapor pressure and air diffusion; and (iii) additives, such as surfactants and salts. Secondly, processing conditions are influenced by factors such as the flow rate of the polymer solution controlled by the syringe pump, the strength of the electric field applied via the power supply, and the distance between the needle tip and the collector. These factors are influenced by the properties of the polymer solution. Finally, atmospheric conditions include the type of gases used during electrospinning, the flow rate of gas, and the

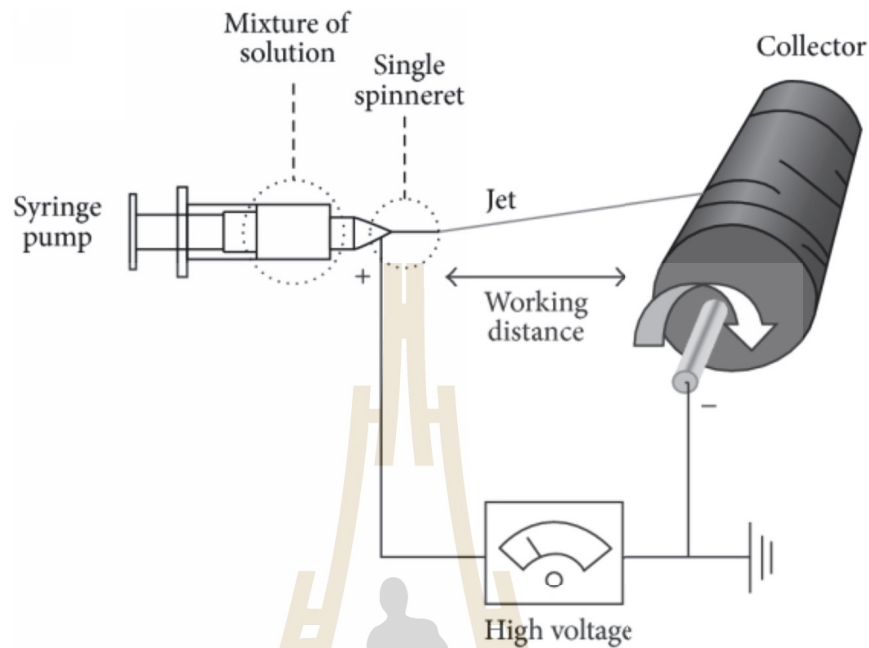


Figure 2.8 Electrospinning diagram (Mori et al., 2015).

humidity in the electrospinning hood. However, most research on electrospinning of nanofibers focuses on regulating the properties of polymer solution and processing conditions while often neglecting atmospheric factors, which are rarely mentioned. In this work, we controlled first two factors, as discussed in the preparation section 3.2 for use as electrodes for supercapacitors (Inagaki et al., 2012).

2.6 Electrolyte

Electrolytes have a significant impact on the efficiency of supercapacitors. Supercapacitors rely on electrolytes for their charge and discharge processes, which can be categorized into three types: liquid, solid-state, or quasi-solid-state, and redox-active electrolytes (Figure 2.9). The characteristics of electrolytes are as follows: (i) ion type and size; (ii) ion and solvent concentration; (iii) ion-solvent interaction; (iv) interaction between electrode material and electrolyte; and (v) the potential window, all of which influence the electric double layer capacitance, pseudocapacitance, energy and power density, and supercapacitors' cyclic lifetime (Kar, 2020a).

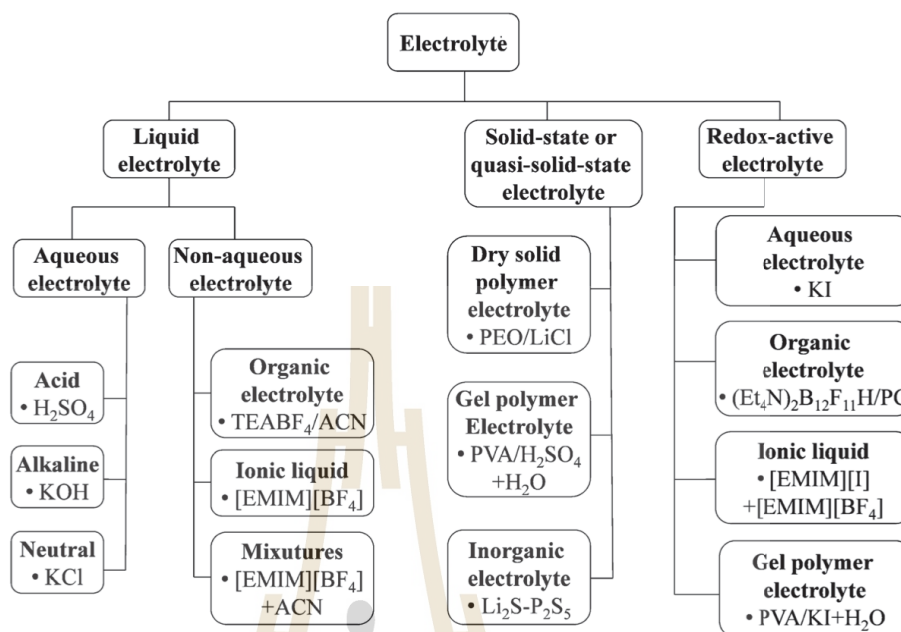


Figure 2.9 Type of electrolytes for supercapacitors (B.-S. Lee and Yu, 2020).

The choice of the appropriate electrolyte for a supercapacitor depends on the material used for the electrode. In this study, we employed two materials with distinct properties: a nanocomposite carbon nanofiber and a transition metal. Among the various aqueous electrolytes, KOH is a commonly used alkaline electrolyte because of its high ionic conductivity (with the highest value of 0.6 S/cm for a 6 M solution). This alkaline electrolyte can be used for EDLCs, PCs and hybrid supercapacitors (Zhong et al., 2015). Therefore, the specific capacitance of the electrode is influenced by both the type of electrolyte and the type of electrode material. For instance, Subbukalai et al. reported that porous NiO/C nanocomposites exhibited a specific capacitance of 644 F g⁻¹ when tested in 2 M KOH at a scan rate of 2 mV s⁻¹ (Vijayakumar et al., 2013). Similarly, Yang et al. fabricated NiO-coated activated carbon nanofibers, which achieved a specific capacitance of 870 F g⁻¹ in 6 M KOH at a current density of 1 A g⁻¹ (X. Yang et al., 2023). Additionally, Jiang et al. developed NiO/Co₃O₄ core/shell nanofibers that demonstrated a specific capacitance of 437 F g⁻¹ in 6 M KOH at the same current density (L. Jiang et al., 2018).

However, we use only 2 M KOH because using a more concentrated electrolyte can cause corrosion on the surface of the electrode, leading to the detachment of the electrode material from the surface (Patil et al., 2008). Therefore, it is neces-

sary to optimize the electrolyte concentration based on the electrode performance, as this plays a critical role in the development of supercapacitors with enhanced energy density, power output, and long-term cycling stability (J. Lu et al., 2024).



CHAPTER III

RESEARCH METHODOLOGY

This section provides a description of the procedures used to fabricate carbon nanofibers decorated with nickel oxide–carbon composites nanoparticles (CNFs–NiO/C NPs). The fabrication process is presented across section 3.1 to 3.3. Section 3.1 outlines the synthesis of the nickel oxide composites with carbon nanoparticles (NiO/C NPs), detailing the chemical preparation and thermal treatment steps required to obtain the composite material. Section 3.2 focuses on the integration of the NiO/C NPs composites with carbon nanofibers, describing the processing conditions and techniques employed to achieve mostly uniform decoration. Section 3.3 focuses on the fabrication and preparation of the working electrodes. Section 3.4 presents the characterization methods used to analyze the structural, morphological, and compositional properties of the synthesized materials. Finally, section 3.5 details the electrochemical measurements used to evaluate the electrochemical performance of the CNFs–NiO/C NPs electrodes.

3.1 Synthesis of Nickel Oxide Composite with Carbon Nanoparticles (NiO/C NPs)

NiO/C nanoparticles (NiO/C NPs) were prepared by collaborators in South Korea using a solvothermal technique followed by high-energy ball milling process, as shown in Figure 3.1 (Nguyen and Bark, 2020). Specifically, 1.3 g of $\text{Ni}(\text{NO}_3)_2 \cdot 6\text{H}_2\text{O}$ was dissolved in 20 mL of methanol and stirred thoroughly to achieve complete dissolution and obtain a uniform green solution. Subsequently, 0.5 g of H_3BTC was introduced into the solution and stirred at 25°C for 1 hour. The resulting mixture was then sealed in an autoclave and heated at 150°C for 24 hours. The obtained product was separated by centrifugation and repeatedly washed several times with ethanol and deionized water to produce Ni-BTC. This intermediate was dried in air at 60°C and subsequently sintered at 400°C for 4 hours to obtain NiO/C microparticles (NiO/C MPs). These microparticles were then subjected to size reduction through a high-energy ball milling process. The NiO/C MPs were dispersed in isopropyl alcohol (IPA) and placed in a vessel containing

zirconia grinding beads. Ball milling was conducted for 24 hours, after which the resulting powders were dried at 80°C for 24 hours to obtain NiO/C nanoparticles (NiO/C NPs).

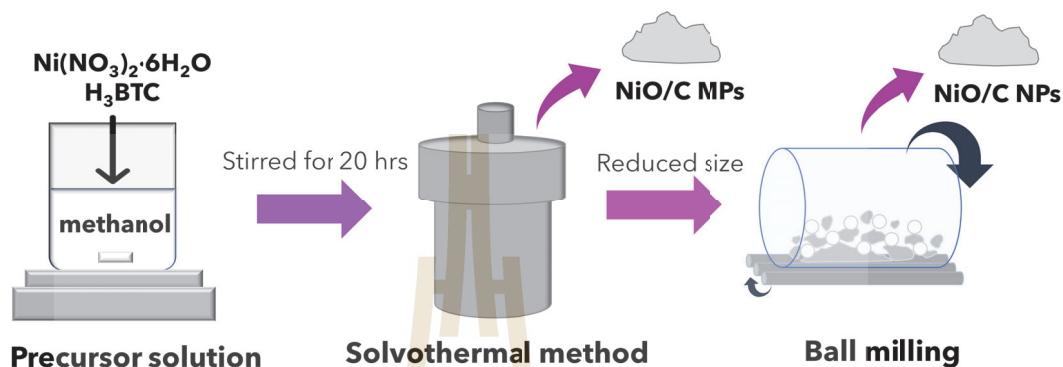


Figure 3.1 Schematic of NiO/C MPs and NPs preparation (Nguyen and Bark, 2020).

3.2 Preparation of Carbon Nanofibers Decorated with NiO/C (CNFs-NiO/C NPs)

Figure 3.2 presents the fabrication process of carbon nanofibers decorated with NiO/C. Initially, 0.5 g of polyacrylonitrile (PAN, molecular weight = $150,000 \text{ g mol}^{-1}$) was dissolved in 4.5 g of N,N-dimethylformamide (DMF) and stirred continuously for 20 hours to obtain a homogeneous polymer solution. Subsequently, NiO/C nanoparticles synthesized by our collaborators in South Korea, as described in section 3.1, were added to the solution and stirred for an additional 8 hours to ensure uniform dispersion. The resulting suspension was then loaded into a 10 mL syringe fitted with a blunt-ended needle having an inner diameter of 0.9 mm. Electrospinning was performed under controlled conditions with a flow rate of 2.6 mL h^{-1} , an applied voltage of 15 kV, and a needle-to-collector distance of 14 cm. The process yielded PAN nanofibers embedded with NiO/C NPs (PAN-NiO/C NPs), which were collected on the rotating drum collector. The collected nanofiber mats were first stabilized by heating at 60°C in air for 24 hours. This was followed by a thermal stabilization step in which the mats were heated to 240°C at a heating rate of 2°C min^{-1} and maintained at that temperature for 4 hours. Carbonization was then carried out at 800°C in an argon atmosphere, with a heating rate of 5°C min^{-1} and hold time of 1.5 hours. The final product was designated as CNFs-NiO/C NPs. To evaluate the optimal amount of NiO/C nanoparticles for the decoration of

carbon nanofibers (CNFs) intended for supercapacitor electrode applications, varying weight fractions of NiO/C nanoparticles were incorporated into a constant mass of the polymer precursor. Specifically, NiO/C nanoparticles were added into the precursor solution at concentrations of 0, 5, 10, and 15 wt%, relative to the weight of PAN. The resulting samples were labelled as CNFs-Bare, CNFs-5NiO/C NPs, CNFs-10NiO/C NPs, and CNFs-15NiO/C NPs, corresponding to 0, 5, 10, and 15 wt% NiO/C nanoparticle loading, respectively.

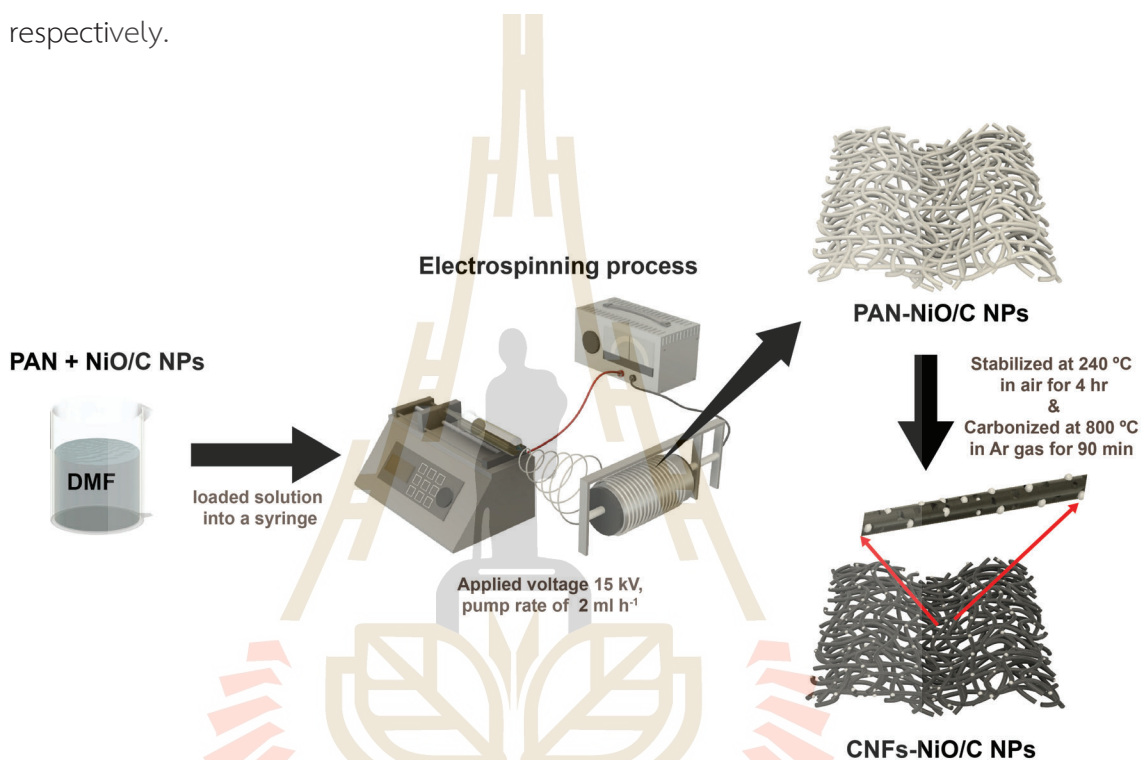


Figure 3.2 Schematic of carbon nanofibers decorated with NiO/C preparation.

3.3 Preparation of Working Electrode

The working electrode was fabricated by sandwiching CNFs-NiO/C NPs between Cu foams. CNFs-NiO/C NPs samples were cut into approximately $1 \times 1 \text{ cm}^2$ squares with an average mass of 2.50 mg. These mats were then sandwiched between pieces of Cu foam measuring $1.5 \times 2 \text{ cm}^2$, as shown in Figure 3.3. The assembled electrodes were compressed at a pressure of 5 MPa for 2 minutes to enhance mechanical contact. Subsequently, the electrodes were immersed in a 2 M KOH electrolyte solution and left to soak overnight to ensure thorough electrolyte absorption.

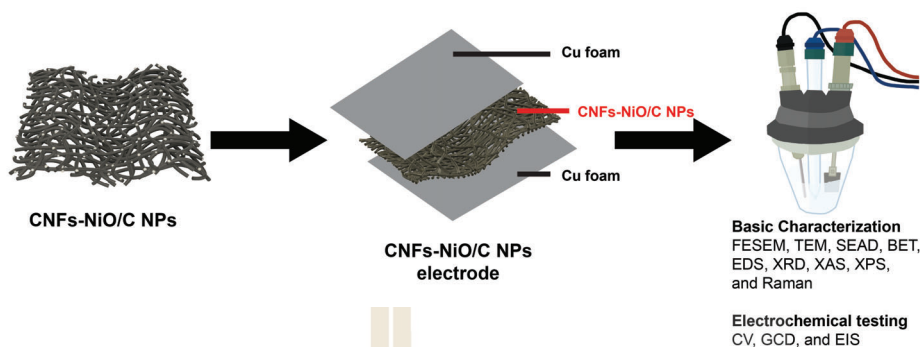


Figure 3.3 Schematic of CNFs-NiO/C NPs electrode preparation.

3.4 Basic characterization

The following techniques will be utilized to investigate the basic properties and structure of CNFs decorated with NiO/C NPs :

3.4.1 Field Emission Scanning Electron Microscope (FE-SEM)

Field-emission scanning electron microscopy (FE-SEM) is a type of electron microscope that utilizes electrons instead of light for imaging. Although it operates on principles similar to those of conventional scanning electron microscopy (SEM), FE-SEM uses a sharp tungsten tip to emit electrons via field emission rather than relying on a thermionically heated cathode. The emitted electrons are focused into a narrow beam by a series of electromagnetic lenses, and scanning coils located near the electron column precisely control and direct this focused beam across the sample surface. Electrons emitted from the sample surface are then captured by detector. The intensity of the detected signal is converted into image brightness and displayed on a monitor (Ahmad et al., 2021), as shown in Figure 3.4. FE-SEM is commonly performed under high vacuum conditions to prevent interference from ambient gas molecules. These gases can disrupt both the incident electron beam and the emitted secondary or backscattered electrons, which are crucial for generating high-resolution images (Jaya, 2020). In this study, we used FE-SEM (FESEM, Carl Zeiss AURIGA) to study the morphology of CNFs decorated with NiO/C.

3.4.2 Transmission Electron Microscope (TEM) with Selected Area Electron Diffraction (SAED) and Energy Dispersive Spectroscopy (EDS)

Figure 3.4 presents a diagram of a transmission electron microscope (TEM), which comprises an electron source, a system of electromagnetic lenses, and detectors. In TEM analysis, a high-energy electron beam is focused into a thin, parallel beam using a series of condenser lenses and directed through the sample. The interaction between the transmitted electrons and the sample produces high-resolution images, which are essential for analyzing the internal morphology and examining chemical structure at the atomic scale of the samples (Nasrollahzadeh et al., 2019). In addition, Selected Area Electron Diffraction (SAED) is a crystallographic technique used in TEM to obtain diffraction patterns from a specific, localized area of a sample (Agrawal, 2022). SAED patterns can exhibit sharp points characteristic of single crystals, ring patterns indicative of nanocrystalline powder, or diffuse ring patterns associated with amorphous samples, depending on the sample type.

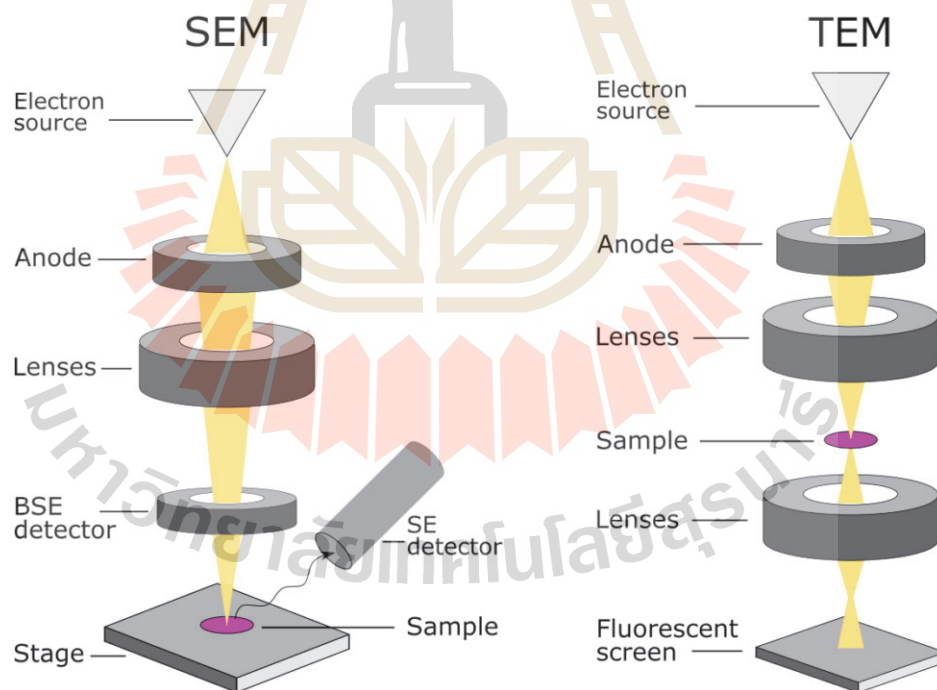


Figure 3.4 A schematic of scanning electron microscope (SEM) and transmission electron microscope (TEM) diagram .

Furthermore, In the TEM, the Energy-dispersive X-ray spectroscopy (EDS) operates by detecting the characteristic X-ray energies emitted from a sample upon exci-

tation by a high-energy electron or X-ray beam. These X-rays possess element-specific energies, thereby enabling both qualitative and quantitative analysis of the elemental composition (Neikov and Yefimov, 2019). EDS was used to investigate the elemental composition of the sample, which has a very small area. In this study, we utilized TEM with SAED, and EDS (TEM, Thermo Scientific TALOS F200X) to study the morphology, crystal structure, and elemental composition of the samples.

3.4.3 X-ray Diffraction (XRD)

X-ray diffraction (XRD) is mostly employed to study the phase composition, crystallite size, and structural parameters of materials. The XRD technique operates by directing X-rays onto a sample, which induces diffraction and reflection at various angles, which are then detected by a detector. The underlying principle of XRD is Bragg's law, mathematically represented in Equation (3.1). The intensity and angles of the diffracted X-rays vary depending on the composition of the material and the crystal structure. Therefore, in this work, XRD analysis (XRD, Bruker D8 Advance diffractometer) was performed to investigate the elemental composition and lattice structures of the prepared samples.

$$2d\sin\theta = n\lambda \quad (3.1)$$

3.4.4 Fourier-Transform Infrared Spectroscopy (FTIR)

Fourier-Transform Infrared (FTIR) spectroscopy is based on the absorption of infrared radiation by molecules, in which transmitted light is collected by an interferometer and subjected to Fourier transformation to produce the infrared spectrum of the sample (Melles et al., 2007; Novais et al., 2019). When infrared light is directed onto a sample, the molecules absorb specific frequencies of the radiation corresponding to the vibrational modes of their chemical bonds. Each type of molecule exhibits characteristic absorption patterns, as the absorbed frequencies align with the natural vibrational frequencies of their chemical bonds within the molecule (Khan et al., 2018), as shown in Figure 3.5. In this work, FTIR (FT-IR Microscope/TENSOR 27-Hyperion-2000) was employed to identify and analyze the functional groups present in the samples.

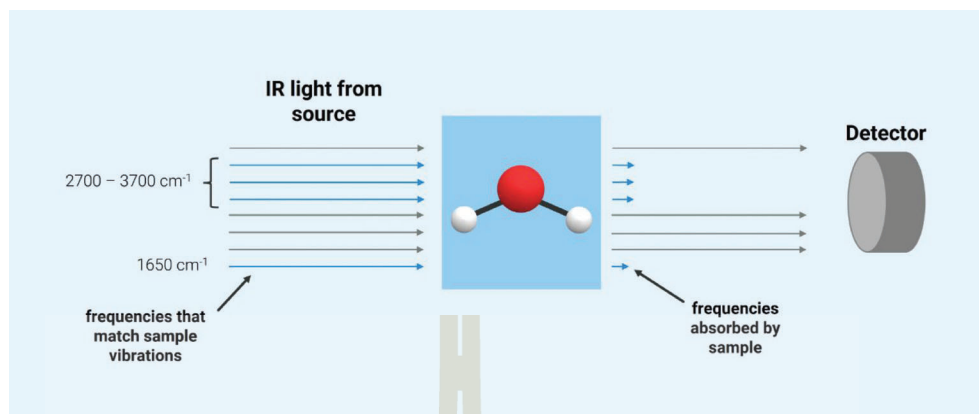


Figure 3.5 Infrared spectroscopy measures the interaction of infrared radiation with matter (Bruker Corporation, n.d.).

3.4.5 Raman Spectroscopy (Raman)

Raman spectroscopy is a non-destructive chemical analysis technique based on the Raman effect, wherein incident light undergoes inelastic scattering at wavelengths differing from the original due to molecular vibrational, rotational, or electronic transitions. These wavelength changes correspond to changes in the vibrational energy levels of the molecules, thereby providing insights into their structural and chemical characteristics (Mitsutake et al., 2019). As a result, we utilized Raman (Renishaw inVia Reflex Raman, UK) to analyze the molecular structure of substances, and also functional groups and their distribution in our samples.

3.4.6 X-ray Absorption Spectroscopy (XAS)

X-ray absorption spectroscopy (XAS) is a technique used to examine the properties of materials by stimulating atoms with X-rays, which excite core electrons residing in localized states. When the photon energy matches the binding energy of these electrons, a characteristic absorption edge appears. The absorption is then measured as a function of photon energy (Fracchia et al., 2018), as shown in Figure 3.6. The resulting absorption spectrum provides information on the local atomic structure, including coordination environment, oxidation state, and bond distances within the sample. Therefore, XAS was employed to study the oxidation state of the NiO/C NPs embedded within CNFs. The measurements were conducted in fluorescent mode at the SUT-NANOTEC-SLRI XAS beamline BL5.2, Synchrotron Light Research Institute (SLRI), Thailand.

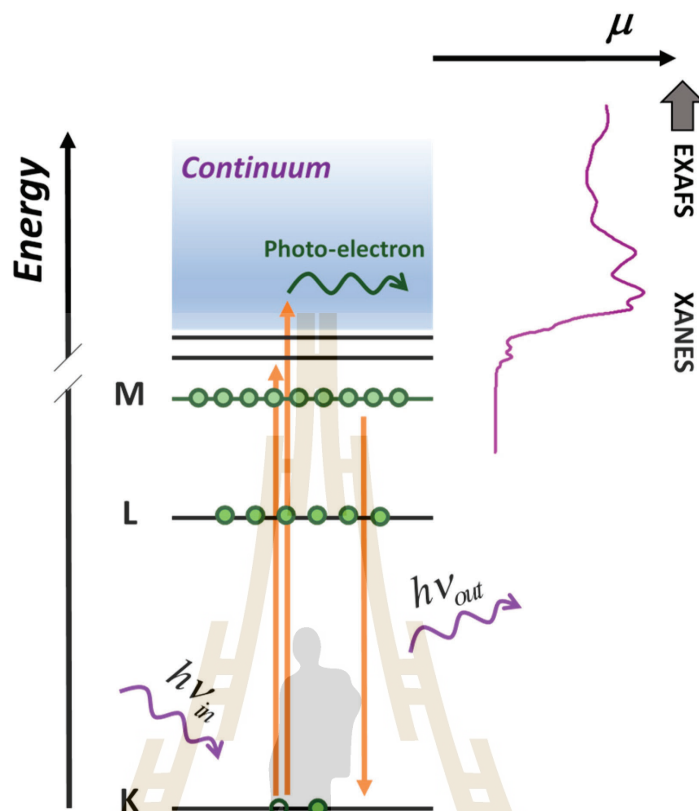


Figure 3.6 Schematic of the principle of XAS (Fracchia et al., 2018).

3.4.7 X-ray Photoelectron Spectroscopy (XPS)

X-ray photoelectron spectroscopy (XPS) is a technique used to identify the elemental composition and chemical bonding states present on a surface of material. The method employs soft X-ray radiation to induce photoelectron emission. Figure 3.7 illustrates the schematic representation of the XPS principle. When atoms absorb the incident X-ray energy, electrons are activated and electrons ejected from their inner orbitals called photoelectric absorption. The kinetic energy (KE) of the emitted electrons is measured and used to calculate the binding energy (BE), which is a characteristic of the specific element and its chemical environment. Since each element exhibits a unique binding energy, XPS enables precise elemental, bonding structure and chemical state identification (Greczynski and Hultman, 2020). As a result, we used XPS analysis with the XPS PHI5000 VersaProbe II instrument (ULVAC-PHI, Japan) at the SUT-NANOTEC-SLRI Joint Research Facility to study the elemental composition of our CNFs decorated with NiO/C surface.

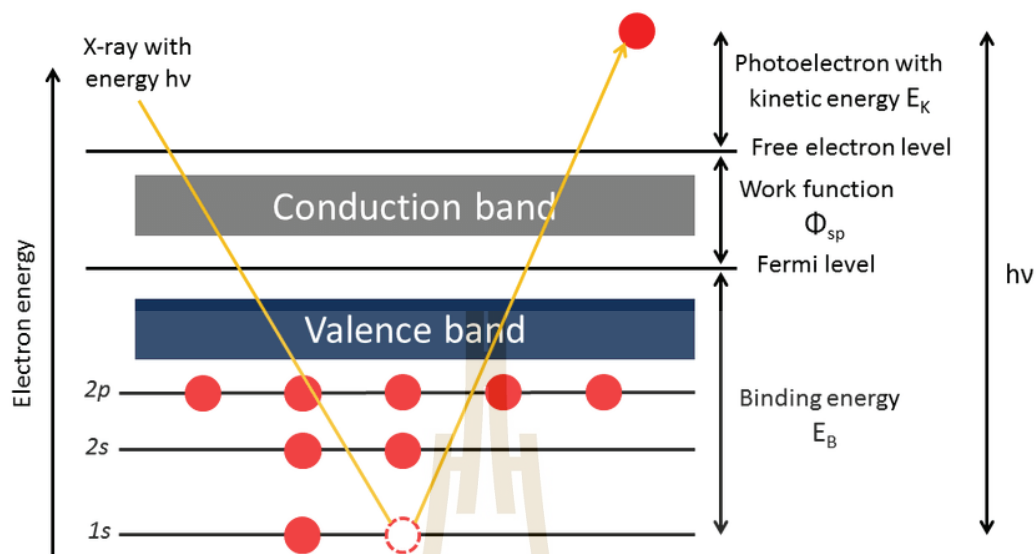


Figure 3.7 Schematic of the principle of XPS (Vandenbroucke, 2015).

3.4.8 Brunauer-Emmett-Teller (BET)

The Brunauer-Emmett-Teller (BET) specific surface area analysis is one of the most commonly used techniques for evaluating the effective surface area of adsorbents, catalysts, and a variety of porous materials. Figure 4.14 shows principles of the BET methods. This analysis is based on the adsorption isotherms of nonreactive gas molecules, such as N_2 at 77 K over a range of relative pressures that encompasses monolayer adsorption. The resulting isotherms are then transformed into a linearized BET plot to calculate the surface area. The collected data are typically presented in the form of adsorption-desorption isotherms (Sing, 1998). So, we used BET to analyze the pore size diameter, specific surface area, and pore volume of our samples.

3.5 Electrochemical characterization

The Electrochemical measurements were performed using a Metrohm Autolab electrochemical workstation (PGSTAT302N) with a three-electrode system in a 2 M KOH aqueous electrolyte. In the measurements, as-prepare electrode was used as working electrode, platinum rod and the silver/silver chloride electrode (Ag/AgCl) was used as counter electrode and reference electrode, respectively. The prepared electrodes were tested using a cyclic voltammetry (CV) technique, galvanostatic charge-discharge (GCD) technique and electrochemical impedance spectroscopy (EIS).

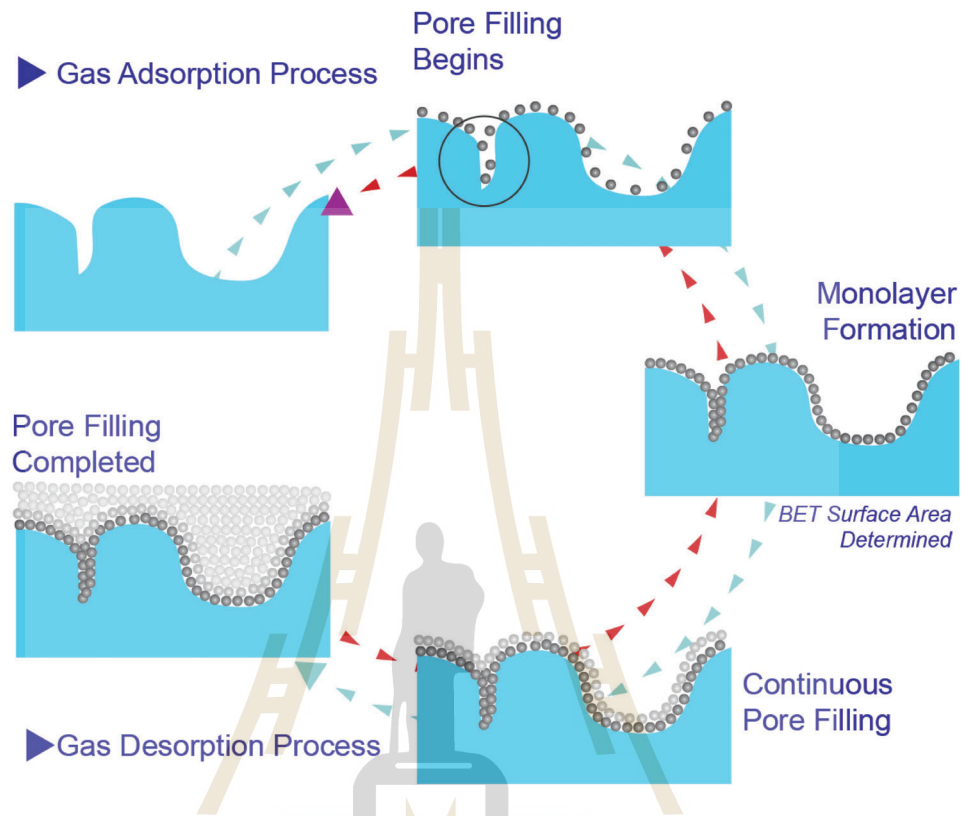


Figure 3.8 Principles of the BET methods (Particle Technology Labs, n.d.).

3.5.1 Cyclic voltammetry (CV)

Cyclic voltammetry (CV) is an electrochemical technique used to study the efficiency of supercapacitors. The data obtained from cyclic voltammetry are plotted in graphs where the y-axis is the current density ($A\ g^{-1}$) and the x-axis is the applied potential (V), as shown in Figure 3.9. The obtained data can be analyzed to determine the maximum oxidation and reduction values, which are obtained by redox reactions in the voltammetry circuit, the amount of charge accumulated at the electrode surface. This charge accumulation is directly related to the specific capacitance of the material, which can be calculated as follows in equation (3.2) (Kar, 2020a, 2020b).

$$C_s = \frac{\int I dV}{\nu_m(\Delta V)}, \quad (3.2)$$

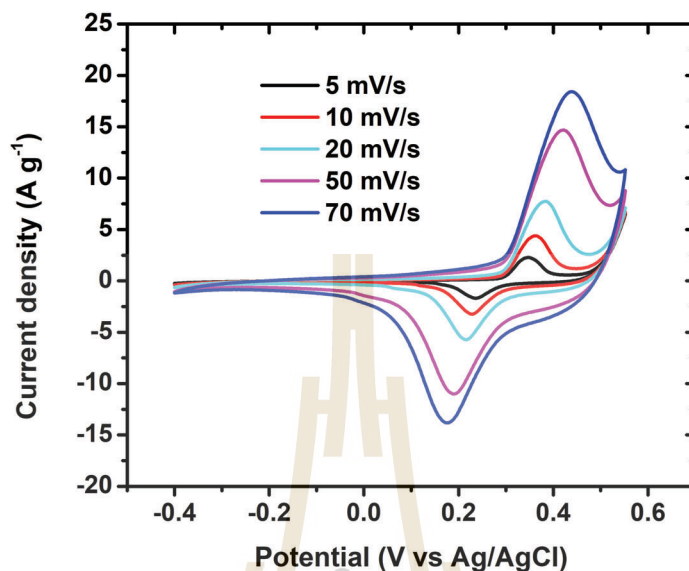


Figure 3.9 The CV curves of NiO/C NPs electrode at various scan rates of 5–70 mV s⁻¹.

where I is the constant current, ν is the scan rate, m is the active mass of prepared electrode and ΔV is the potential window in cyclic voltammograms

3.5.2 Galvanostatic charge-discharge (GCD)

Galvanostatic charge-discharge (GCD) is a technique used to evaluate the electrochemical capacitance of electrodes. GCD works by charging-discharging to the working electrodes at different current density. The data obtained from GCD is plotted on graphs with time on the x-axis and the potential (V) on the y-axis, as shown in Figure 3.10.

The obtained data can be used to calculate the specific capacitance of the supercapacitor by using equation (3.3) from the discharge curves as shown in Figure 3.11. We can also use the GCD to assess the resistance and cyclic stability of the electrode (Kar, 2020a).

$$C_s = \frac{2I \int V dt}{m(\Delta V)^2} \quad (3.3)$$

where $\frac{I}{m}$ is the current density, $\int V dt$ is an area of discharge curve and ΔV is the potential window (Kar, 2020b).

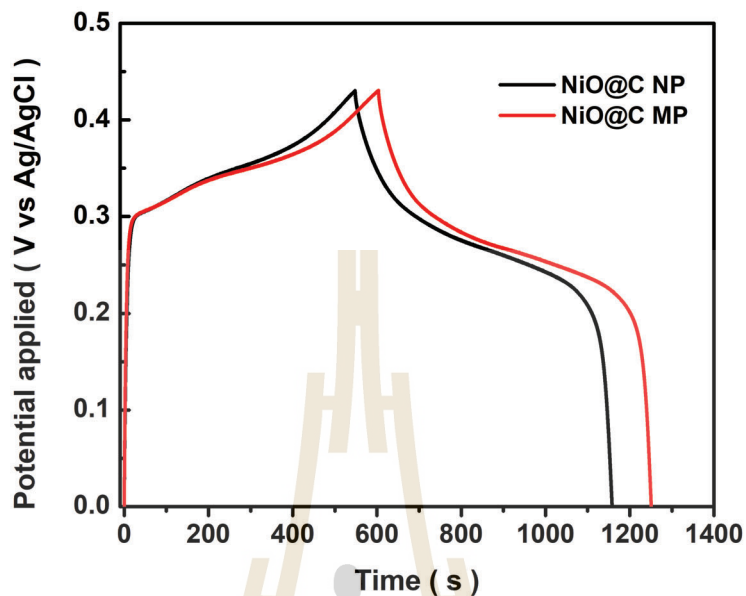


Figure 3.10 The GCD curves of NiO/C nanoparticles (NiO/C NPs) and microparticles (NiO/C MPs) electrodes at a current density of 0.5 A g^{-1} .

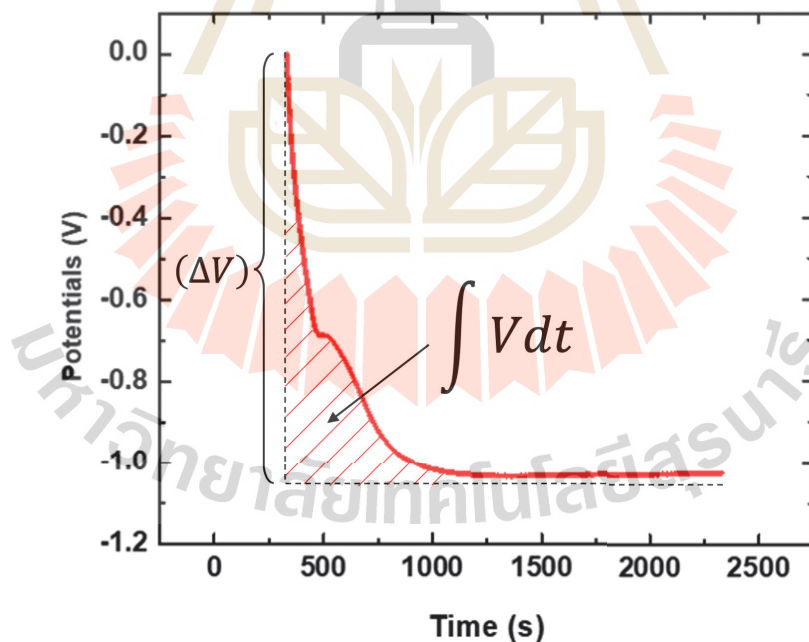


Figure 3.11 Specific capacitance calculated from galvanostatic charge-discharge.

3.5.3 Electrochemical impedance spectroscopy (EIS)

Electrochemical impedance is a tool used to calculate the impedance of an electrode. The data is presented as a Nyquist plot graph, showing the imaginary

and real parts of the impedance on the complex plane, where the intersection of the curves at the x-axis represents the electrolyte resistance of the electrode. In addition, the Nyquist plot graph shows data about the series, charge transfer and ion diffusion resistance. The data obtained can be used to study the characteristics of the electrode materials, the pore size distribution of the electrode materials and particle-particle interaction, etc. (Kar, 2020a, 2020b). To explain various physical processes occurring within the electrode, and at the electrode-electrolyte interface, the entire frequency region is divided into three frequency regions, as shown in Figure 3.12, each of which is assigned to different electrical elements (Ruiz et al., 2008). The x-intercept observed in the high-frequency region is generally known as the equivalent series resistance (ESR) or bulk resistance, denoted as R_s , which is attributed to the collective contribution of resistances from the bulk electrolyte, the electrode material, and the contact resistance between the electrode and the current collector (Yu et al., 2013). Following this region, the semicircular arc, which spans the high to mid-frequency region of the EIS spectrum, whose diameter is the charge transfer resistance (R_{CT}) at the electrode-electrolyte interface. This resistance is associated to the porosity of the electrode, and is attributed to the diffusion, and of electrolyte ions through the porous structure of the material (Fang and Binder, 2006). Furthermore, the nearly vertical line at low frequencies indicates the capacitive behavior of the electrode material, which arises from electric double-layer capacitance (EDLC) and/or pseudocapacitance (C.-L. Liu et al., 2007).

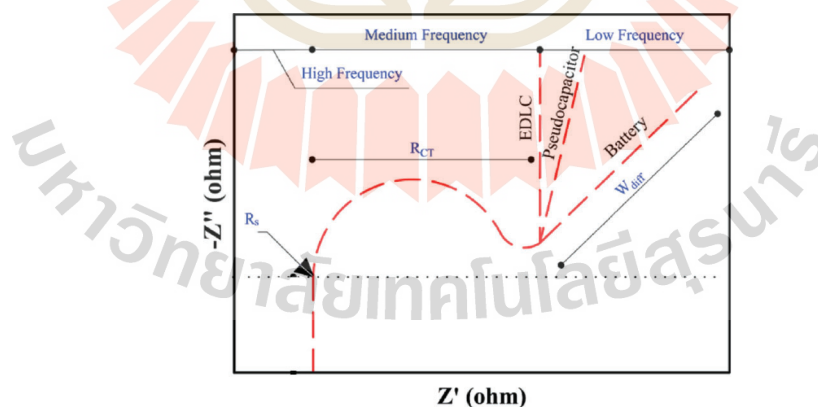


Figure 3.12 The Nyquist plot diagram with key regions labelled (Mevada and Mukhopadhyay, 2023).

CHAPTER IV

RESULTS AND DISCUSSION

4.1 Basic Characterization

The surface morphologies of CNFs-Bare, CNFs-5NiO/C NPs, CNFs-10NiO/C NPs, and CNFs-15NiO/C NPs were examined using FE-SEM, as shown in Figure 4.1a–d. The FE-SEM images show that the CNFs mats consist of nanofibers arranged in overlapping, crossed patterns with a uniform nanoscale diameter distribution. The diameters of the nanofibers for CNFs-Bare, CNFs-5NiO, CNF-10NiO, and CNF-15NiO are 337 ± 15 nm, 330 ± 16 nm, 333 ± 22 nm, and 316 ± 23 nm, respectively, as shown in Figure 4.2a–d. The diameter measurements were analyzed and quantified using ImageJ software. The uniform diameter of the carbon nanofibers is attributed to the good controllability of the electrospinning process.

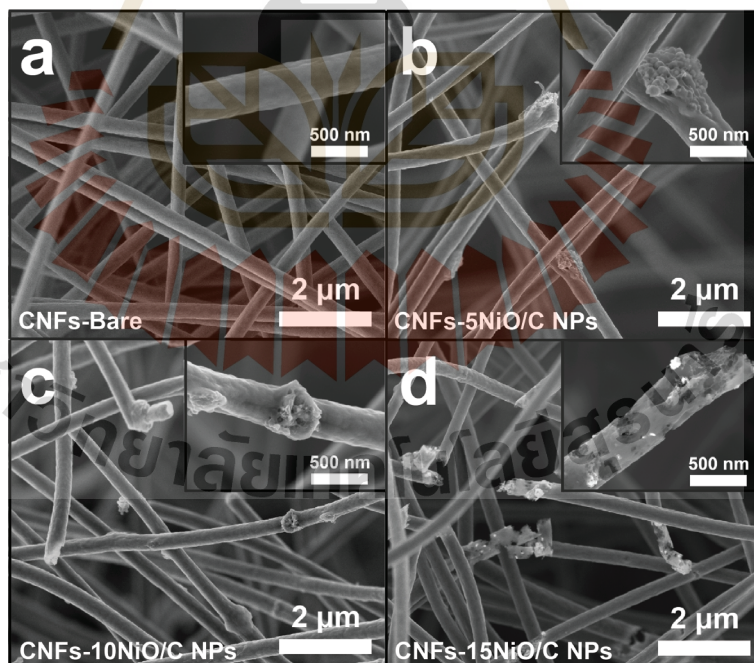


Figure 4.1 FE-SEM images of (a) CNFs-Bare, (b) CNFs-5NiO/C NPs, (c) CNFs-10NiO/C NPs and (d) CNFs-15NiO/C NPs at a magnification of 10 kx with the insets of (a)-(d) representing their FESEM images at 50kx magnification.

Figure 4.1b–d present the FESEM image of CNFs-5NiO/C NPs, CNFs-10NiO/C NPs, and CNFs-15NiO/C NPs. The surface morphology of the CNFs-NiO/C NPs reveals that the NiO/C NPs are embedded within the CNFs matrix. Notably, the quantity of these nanoparticles visibly increases with the rising NiO/C NPs concentration within the polymer precursor solution. In contrast, the surface of CNFs-Bare, prepared without the addition of NiO/C nanoparticles in the polymer precursor, exhibits a smooth morphology with no observable nanoparticle decoration as shown in Figure 4.1a. The insets of Figure 4.1a–d reveal the embedding characteristics of NiO/C nanoparticles within the CNFs containing NiO/C NPs. The decoration of NiO/C NPs into the CNFs matrix may enhance surface porosity and increase the interfacial contact area, which in turn contributes to improved electrochemical performance. This will be discussed in the BET analysis part.

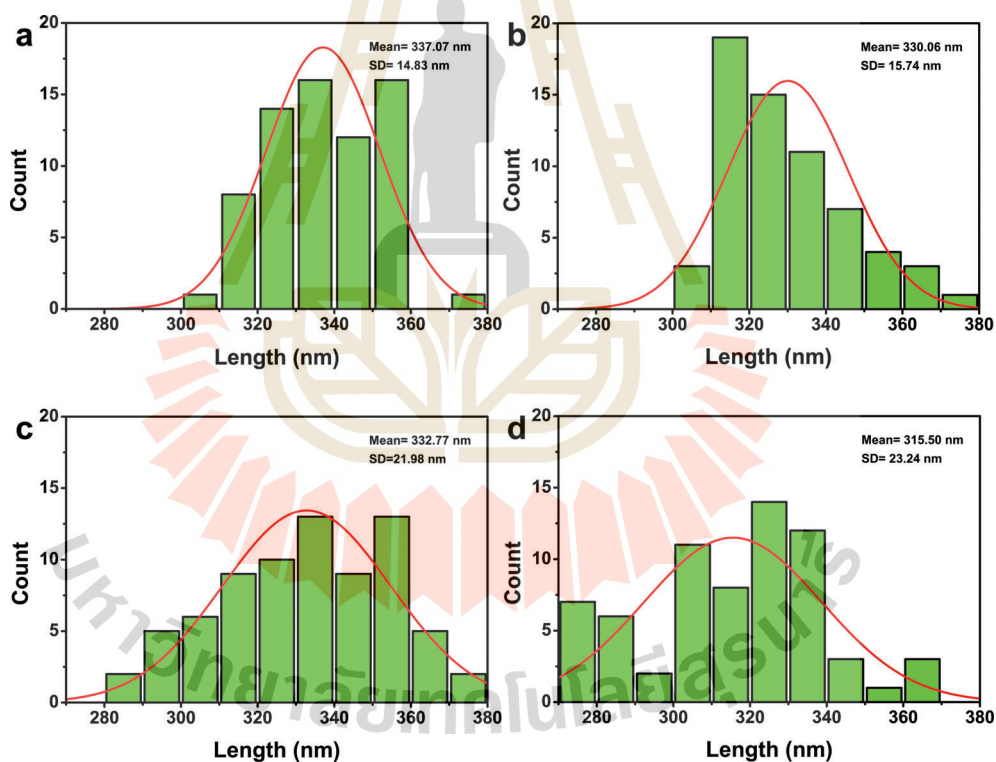


Figure 4.2 Histogram of diameter distribution of (a) CNFs-Bare, (b) CNFs-5NiO/C NPs, (c) CNFs-10NiO/C NPs and (d) CNFs-15NiO/C NP.

The TEM was employed to examine the internal structures of prepared carbon nanofibers. Figure 4.3a–d present TEM images of CNFs-Bare, CNFs-5NiO/C NPs, CNFs-10NiO/C NPs, and CNFs-15NiO/C NPs, respectively. The image of CNFs-Bare reveals smooth nanofibers without any observable particles embedded in the CNFs. In

contrast, the TEM images of CNFs-5NiO/C NPs, CNFs-10NiO/C NPs, and CNFs-15NiO/C NPs reveal carbon nanofiber structures with clearly embedded nanoparticles, indicating successful incorporation of NiO/C within the CNFs matrix. In addition, the number of nanoparticles embedded within the carbon nanofibers tends to increase proportionally with the concentration of NiO/C NPs added into the polymer precursor. The incorporation of nanoparticles into the nanofibers enhances their porosity and increases the surface area, as illustrated in the inset of Figure 4.3. Thus, the obtained TEM observations are consistent with the results from the FE-SEM analysis, confirming the successful preparation of CNFs decorated with NiO/C NPs as a composite material.

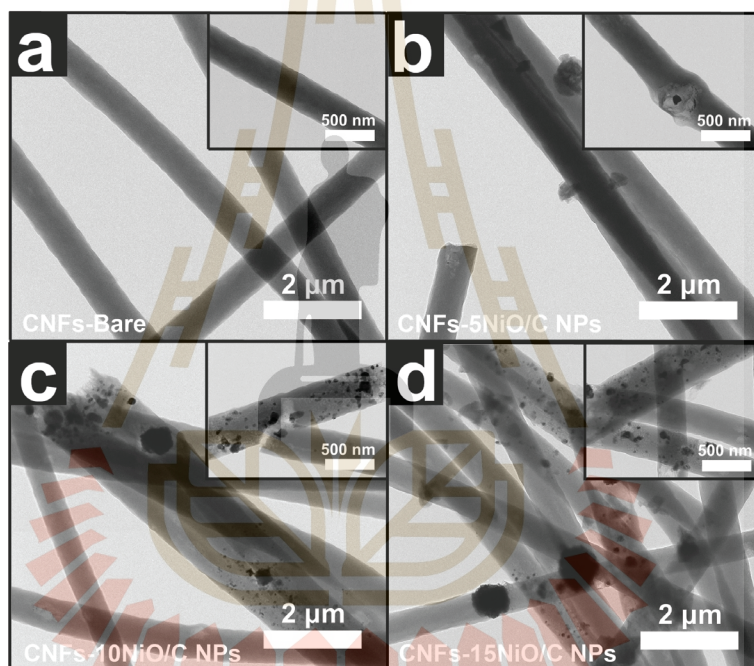


Figure 4.3 TEM images of (a) CNFs-Bare, (b) CNFs-5NiO/C NPs, (c) CNFs-10NiO/C NPs and (d) CNFs-15NiO/C NP with the insets of (a)-(d) representing their higher magnification of TEM images.

The detailed structure of the CNFs decorated with NiO/C NPs was examined using high-resolution TEM (HRTEM). The HRTEM image of the CNFs-15NiO/C NPs sample reveals the terminal region of the nanofiber, confirming the presence of small nanoparticles embedded within the CNFs matrix, as shown in Figure 4.4. Furthermore, the lattice spacings of 0.24, and 0.20 nm were measured for the embedded nanoparticles using ImageJ software. These values correspond to the interplanar distances of (111) and (200) of the NiO phase (Rakshit et al., 2013; Ye and Guan, 2019), respectively. The

nanoparticles are surrounded by regions of amorphous carbon.

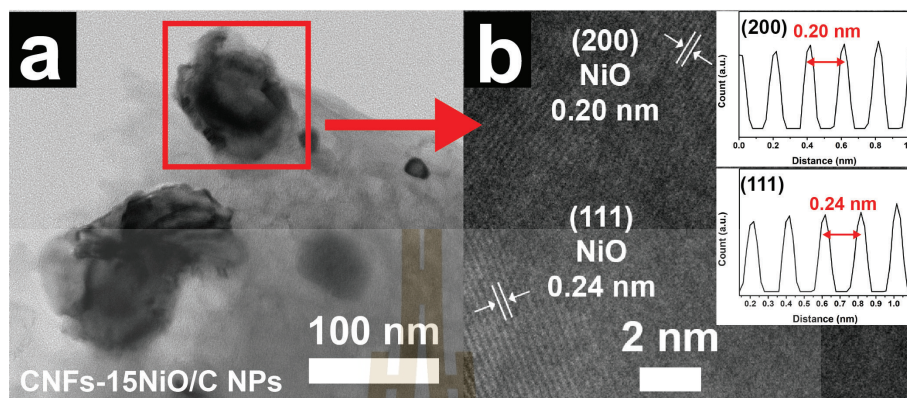


Figure 4.4 (a) The TEM image of CNFs-15NiO/C NPs at the magnification of 120kx, and (b) the HRTEM image of CNFs-15NiO/C NPs along with the lattice spacing.

Figure 4.5a–e show the selected area electron diffraction (SAED) patterns of NiO/C NPs, CNFs-Bare, CNFs-5NiO/C NPs, CNFs-10NiO/C NPs, and CNFs-15NiO/C NPs, respectively. The diffraction rings from the NiO/C NPs were indexed to a mixed phase containing both NiO and metallic Ni, showing a cubic lattice structure as summarized in Table 4.1. These rings correspond to the (111), (200), (220) and (311) planes of NiO, as well as the (111), (220), and (311) planes of Ni (Balu et al., 2012; Dilmukhambetov et al., 2013; Richardson et al., 2003). On the other hand, the SAED pattern of the CNFs-Bare sample does not exhibit any diffraction rings, indicating an amorphous carbon structure (Saleemi et al., 2019). Moreover, the SAED pattern of the CNFs-5NiO/C NPs, CNFs-10NiO/C NPs, and CNFs-15NiO/C NPs sample exhibit diffraction rings characteristic of both NiO/C NPs and CNFs-Bare, indicating the presence of NiO, Ni, and amorphous carbon phases.

The elemental composition of the electrode materials was analyzed through energy-dispersive X-ray spectroscopy (EDS). In this study, EDS was employed to identify the constituent elements of CNFs-Bare and CNFs-15NiO/C NPs, as shown in Figure 4.6(a) and (b), respectively. The EDS spectrum of CNFs-Bare reveals the presence of carbon (C), nitrogen (N), and oxygen (O), confirming the expected elemental composition of the bare carbon nanofibers. In contrast, the EDS spectrum of CNFs-15NiO/C NPs exhibits additional peaks corresponding to nickel (Ni), along with those of C, N, and O. This observation confirms the successful incorporation of NiO/C NPs into the CNFs matrix, which will be further verified by X-ray diffraction analysis.

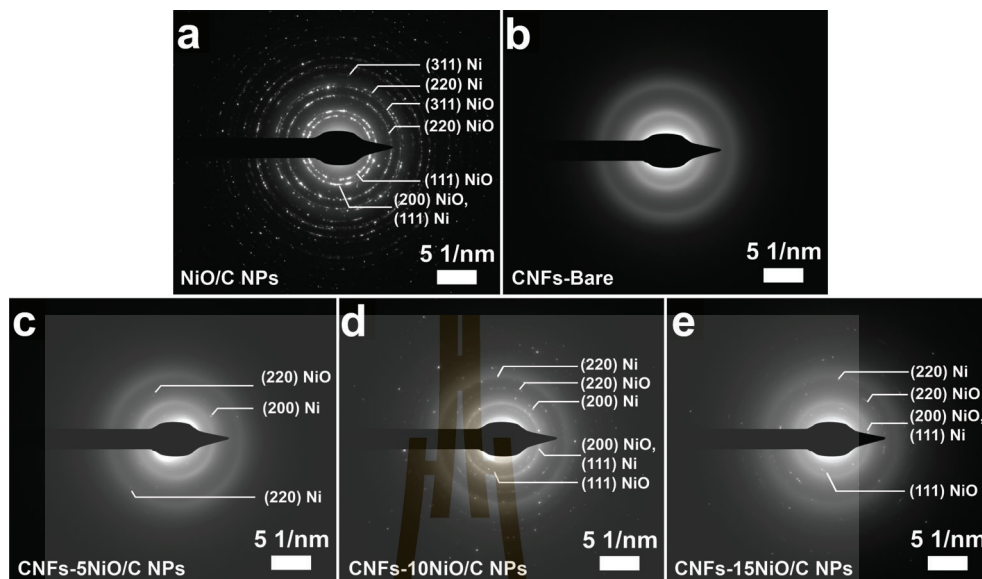


Figure 4.5 SAED rings of (a) NiO/C NPs, (b) CNFs-Bare, (c) CNFs-5NiO/C NPs, (d) CNFs-15NiO/C NPs, and (e) CNFs-15NiO/C NPs.

Table 4.1 Interplanar distances (d -spacings) for electron diffraction patterns of NiO/C NPs and CNFs-10NiO/C NPs.

Sample	Phase	hkl	$d_{(hkl)}$ (Å)	Sample	Phase	hkl	$d_{(hkl)}$ (Å)
NiO/C NPs	NiO	111	2.46	CNFs-5NiO/C NPs	Ni	200	1.85
	NiO,Ni	200,111	2.10		NiO	220	1.56
	NiO	220	1.51		Ni	220	1.20
	NiO	311	1.29	CNFs-10NiO/C NPs	NiO	111	2.41
	Ni	220	1.24		NiO,Ni	200,111	2.03
	CNFs-15NiO/C NPs	Ni	311		1.06	Ni	200
CNFs-15NiO/C NPs		NiO	111		2.45	NiO	220
		NiO,Ni	200,111	2.10	Ni	220	1.24
CNFs-15NiO/C NPs		NiO	220	1.50	NiO	111	2.45
		Ni	220	1.29	NiO,Ni	200,111	2.10

EDS mapping was performed to verify the elemental distribution in the prepared carbon nanofibers. Figure 4.7 presents the EDS elemental mapping of the CNFs-15NiO/C NPs sample. The elemental analysis confirms the presence of C, O, N, and Ni

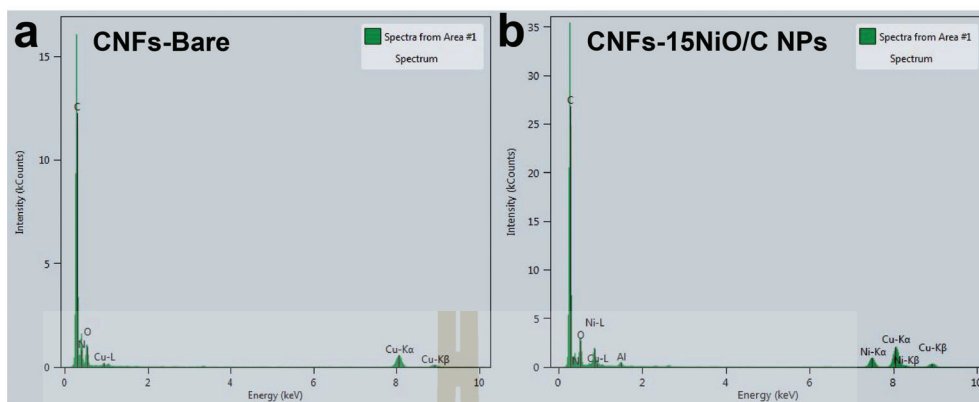


Figure 4.6 EDS spectra of a) CNFs-Bare, and CNFs-15NiO/C NPs with their element.

within the CNFs-15NiO/C NPs sample. The distribution maps show that C, O, and N are uniformly dispersed along the entire length of the CNFs. Notably, regions with elevated Ni concentrations overlap with areas of increased O intensity, corresponding to the locations of NiO particles embedded within the CNFs matrix. These findings confirm the successful integration of NiO/C nanoparticles into the carbon nanofiber structure.



Figure 4.7 EDS mapping of CNFs-15NiO/C NPs with their element.

Figure 4.8 presents the XRD pattern of all samples. The pattern for CNFs-NiO/C NPs exhibits a broad peak centered at $2\theta = 25^\circ$, characteristic of the amorphous structure of CNFs derived from PAN nanofibers following the thermal treatment process (H.-F. Lee et al., 2019). This result indicates that the CNFs produced via electrospinning process were successfully carbonized through calcination at 800°C under an argon atmosphere. The XRD pattern of NiO/C NPs exhibits diffraction peaks at 2θ values of 37.30° , 43.4° , 62.9° , and 75.5° , corresponding to the (111), (200), (220), and (311) crystal planes of cubic NiO (ICDD Card No. 01-073-1523), respectively. Additional peaks at

2θ values of 44.6° , 51.9° , and 76.5° correspond to the (111), (200), and (220) planes of metallic Ni (ICDD Card No. 00-004-0850), as shown in Figure 4.8. Moreover, the XRD patterns of CNFs-5NiO/C NPs, CNFs-10NiO/C NPs, and CNFs-15NiO/C NPs exhibit diffraction peaks corresponding to amorphous carbon, cubic NiO (ICDD Card No. 01-073-1523), and metallic Ni (ICDD Card No. 00-004-0850). Notably, the intensity of the peaks associated with NiO and Ni structures increases with higher concentrations of NiO/C NPs in the polymer solution, confirming the successful integration of NiO/C nanoparticles into the CNFs matrix.

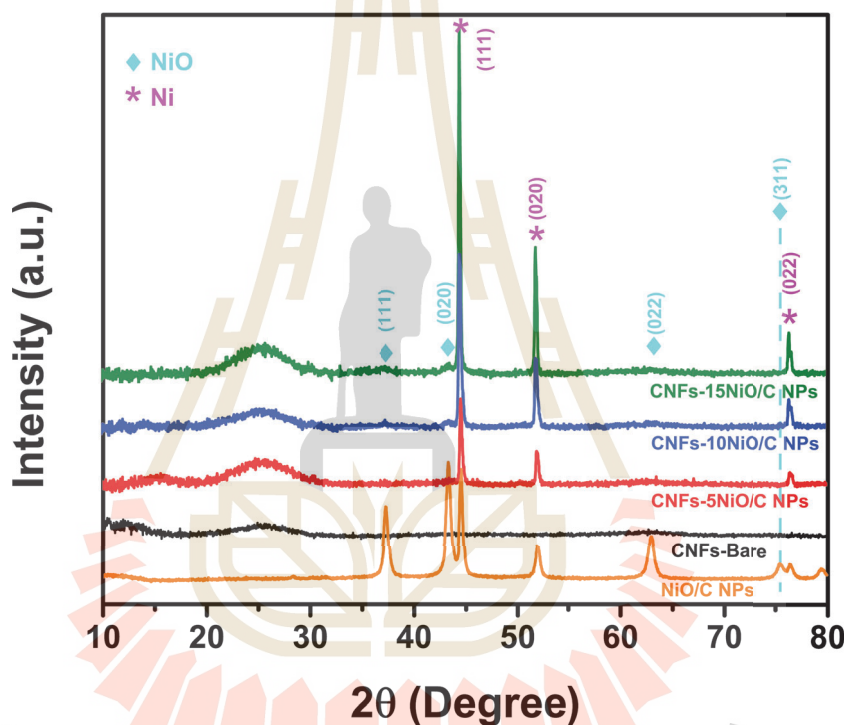


Figure 4.8 XRD pattern of NiO/c NPs, CNFs-Bare, CNFs-5NiO/C NPs, CNFs-10NiO/C NPs and CNFs-15NiO/C NPs.

The FT-IR spectra of all samples provide critical information regarding their functional groups within the wavenumber range of $400\text{--}4000\text{ cm}^{-1}$, as shown in Figure 4.9. The IR spectra of the NiO/C NPs initially exhibits two peaks: the first peak, appearing around 479 cm^{-1} , is attributed to the Ni–O stretching vibration mode (X.-M. Liu et al., 2006; Ren and Gao, 2010), while the second peak, appearing around 692 cm^{-1} , corresponds to the C–O functional species present within the NiO/C nanoparticles (X.-M. Liu et al., 2006). For the FT-IR spectrum of CNFs-Bare, characteristic absorption bands were observed at 1566 cm^{-1} and 1153 cm^{-1} , corresponding to the C=C double bond

and C–C single bond vibrations in the CNFs after the calcination process, respectively (Xu et al., 2020). Notably, the FT-IR spectra of CNFs-5NiO/C NPs, CNFs-10NiO/C NPs, and CNFs-15NiO/C NPs also exhibit characteristic peaks corresponding to the C=C and C–C bonds, indicating the structural features of CNFs. Interestingly, an additional peak observed in the range of 460–480 cm^{-1} is corresponded to the Ni–O bond, confirming the presence of NiO in the CNFs-NiO/C NPs samples, as shown in Figure 4.9. Furthermore, the peaks associated with C–O species observed in the NiO/C NPs disappear after mixing with the polymer solution and undergoing carbonization to form CNFs (X.-M. Liu et al., 2006). These findings are further supported by XRD analysis, which confirms that CNFs-Bare is composed only of carbon. While, the samples containing 5, 10, and 15 wt% NiO/C NPs relative to the PAN weight in the polymer solution exhibit the presence of both Ni and NiO phases within the CNFs matrix.

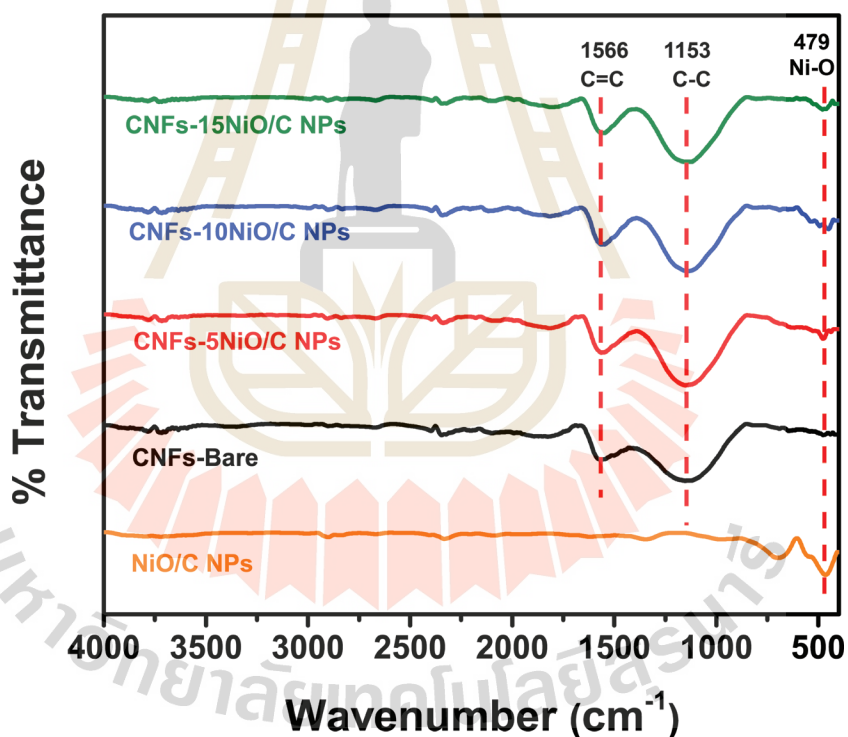


Figure 4.9 FT-IR spectra of NiO/c NPs, CNFs-Bare, CNFs-5NiO/C NPs, CNFs-10NiO/C NPs and CNFs-15NiO/C NPs.

The samples were characterized using Raman spectroscopy (Renishaw inVia Reflex Raman, UK) with an excitation wavelength of 532 nm to investigate their crystal structure and impurities. Raman spectra were recorded at room temperature in the 100–1000 cm^{-1} range. Figure 4.10 presents the Raman spectra of all samples. In the

case of NiO/C NPs, no Raman-active modes are observed for metallic nickel (Ni), as it is a face-centered cubic (FCC) metal with a single-atom primitive unit cell, which lacks the polarizability changes necessary for Raman activity (Lewis and Edwards, 2001). However, the Raman spectrum of NiO/C NPs exhibits peaks at around 350 and 540 cm^{-1} , corresponding to the first-order transverse optical (TO_1) and longitudinal optical (LO_1) phonon modes associated with Ni–O lattice vibrations. In addition, peaks located near 685 cm^{-1} and 1080 cm^{-1} are corresponded to the second-order transverse (TO_2) and longitudinal optical (LO_2) phonon modes of NiO vibrational modes, further confirming the presence and vibrational characteristics of the NiO phase (Mironova-Ulmane et al., 2007; Rong et al., 2015). Moreover, the Raman spectra of CNFs-5NiO/C NPs, CNFs-10NiO/C NPs, and CNFs-15NiO/C NPs exhibit peaks in the ranges of approximately $700\text{--}800\text{ cm}^{-1}$ and $1050\text{--}1070\text{ cm}^{-1}$, corresponding to the TO_2 and LO_2 phonon modes of NiO, respectively. Moreover, these samples also exhibit D and G band, which signify the pr-

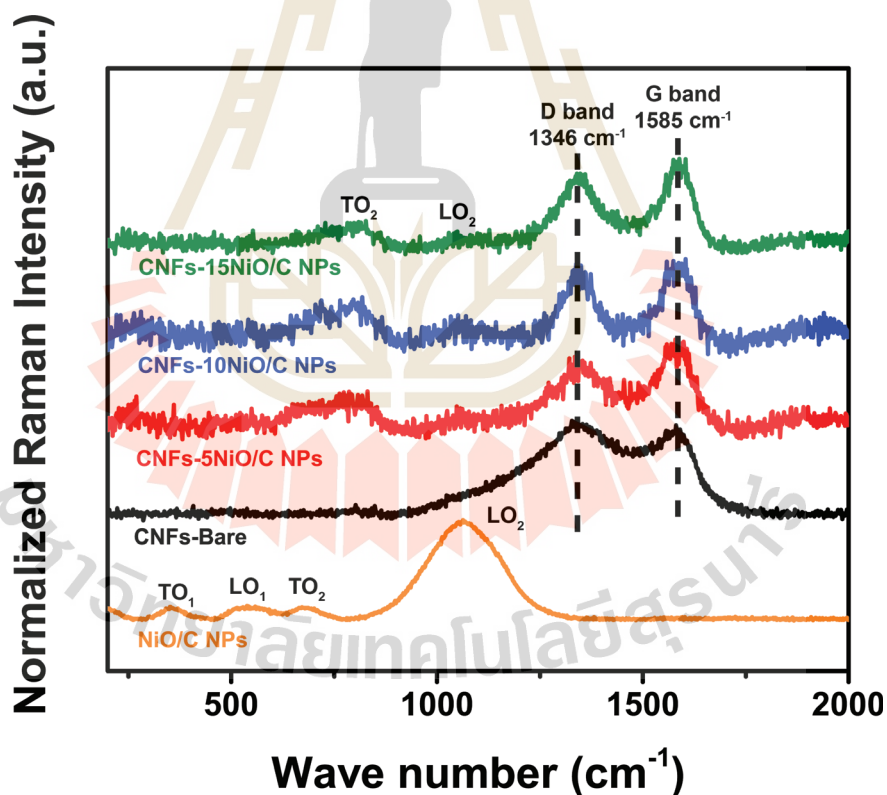


Figure 4.10 Raman spectra of NiO/c NPs, CNFs-Bare, CNFs-5NiO/C NPs, CNFs-10NiO/C NPs and CNFs-15NiO/C NPs.

esence of disordered and graphitic carbon structures within the CNFs, respectively (Cheng et al., 2015; Zhou et al., 2009). The D band appears at approximately 1346

cm^{-1} , while the G band is observed near 1585 cm^{-1} , corresponding to disordered sp^2 (Sankar et al., 2017). In contrast, the Raman spectra of CNFs-Bare displays only the characteristic D and G bands, with no observable peaks corresponding to NiO vibrational modes, thereby confirming the absence of NiO in the sample. These observation align with the results obtained from HRTEM, SAED, XRD, and FT-IR analysis.

X-ray photoelectron spectroscopy (XPS) was used to examine the elemental composition, and oxidation states of the samples in detail. Figure 4.11 presents the survey XPS spectra of CNFs-Bare, and CNFs-15NiO/C NPs. The spectrum of CNFs-Bare verifies the existence of O 1s, N 1s, and C 1s, whereas the survey spectrum of CNFs with NiO/C NPs further indicates an existence of Ni 2p, in addition to O 1s, N 1s, and C 1s.

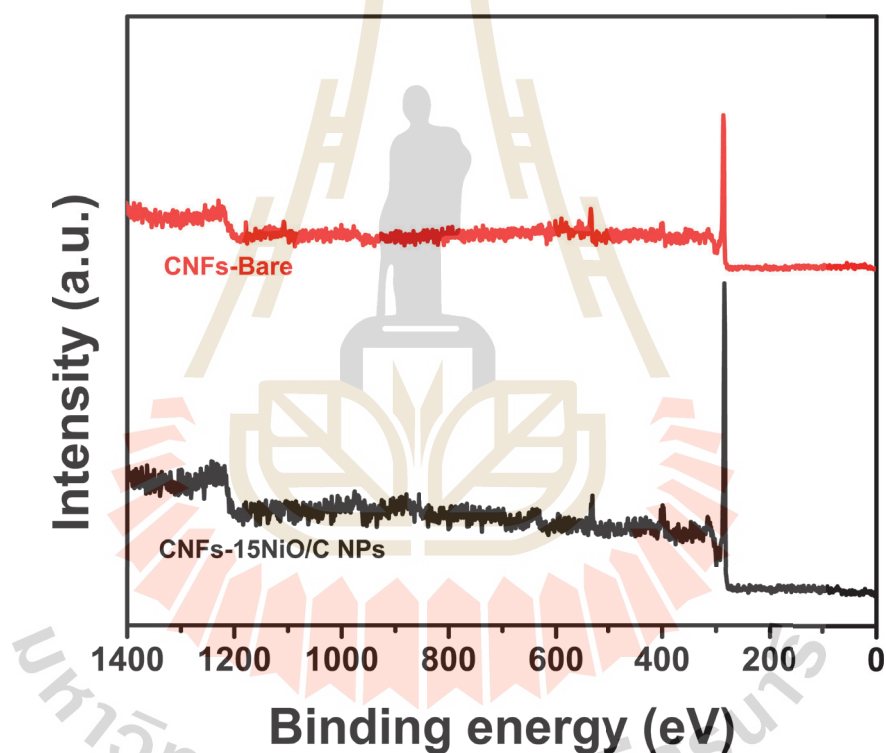


Figure 4.11 the survey XPS spectra of CNFs-Bare, and CNFs-15NiO/C NPs.

The Ni 2p spectrum of CNFs-5NiO/C NPs, CNFs-10NiO/C NPs, and CNFs-15NiO/C NPs, as shown in Figure 4.12a, exhibits spin-orbit splitting into two primary regions: Ni $2\text{p}^{3/2}$ and Ni $2\text{p}^{1/2}$, accompanied by satellite peaks around 860.0 eV and 880.0 eV, respectively. These spectra can be deconvoluted into three distinct pairs of peaks. Each of these pairs corresponds to a unique oxidation state of nickel present in the sample. Metallic nickel (Ni^0) is represented by peaks at 852.4 eV (Ni $2\text{p}^{3/2}$) and 870.0 eV (Ni $2\text{p}^{1/2}$) (Biesinger et al., 2009). The Ni^{2+} state is indicated by peaks at 854.4 eV

and 872.0 eV, while Ni^{3+} is associated with peaks at 856.3 eV ($\text{Ni } 2p^{3/2}$) and 873.8 eV ($\text{Ni } 2p^{1/2}$). Interestingly, the Ni 2p spectrum of CNFs-Bare exhibits a flat profile with no distinct peaks, indicating the absence of nickel species. These features confirm the presence of metallic Ni and NiO in the sample (K. Kim and Winograd, 1974; Salunkhe et al., 2021).

Figure 4.12b presents the O 1s XPS spectra of CNFs-Bare, CNFs-5NiO/C NPs, CNFs-10NiO/C NPs, and CNFs-15NiO/C NPs. For CNFs-5NiO/C NPs, CNFs-10NiO/C NPs, and CNFs-15NiO/C NPs, the O 1s spectra were deconvoluted into four distinct peaks located at 530.0, 531.2, 532.8, and 534.9 eV. The peak at 531.2 eV is attributed to hydroxyl groups ($-\text{OH}$) and carbonyl ($\text{O}=\text{C}$) bonds (Benko et al., 2015; Xiong et al., 2017), while the peak at 532.8 eV corresponds to C–O and carboxylate ($\text{O}=\text{C}-\text{O}$) bonding environments (J. H. Lee et al., 2021; K. Li et al., 2021). The peak at 534.9 eV is associated with adsorbed water molecules (H_2O) (Benko et al., 2015). Interestingly, the peak observed around 530.0 eV indicates the presence of O-metal (O-M) bonds, indicating O–Ni bonding (Xiong et al., 2017). In contrast, the O 1s XPS spectra of CNFs-Bare does not display a peak near 530.0 eV, confirming the absence of O-M bonding in the sample. This observation is consistent with the Ni 2p XPS spectra, which show that only the CNFs-5NiO/C NPs, CNFs-10NiO/C NPs, and CNFs-15NiO/C NPs samples contain NiO and metallic Ni embedded within the CNFs matrix.

The N 1s spectra of all samples, as shown in Figure 4.12c, can be deconvoluted into four peaks located at 398.5, 400.8, 401.9, and 404.0–405.6 eV, corresponding to pyridinic, pyrrolic, graphitic, and oxidized N species, respectively (H.-F. Li et al., 2020; McClure et al., 2012; Roldán et al., 2012). These results show the presence of nitrogen in the samples, which originates from the PAN precursor (Rakhimbek et al., 2024). Moreover, the XPS high-resolution spectra in the C 1s region for CNFs-Bare, CNFs-5NiO/C NPs, CNFs-10NiO/C NPs, and CNFs-15NiO/C NPs are presented in Figure 4.12d. After curve fitting, five distinct peaks were identified at binding energies of 284.8, 286.3, 287.8, and 288.8 eV. The peak at 284.8 eV corresponds to carbon atoms in C–C and C=C bonds (X.-L. Song et al., 2016; W. Wang et al., 2017). The peak at 286.3 eV is associated with C–O and C–N bonds, while the peak at 287.8 eV is attributed to C=O and C=N bonds (J. Y. Lee et al., 2017). Additionally, the peak at 288.8 eV is assigned to the O–C=O functional group (Cong et al., 2021).

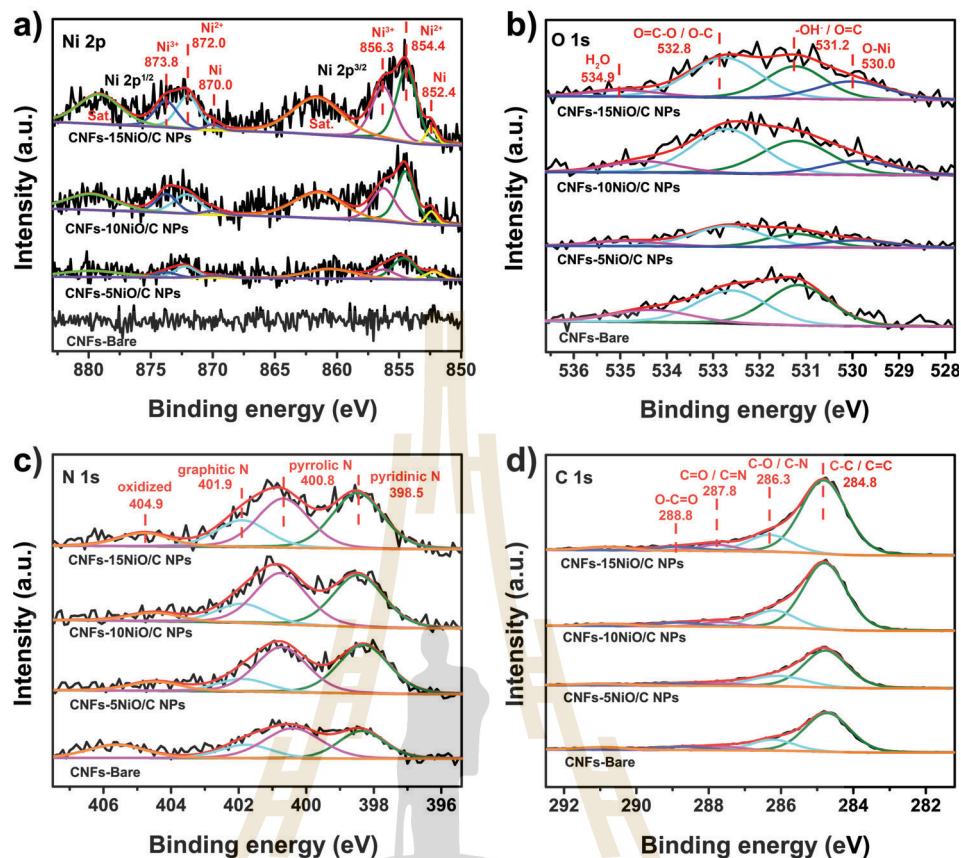


Figure 4.12 XPS high resolution spectra at (a) Ni 2p, and (b) O 1s (c) N 1s, and (d) C 1s regions of CNFs-Bare, CNFs-5NiO/C NPs, CNFs-10NiO/C NPs and CNFs-15NiO/C NPs.

In order to obtain further information on the environment, oxidation state, and the electronic structure of the supported Ni specie, The the X-ray absorption near-edge structure (XANES) in Ni K-edge XAS measurements were carried out. Figure 4.13 shows the Ni K-edge XANES spectra of NiO/C NPs, CNFs-5NiO/C NPs, CNFs-10NiO/C NPs, CNFs-15NiO/C NPs, Ni foil standard (Ni foil std.) and NiO standard (NiO std.). The Ni K-edge XANES spectra of NiO/C NPs, CNFs-5NiO/C NPs, CNFs-10NiO/C NPs, and CNFs-15NiO/C NPs exhibit features similar to those of both the Ni foil and NiO standards, indicating the coexistence of metallic nickel (Ni^0) and divalent nickel (Ni^{2+}). This interpretation is supported by the presence of a pre-edge shoulder characteristic of Ni^0 , resembling that of the Ni foil std. Additionally, although the spectra retain white line features at the first peak near 8350 eV that are characteristic of Ni^{2+} species, the decreased intensity of these features further supports the partial presence of metallic nickel (Ni^0) (Boesenberg et al., 2014). Moreover, the Ni K-edge XANES spectra of CNFs-5NiO/C NPs, CNFs-10NiO/C NPs, and CNFs-15NiO/C NPs also exhibit a distinct peak

labeled as feature B, which corresponds to Ni–Ni scattering and closely matches the spectral characteristics of the Ni foil standard (Denny et al., 2014).

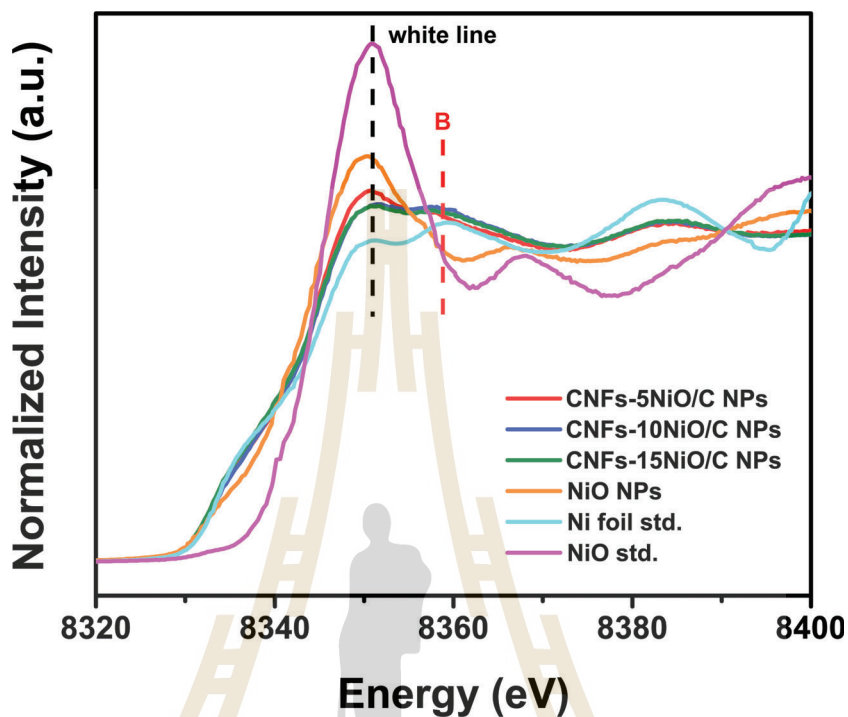


Figure 4.13 Ni K-edge XANES of NiO/C NPs, CNFs-Bare, CNFs-5NiO/C NPs, CNFs-10NiO/C NPs and CNFs-15NiO/C NPs compare with Ni foil and NiO standard.

BET analysis was conducted to evaluate the surface area and pore structure of the samples. The N_2 adsorption–desorption isotherms for CNFs-Bare and CNFs-15NiO/C NPs are illustrated in Figure 4.14. The N_2 adsorption–desorption isotherms of the samples exhibit typical Type IV curves with pronounced hysteresis loops, indicating the presence of mesoporous structures in the materials (Ma et al., 2013).

Table 4.2 reveals that the BET surface area for CNFs-Bare is $487 \text{ m}^2 \text{ g}^{-1}$, while CNFs-15NiO/C NPs exhibits a higher surface area of $513 \text{ m}^2 \text{ g}^{-1}$. This indicates that the incorporation of NiO/C nanoparticles can increase the surface area of the CNFs. Moreover, the average pore size distribution, determined using the Barrett–Joyner–Halenda (BJH) method for CNFs-Bare and CNFs-15NiO/C NPs is 3.6 and 3.9 nm, respectively. Generally, pore sizes are categorized into three classes: micropores (<2 nm), mesopores (2–50 nm), and macropores (>50 nm) (W. Li et al., 2016). Accordingly, both CNFs-Bare and CNFs-15NiO/C NPs exhibit mesoporous characteristics, which facilitate efficient electrolyte ion permeability and diffusion within the electrode material (Xia et al., 2008).

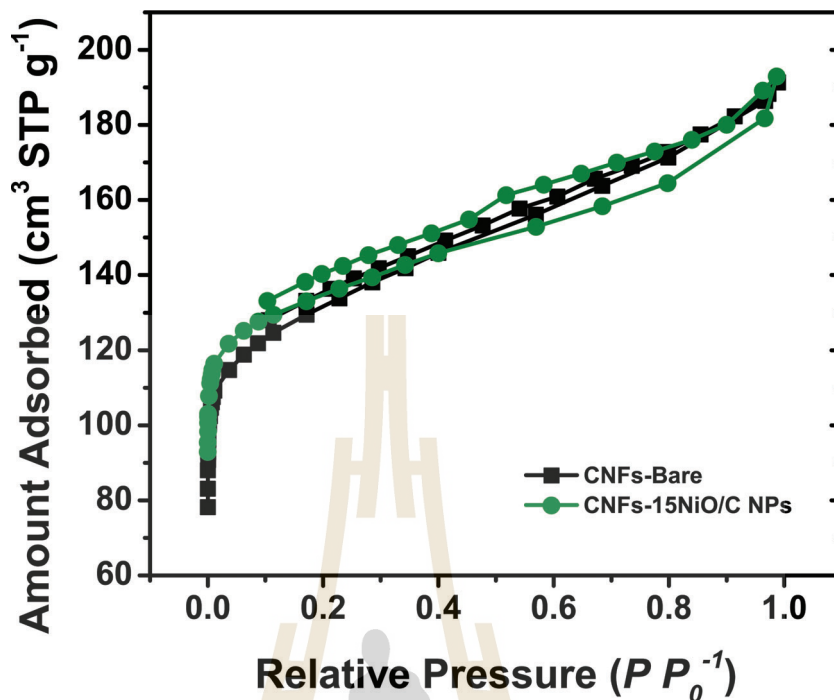


Figure 4.14 The N_2 adsorption–desorption isotherms of CNFs-Bare, and CNFs-15NiO/C NPs.

Table 4.2 Specific surface area and average pore size of sample.

Sample	Surface area ($m_2 g^{-1}$)	Pore size (nm)
CNFs-Bare	487	3.6
CNFs-15NiO/C NPs	513	3.9

4.2 Electrochemical Characterizations

Based on the basic characterization findings, it is apparent that the structural and morphological features of the electrode material may significantly influence its electrochemical performance. To investigate how these features influence the electrochemical performance of the CNFs-NiO/C NPs composite as an electrode material for supercapacitor applications, electrochemical measurements were conducted using a Metrohm Autolab electrochemical workstation (PGSTAT302N) configured in a three-electrode system with 2 M KOH aqueous solution as an electrolyte.

Cyclic voltammetry (CV) measurements were conducted on CNFs-Bare, CNFs-5NiO/C NPs, CNFs-10NiO/C NPs, and CNFs-15NiO/C NPs electrodes within a potential window of 0–0.6 V at different scan rates ranging from 2 to 100 mV s^{-1} , as illustrated in Figure 4.15. In general, NiO-based materials in alkaline electrolytes store charge by reversible redox reactions occurring at the electrode surface (Yuan et al., 2009). As a result, the CV curves of CNFs-5NiO/C NPs, CNFs-10NiO/C NPs, and CNFs-15NiO/C NPs electrodes exhibit distinct shapes compared to those characteristic of electric double-layer capacitance (EDLC). Notably, two redox peaks are observed, corresponding to Faradaic oxidation and reduction processes associated with the reversible transformation between NiO and NiOOH, as described by equation (4.1) (Meher et al., 2011). Moreover, with the scan rate increases, both the anodic and cathodic peak potentials shift toward more positive and negative values, respectively, which is attributed to the faster charge and discharge rate (Elkholy et al., 2017).

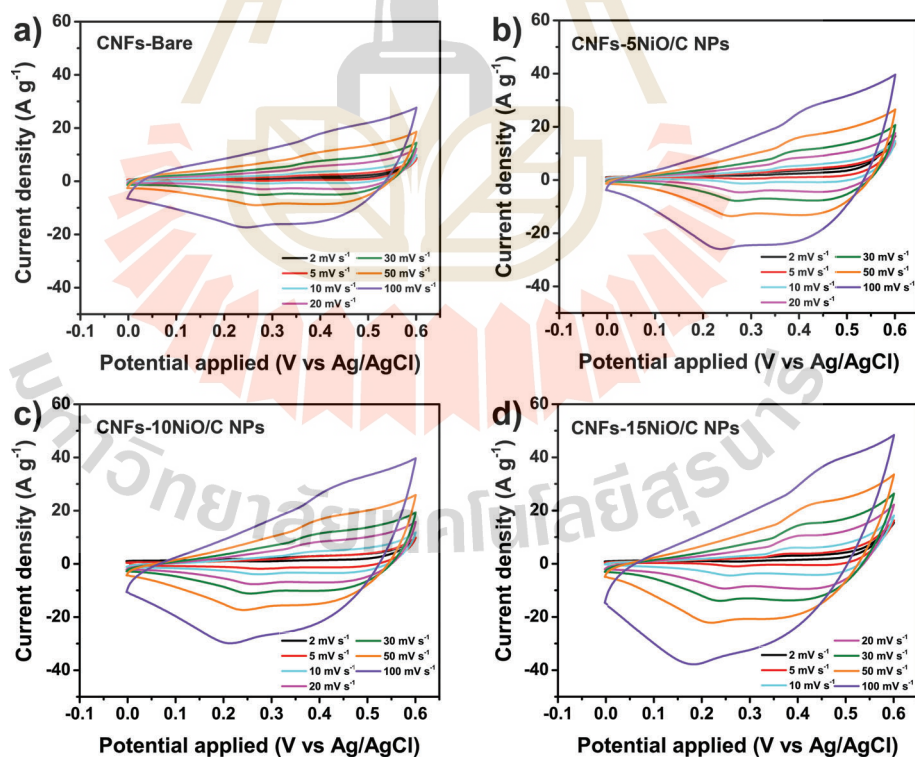


Figure 4.15 CV curves of (a) CNFs-Bare, (b) CNFs-5NiO/C NPs, (c) CNFs-10NiO/C NPs, and (d) CNFs-15NiO/C NPs electrode at various scan rates of 2–100 mV s^{-1} .

In contrast, the CV curves of the CNFs-Bare electrode are not expected to exhibit redox peaks associated with NiO, as it lacks NiO content. Instead, the electrochemical response of pristine CNFs generally displays a quasi-rectangular profile, which is an indication of EDLC behavior (J. Chen, Li, et al., 2002). However, weak redox peaks are still observed, which are corresponded to the redox reactions involving the Cu foam substrate. Since, This redox activity occurs within a similar potential window of the redox reaction between NiO and NiOOH (Lv et al., 2022), thereby potentially overlapping in the voltammogram. Interestingly, the CV curves of CNFs-5NiO/C NPs, CNFs-10NiO/C NPs, and CNFs-15NiO/C NPs electrodes display significantly more pronounced redox peaks compared to the CNFs-Bare electrode, confirming the enhanced redox activity due to the presence of NiO in the CNFs matrix.

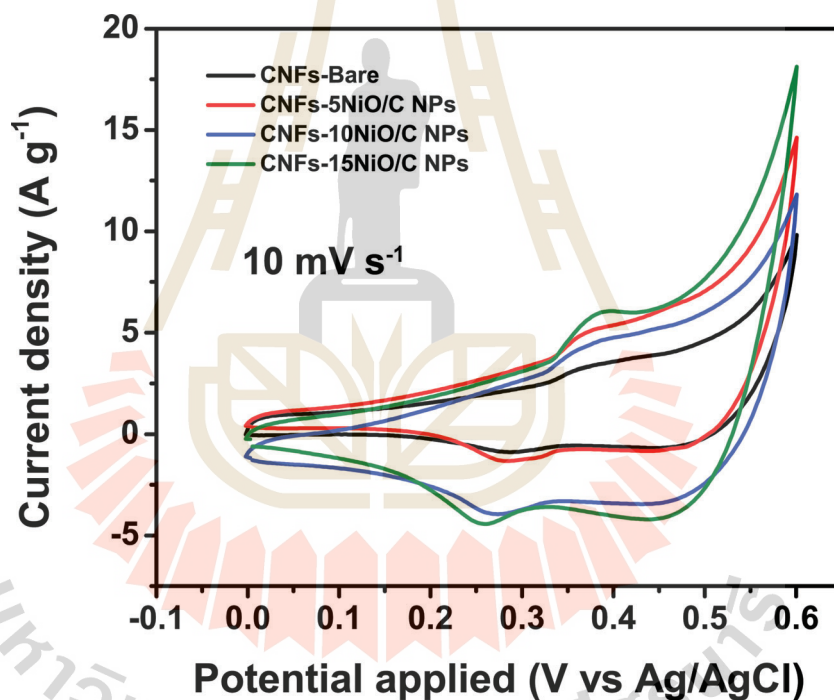


Figure 4.16 CV curves of CNFs-Bare, CNFs-5NiO/C NPs, CNFs-15NiO/C NPs, and CNFs-15NiO/C NPs electrode at a scan rate of 10 mV s^{-1} .

Moreover, when comparing the CV curves of CNFs-Bare, CNFs-5NiO/C NPs, CNFs-10NiO/C NPs, and CNFs-15NiO/C NPs electrodes at a scan rate of 10 mV s^{-1} , it is clear that the CNFs-15NiO/C NPs electrode exhibits the largest area of the CV curve. This observation suggests that the CNFs-15NiO/C NPs electrode possesses the highest capacitance among the CNFs electrodes, as shown in Figure 4.16.

To further investigate the electrochemical characteristics of the electrodes, galvanostatic charge–discharge (GCD) measurements were conducted to assess the charge–discharge behavior of the fabricated electrodes. The GCD tests were performed in a potential window of 0 to 0.45 V at various current densities of 0.5 – 5 A g⁻¹. The charge–discharge curves of the CNFs-Bare, CNFs-5NiO/C NPs, CNFs-10NiO/C NPs, and CNFs-15NiO/C NPs electrodes are shown in Figure 4.17. The observed non-linear characteristics of all charge–discharge curves of CNFs with NiO/C NPs confirm the pseudocapacitive behavior associated with NiO (H. Jiang et al., 2011). However, the GCD curves of CNFs-Bare still exhibit non-linear characteristics, which may be attributed to the redox behavior of the underlying Cu foam substrate. These GCD results are consistent with the findings obtained from the CV analysis.

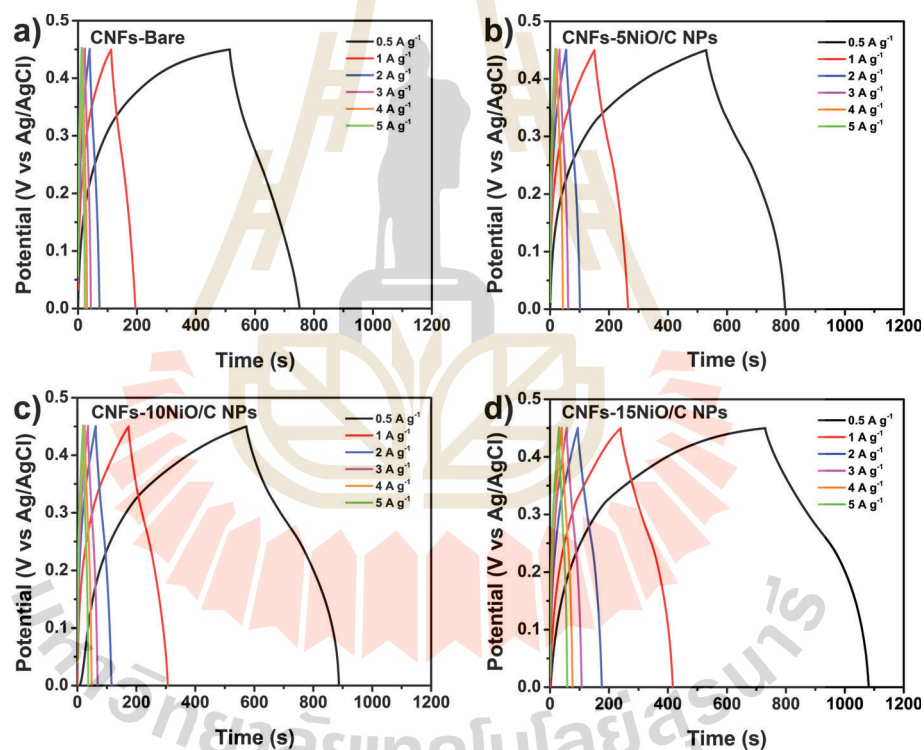


Figure 4.17 GCD charge and discharge curves of (a) CNFs-Bare, (b) CNFs-5NiO/C NPs, (c) CNFs-10NiO/C NPs, and (d) CNFs-15NiO/C NPs electrode at various current densities of 0.5–5 A g⁻¹.

Figure 4.18 presents a comparison of the charge-discharge curves of all electrodes at a current density of 0.5 A g⁻¹. Notably, the CNFs-15NiO/C NPs electrode, containing 15 wt% of NiO/C NPs, shows the longest discharge time compared to the CNFs-Bare, CNFs-5NiO/C NPs, and CNFs-10NiO/C NPs electrodes, indicating enhanced

charge storage performance. This indicates that the CNFs-15NiO/C NPs has better charge storage performance among the samples. This result suggests that the CNFs-15NiO/C NPs electrode exhibits superior charge storage capability compared to the other samples (Reddy et al., 2021).

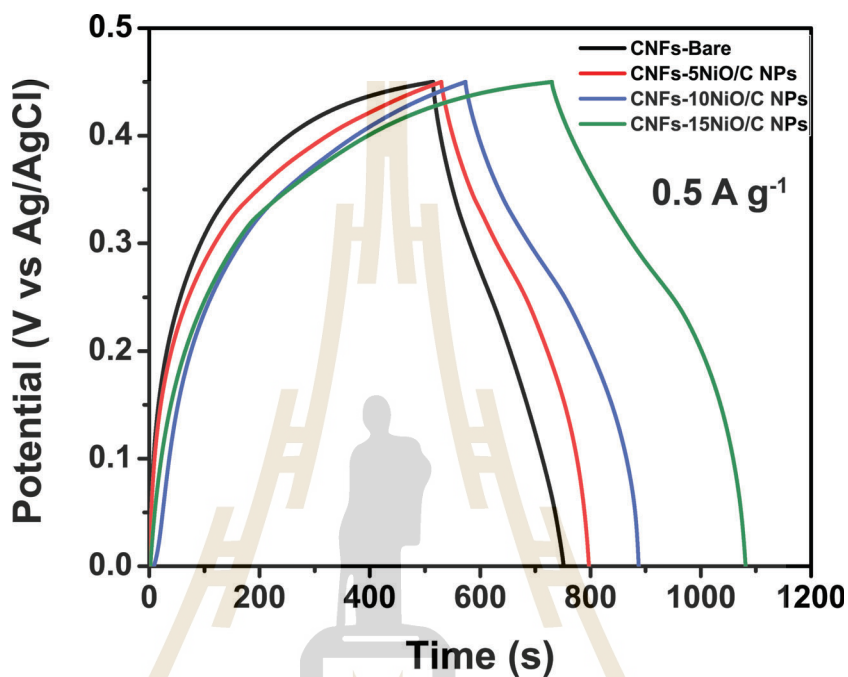


Figure 4.18 CV curves of CNFs-Bare, CNFs-5NiO/C NPs, CNFs-10NiO/C NPs, and CNFs-15NiO/C NPs electrode at a current density of 0.5 A g^{-1} .

The specific capacitance values were determined based on the area under the GCD discharge curves. Figure 4.19 presents a comparative analysis of the specific capacitance for CNFs-Bare, CNFs-5NiO/C NPs, CNFs-10NiO/C NPs, and CNFs-15NiO/C NPs electrodes at various current densities ranging from 0.5 to 5 A g^{-1} . The CNFs-Bare electrode exhibits specific capacitance values of 266 , 195 , 167 , 156 , 146 , and 139 F g^{-1} ; CNFs-5NiO/C NPs shows specific capacitance values of 343 , 286 , 246 , 230 , 218 , and 208 F g^{-1} ; CNFs-10NiO/C NPs achieves specific capacitance values of 404 , 327 , 274 , 254 , 242 , and 233 F g^{-1} ; and CNFs-15NiO/C NPs shows specific capacitance values of 474 , 467 , 428 , 400 , 392 , and 380 F g^{-1} , at the current densities of 0.5 – 5 A g^{-1} , respectively, as summarized in Table 4.3. The specific capacitance of the electrode typically decreases with increasing current density due to the insufficient time available for ions in an electrolyte to diffuse into the bulk of the active material and access all existing active sites within the material matrix (Rani et al., 2020).

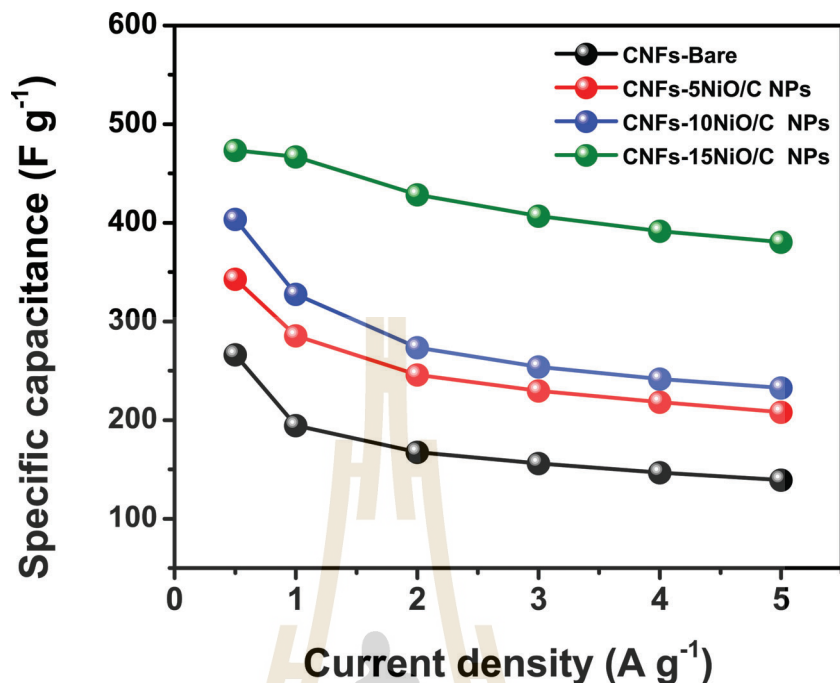


Figure 4.19 Specific capacitance of CNFs-Bare, CNFs-5NiO/C NPs, CNFs-10NiO/C NPs, and CNFs-15NiO/C NPs electrode at various current densities of 0.5–5 A g⁻¹.

Table 4.3 the specific capacitance value of CNFs-Bare, CNFs-5NiO/C NPs, CNFs-15NiO/C NPs, and CNFs-15NiO/C NPs electrode at various current densities of 0.5–5 A g⁻¹.

Current density (A g ⁻¹)	SC (F g ⁻¹)			
	CNFs-Bare	CNFs-5NiO/C NPs	CNFs-10NiO/C NPs	CNFs-15NiO/C NPs
0.5	266	343	404	474
1	195	286	327	467
2	167	246	274	428
3	156	230	254	400
4	146	218	242	392
5	139	208	233	380

The CNFs-NiO/C NPs electrode exhibits the higher specific capacitance value than CNFs-Bare at all current densities. This observation highlights the significant enhancement in electrochemical performance achieved through the incorporation of NiO/C NPs. The superior specific capacitance may be primarily attributed to the improved electrical conductivity, as well as the increased porosity and surface area of the active materials, which together promote efficient ion adsorption, enhanced electrolyte infiltration, and rapid ion transport within the electrode matrix (Daubert et al., 2015).

The conductive behavior and charge transport information of the CNFs electrodes are further confirmed by the results of the electrochemical impedance spectroscopy (EIS) analysis, as shown in the Nyquist plot in Figure 4.20a. Electrochemical impedance measurements conducted over a frequency range of 100 kHz to 0.01 Hz. The Nyquist impedance plot describes the relationship between the imaginary ($-Z''$) and real part (Z') of the impedance. The intercept on the real axis in the high-frequency region of the Nyquist plot corresponds to the equivalent series resistance (ESR), or bulk resistance (R_s) of the electrode and electrolyte (Yu et al., 2013). Impedance test at a frequency range of 100 kHz to 0.01 Hz show The R_s values of CNFs-Bare, CNFs-5NiO/C NPs, CNFs-10NiO/C NPs, and CNFs-15NiO/C NPs electrode is 1.15, 0.81, 0.71, and 0.59 Ω , respectively. This trend indicates that increasing the NiO/C NPs content embedded within the CNFs matrix leads to a reduction in R_s . This resistance consist of (i) ionic and electronic resistances, (ii) the intrinsic resistance of the NiO active material, and (iii) diffusive and contact resistance at the interface between the electrode and current collector (M. S. Wu and Hsieh, 2008). Therefore, the smaller R_s value reflects decreased electrical resistance, indicating that the incorporation of the NiO/C NPs embedded in the CNFs matrix effectively improves electrical conductivity and contributes to enhanced electrochemical performance (Moradlou et al., 2018). Additionally, the diameter of the semicircular arc in the mid-frequency region corresponds to the charge transfer resistance (R_{ct}), which relates to the resistance associated with electron transfer processes occurring at the interface of the electrode and electrolyte (Muthurasu and Ganesh, 2012). The absence of a semicircle in the Nyquist plots of CNFs-5NiO/C NPs, CNFs-10NiO/C NPs, and CNFs-15NiO/C NPs electrode suggests low charge transfer resistance (R_{ct}) at the electrode–electrolyte interface, indicating highly efficient charge transport (W. Chen et al., 2014), as shown in Figure 4.20b. In contrast, the CNFs-Bare electrode exhibits a noticeable semicircle with an R_{ct} value of 1.17 Ω , reflecting a relatively reduced charge storage capability (Elkholy et al., 2017). These enhancement can be attributed to the dual electrochemical characteristics of the NiO/C NPs, which consist both NiO and metallic Ni components. NiO contributes significantly to electrochemical performance due to its excellent charge storage capabilities. Concurrently, the presence of conductive metallic Ni facilitates rapid electron transport pathways, enabling faster Faradaic reactions. Consequently, the combined presence of NiO and Ni within the NiO/C NPs significantly enhances the overall electrochemical behavior and increases the specific capacitance of the CNFs decorated with these nanostructures (M.

Liu et al., 2013). Accordingly, the CNFs-15NiO/C NPs electrode exhibits the highest specific capacitance, which is primarily attributed to the highest loading of NiO/C NPs in the polymer precursor. This increased concentration leads to enhanced porosity and electrical conductivity of the CNFs matrix. These enhancements facilitate greater electrolyte diffusion within the electrode structure, thereby reducing charge-transfer resistance and significantly improving the overall electrochemical performance.

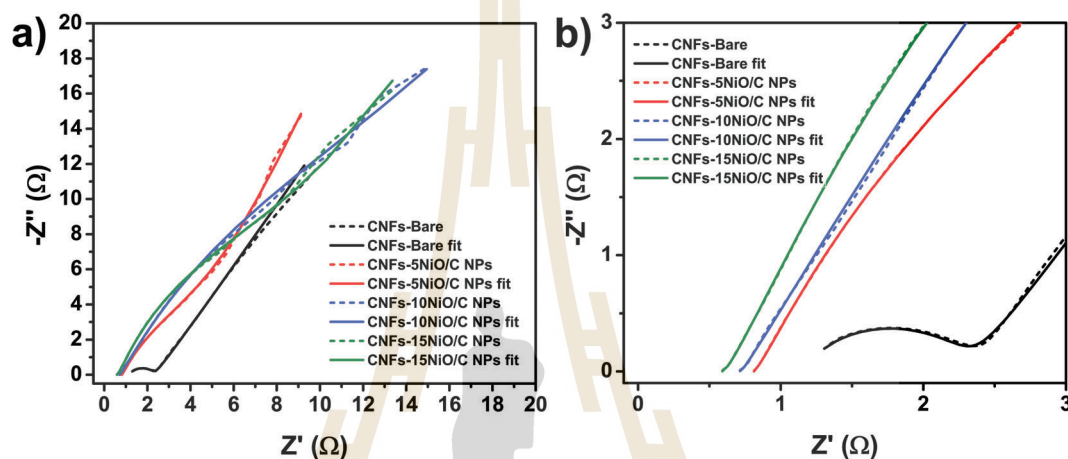


Figure 4.20 Nyquist plot of (a) CNFs-Bare, CNFs-5NiO/C NPs, CNFs-10NiO/C NPs, and CNFs-15NiO/C NPs electrode with (b) their high to low frequency region, where the solid lines represent the fitted data and the dashed lines correspond to the raw experimental data.

Long-term cyclic stability of the electrode is a crucial demand for evaluating the practical applicability of supercapacitor devices. The cycling performance of all electrodes was assessed through continuous charge–discharge testing at a current density of 3 A g^{-1} over 1000 cycles, as shown in Figure 4.21. After 1000 charge–discharge cycles, the capacitance percentage retention of CNFs-Bare, CNFs-5NiO/C NPs, CNFs-10NiO/C NPs, and CNFs-15NiO/C NPs remained approximately 81, 92, 91, and 103% of their initial values, respectively. These results demonstrate that all CNFs-based electrodes maintained more than 80% of their initial capacitance after 1000 charge–discharge cycles, while the CNFs electrodes embedded with NiO/C nanoparticles exhibited enhanced stability, retaining over 90%. Notably, the CNFs-15NiO/C NPs electrode exhibited a capacitance retention exceeding 103%, indicating that electrochemical activation was not fully achieved during the initial cycles (Tanapongpisit et al., 2022).

Based on these electrochemical results, the CNFs-15NiO/C NPs electrode demonstrates the highest specific capacitance performance. This elevated concentra-

tion of NiO/C NPs in the precursor solution can enhance both the porosity and electrochemical performance characteristics of the CNFs electrode. These results demonstrate that the integration of NiO/C NPs with CNFs can substantially enhance the electrochemical performance characteristics of supercapacitor electrode systems.

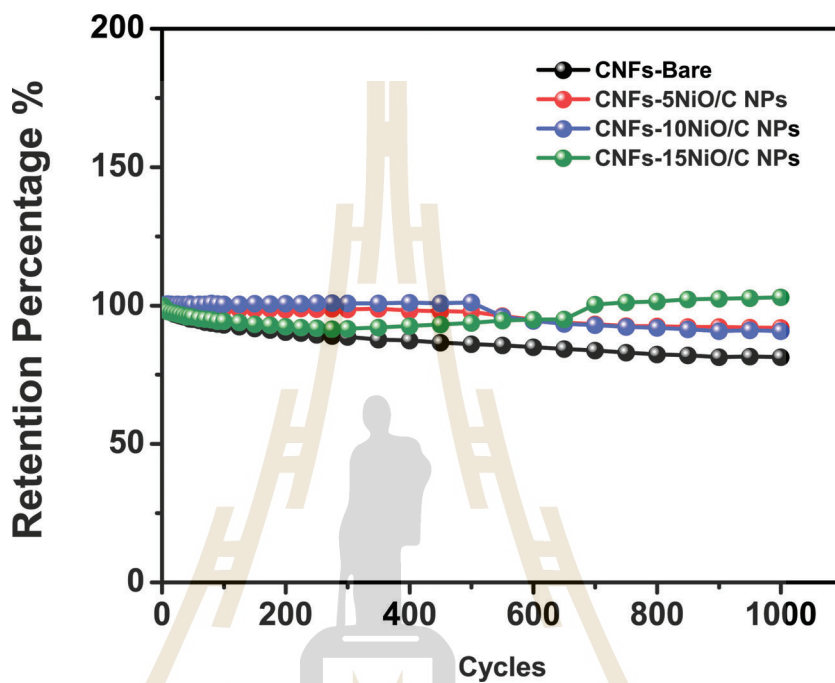


Figure 4.21 Cyclic stability for 1000 cycles of all electrodes at a current density of 3 A g^{-1} .

CHAPTER V

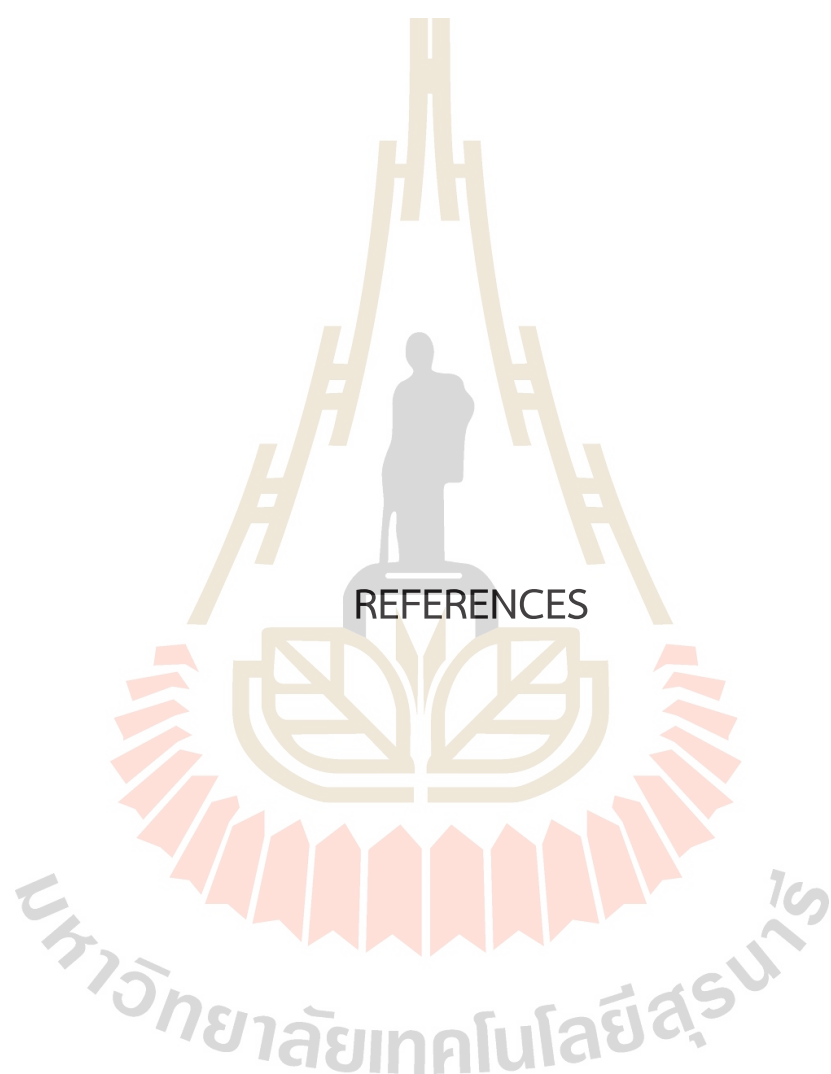
CONCLUSION AND RECOMMENDATION

In this study, CNFs decorated with NiO/C NPs were successfully synthesized through an electrospinning process followed by thermal treatment. The synthesis approach demonstrated high controllability, enabling the preparation of nanostructured electrodes with well-integrated NiO/C NPs. Structural, morphological, and compositional analyses confirmed the successful incorporation of NiO/C NPs within the CNFs matrix, which enhanced both porosity and surface area. Moreover, electrochemical analysis demonstrated a marked enhancement in the specific capacitance of CNFs upon the incorporation of NiO/C NPs. Notably, the CNFs-15NiO/C NPs electrode, comprising 15 wt% NiO/C NPs, exhibited the highest specific capacitance value of 474 F g^{-1} at a current density of 0.5 A g^{-1} , significantly increasing that of the CNFs-Bare electrode, which recorded a capacitance of 266 F g^{-1} under identical conditions. This enhancement is primarily attributed to the synergistic contribution of electric double-layer capacitance originating from the CNFs and the pseudocapacitive behavior of the NiO phase, combined with the high electrical conductivity imparted by metallic Ni. The increased loading of NiO/C NPs also contributed to a reduction in internal resistance and enhanced charge transport, as confirmed by EIS measurements. The electrodes also demonstrated excellent cycling stability after 1000 cycles. Notably, the CNFs-15NiO/C NPs electrode demonstrated outstanding cycling stability, maintaining 103 % of its initial capacitance after 1000 cycles, suggesting possible electrochemical activation during extended cycling. These results collectively underscore the potential of CNFs-NiO/C nanocomposites as high-performance electrode materials for next-generation supercapacitors, offering a promising pathway toward the development of energy storage devices with enhanced energy density, conductivity, and cycling durability.

Future investigations should consider exploring NiO loadings more than 15 %wt to determine the optimal balance between enhanced capacitance and structural stability. Moreover, fine-tuning parameters such as crystallinity, particle size, and the Ni/NiO phase ratio may lead to further improvements in electrical conductivity and redox activity. Collectively, the findings of this study offer significant insights into the rational design of hybrid nanostructured electrodes and establish a promising foundation for

the scalable development of high-performance energy storage systems.





REFERENCES

- Abouali, S., Garakani, M. A., Zhang, B., Xu, Z.-L., Heidari, E. K., Huang, J.-q., Huang, J., and Kim, J.-K. (2015). Electrospun carbon nanofibers with in situ encapsulated CO_3O_4 nanoparticles as electrodes for high-performance supercapacitors. *ACS applied materials and interfaces*, 7, 13503–13511.
- Agrawal, S. (2022). Spectroscopy techniques for rare-earth-activated phosphors. In *Rare-earth-activated phosphors* (pp. 147–175). Elsevier.
- Ahankari, S., and Kar, K. (2017). *Functionally graded composites: Processing and applications*. Springer.
- Ahmad, A., Ahmad, I., Ramzan, S., Kiyani, M. Z., Dubal, D., and Mubarak, N. (2021). 5 - nanomaterial synthesis protocols. In F. Verpoort, I. Ahmad, A. Ahmad, A. Khan and C. Y. Chee (Eds.), *Nanomedicine manufacturing and applications* (pp. 73–85). Elsevier.
- Asmatulu, R., and Khan, W. (2019). Introduction to electrospun nanofibers.
- Balu, A., Nagarethinam, V., Arunkumar, N., and Suganya, M. (2012). Nanocrystalline nio thin films prepared by a low cost simplified spray technique using perfume atomizer. *Journal of electron devices*, 13, 920–930.
- Barakat, N., Khalil, A., and Kim, H. (2012). Toward facile synthesizing of diamond nanostructures via nanotechnological approach: Lonsdaleite carbon nanofibers by electrospinning. *Materials Research Bulletin*, 47, 2140–2147.
- Bashir, Z. (1991). A critical review of the stabilisation of polyacrylonitrile. *Carbon*, 29(8), 1081–1090.
- Beguin, F., Presser, V., Balducci, A., and Frackowiak, E. (2014). Carbons and electrolytes for advanced supercapacitors. *Advanced materials (Deerfield Beach, Fla.)*, 26, 2219–2251.
- Benko, A., Fraczek-Szczypta, A., Menaszek, E., Wyrwa, J., Nocun, M., and Blazewicz, M. (2015). On the influence of various physicochemical properties of the cnts based implantable devices on the fibroblasts' reaction in vitro. *Journal of Materials Science: Materials in Medicine*, 26, 1–13.
- Biesinger, M. C., Payne, B. P., Lau, L. W., Gerson, A., and Smart, R. S. C. (2009). X-ray photoelectron spectroscopic chemical state quantification of mixed nickel metal,

- oxide and hydroxide systems. *Surface and Interface Analysis: An International Journal devoted to the development and application of techniques for the analysis of surfaces, interfaces and thin films*, 41(4), 324–332.
- Boesenberg, U., Marcus, M. A., Shukla, A. K., Yi, T., McDermott, E., Teh, P. F., Srinivasan, M., Moewes, A., and Cabana, J. (2014). Asymmetric pathways in the electrochemical conversion reaction of nio as battery electrode with high storage capacity. *Scientific reports*, 4(1), 7133.
- Bruker Corporation. (n.d.). What is ft-ir spectroscopy? [Accessed: 2025-06-11].
- Candelaria, S. L., Garcia, B. B., Liu, D., and Cao, G. (2012). Nitrogen modification of highly porous carbon for improved supercapacitor performance. *Journal of Materials Chemistry*, 22(19), 9884–9889.
- Cervo, E., and Thies, M. (2007). Control of the molecular weight distribution of petroleum pitches via dense-gas extraction. *Chemical Engineering Technology*, 30, 742–748.
- Chen, J., and Harrison, I. (2002). Modification of polyacrylonitrile (pan) carbon fiber precursor via post-spinning plasticization and stretching in dimethyl formamide (dmf). *Carbon*, 40(1), 25–45.
- Chen, J., Li, W., Wang, D., Yang, S., Wen, J., and Ren, Z. (2002). Electrochemical characterization of carbon nanotubes as electrode in electrochemical double-layer capacitors. *Carbon*, 40(8), 1193–1197.
- Chen, W., Xia, C., and Alshareef, H. N. (2014). One-step electrodeposited nickel cobalt sulfide nanosheet arrays for high-performance asymmetric supercapacitors. *ACS nano*, 8(9), 9531–9541.
- Cheng, Y., Huang, L., Xiao, X., Yao, B., Yuan, L., Li, T., Hu, Z., Wang, B., Wan, J., and Zhou, J. (2015). Flexible and cross-linked n-doped carbon nanofiber network for high performance freestanding supercapacitor electrode. *Nano energy*, 15, 66–74.
- Cong, R., Choi, J.-Y., Song, J.-B., Jo, M., Lee, H., and Lee, C.-S. (2021). Characteristics and electrochemical performances of silicon/carbon nanofiber/graphene composite films as anode materials for binder-free lithium-ion batteries. *Scientific reports*, 11(1), 1283.
- Daubert, J. S., Lewis, N. P., Gotsch, H. N., Mundy, J. Z., Monroe, D. N., Dickey, E. C., Losego, M. D., and Parsons, G. N. (2015). Effect of meso- and micro-porosity in carbon electrodes on atomic layer deposition of pseudocapacitive V_2O_5 for high performance supercapacitors. *Chemistry of Materials*, 27(19), 6524–6534.

- Denny, Y. R., Takahashi, K., Niki, K., Yang, D. S., Fujikawa, T., and Kang, H. J. (2014). Ni k-edge xafs analysis of nio thin film with multiple scattering theory. *Surface and Interface Analysis*, 46(10-11), 997–999.
- Dilmukhambetov, E., Espolov, T., Ospanova, M., and Ilyin, A. (2013). Reactivity to oxidation of metal nanopowders after electron irradiation. *Journal of Materials Science Research*, 2(1), 175.
- Elkholy, A. E., Heakal, F. E. T., and Allam, N. K. (2017). Nanostructured spinel manganese cobalt ferrite for high-performance supercapacitors. *RSC advances*, 7(82), 51888–51895.
- Endo, M., Kim, Y., Hayashi, T., Nishimura, K., Matusita, T., Miyashita, K., and Dresselhaus, M. (2001). Vapor-grown carbon fibers (vgcfs): Basic properties and their battery applications. *Carbon*, 39(9), 1287–1297.
- Fan, L.-Z., and Maier, J. (2006). High-performance polypyrrole electrode materials for redox supercapacitors. *Electrochemistry communications*, 8(6), 937–940.
- Fang, B., and Binder, L. (2006). A modified activated carbon aerogel for high-energy storage in electric double layer capacitors. *Journal of power sources*, 163(1), 616–622.
- Fayed, M. G., Aman, D., and Mohamed, S. G. (2025). Synergetic electrochemical behavior of nio and activated carbon composites for advanced supercapacitors. *Journal of Cluster Science*, 36(3), 94.
- Fic, K., Platek, A., Piwek, J., and Frackowiak, E. (2018). Sustainable materials for electrochemical capacitors. *Materials Today*, 21, 437–454.
- Flöck, J., Friedrich, K., and Yuan, Q. (1999). On the friction and wear behaviour of pan-and pitch-carbon fiber reinforced peek composites. *Wear*, 225, 304–311.
- Fracchia, M., Ghigna, P., Vertova, A., Rondinini, S., and Minguzzi, A. (2018). Time-resolved x-ray absorption spectroscopy in (photo) electrochemistry. *Surfaces*, 1(1), 138–150.
- Ghouri, Z., Barakat, N., Obaid, M., Lee, J., and Kim, H. (2015). Co/CeO₂-decorated carbon nanofibers as effective non-precious electro-catalyst for fuel cells application in alkaline medium. *Ceramics International*, 41, 2271–2278.
- Goswami, M., Kumar, S., Siddiqui, H., Chauhan, V., Singh, N., Sathish, N., Ashiq, M., and Kumar, S. (2023). Hybrid energy storage devices: Li-ion and na-ion capacitors. In *Emerging trends in energy storage systems and industrial applications* (pp. 223–258). Elsevier.

- Greczynski, G., and Hultman, L. (2020). X-ray photoelectron spectroscopy: Towards reliable binding energy referencing. *Progress in Materials Science*, 107, 100591.
- Gu, Y., Ding, J., Hu, G., You, F., Chen, S., Huang, H., and Hu, C. (2024). Carbon nanofibers as supporting substrate for growth of polyaniline nanorods on fe₂o₃ nanoneedles toward electrochemical energy storage. *ACS omega*, 9(51), 50237–50245.
- Guo, M., Guo, J., Jia, D., Zhao, H., Sun, Z., Song, X., and Li, Y. (2015). Coal derived porous carbon fibers with tunable internal channels for flexible electrodes and organic matter absorption. *J. Mater. Chem. A*, 3, 21178–21184.
- Hammel, E., Tang, X., Trampert, M., Schmitt, T., Mauthner, K., Eder, A., and Pötschke, P. (2004). Carbon nanofibers for composite applications. *Carbon*, 42(5), 1153–1158.
- Han, B., Yu, X., and Ou, J. (2014). Chapter 2 - compositions of self-sensing concrete. In B. Han, X. Yu and J. Ou (Eds.), *Self-sensing concrete in smart structures* (pp. 13–43). Butterworth-Heinemann.
- Hu, J., Wang, H., and Huang, X. (2012). Improved electrochemical performance of hierarchical porous carbon/polyaniline composites. *Electrochimica Acta*, 74, 98–104.
- Huang, Y., Yang, J., Cai, H., Zhai, Y., Feng, D., Deng, Y., Tu, B., and Zhao, D. (2009). A curing agent method to synthesize ordered mesoporous carbons from linear novolac phenolic resin polymers. *J. Mater. Chem.*, 19, 6536–6541.
- Inagaki, M., Yang, Y., and Kang, F. (2012). Carbon nanofibers prepared via electrospinning. *Advanced materials (Deerfield Beach, Fla.)*, 24(19), 2547–2566.
- Jaya, R. P. (2020). Porous concrete pavement containing nanosilica from black rice husk ash. In *New materials in civil engineering* (pp. 493–527). Elsevier.
- Jiang, H., Sun, T., Li, C., and Ma, J. (2011). Peapod-like nickel@ mesoporous carbon core-shell nanowires: A novel electrode material for supercapacitors. *RSC advances*, 1(6), 954–957.
- Jiang, L., Ren, Z., Chen, S., Zhang, Q., Lu, X., Zhang, H., and Wan, G. (2018). Bio-derived three-dimensional hierarchical carbon-graphene-TiO₂ as electrode for supercapacitors. *Scientific reports*, 8(1), 4412.
- Jiang, P., Wang, Q., Dai, J., Li, W., and Wei, Z. (2017). Fabrication of nio@ co₃o₄ core/shell nanofibres for high-performance supercapacitors. *Materials Letters*, 188, 69–72.
- Jiang, X., Deng, S., Liu, J., Qi, N., and Chen, Z. (2021). Metal–organic framework derived nio/ni@ c composites as electrode materials with excellent electrochemical performance for supercapacitors. *Journal of Energy Storage*, 37, 102426.

- Kang, E., Jeon, G., and Kim, J. K. (2013). Free-standing, well-aligned ordered mesoporous carbon nanofibers on current collectors for high-power micro-supercapacitors. *Chem. Commun.*, 49, 6406–6408.
- Kar, K. K. (2020a). *Handbook of nanocomposite supercapacitor materials i*. Springer.
- Kar, K. K. (2020b). *Handbook of nanocomposite supercapacitor materials ii* (Vol. 302). Springer.
- Kar, K. K., Rana, S., and Pandey, J. (2015). *Handbook of polymer nanocomposites processing, performance and application*. Springer.
- Karacan, I., and Meşeli, H. (2016). Characterization of amorphous carbon fibers produced from thermally stabilized polyamide 6 fibers. *Journal of Industrial Textiles*, 47, 1–27.
- Karuppanan, K. K., Panthalingal, M. K., and Biji, P. (2018). Chapter 26 - nanoscale, catalyst support materials for proton-exchange membrane fuel cells. In C. Mustansar Hussain (Ed.), *Handbook of nanomaterials for industrial applications* (pp. 468–495). Elsevier.
- Khan, S. A., Khan, S. B., Khan, L. U., Farooq, A., Akhtar, K., and Asiri, A. M. (2018). Fourier transform infrared spectroscopy: Fundamentals and application in functional groups and nanomaterials characterization. *Handbook of materials characterization*, 317–344.
- Kim, C. H., and Kim, B.-H. (2015). Zinc oxide/activated carbon nanofiber composites for high-performance supercapacitor electrodes. *Journal of Power Sources*, 274, 512–520.
- Kim, K., and Winograd, N. (1974). X-ray photoelectron spectroscopic studies of nickel-oxygen surfaces using oxygen and argon ion-bombardment. *Surface Science*, 43(2), 625–643.
- Kim, S. K., Kim, S. A., Han, Y. S., and Jung, K.-H. (2024). Supercapacitor performance of mxene-coated carbon nanofiber electrodes. *C*, 10(2), 32.
- Konstantopoulos, G., Soulis, S., Dragatogiannis, D., and Charitidis, C. (2020). Introduction of a methodology to enhance the stabilization process of pan fibers by modeling and advanced characterization. *Materials*, 13(12), 2749.
- Kötz, R., and Carlen, M. (2000). Principles and applications of electrochemical capacitors. *Electrochimica acta*, 45(15-16), 2483–2498.

- Lee, B.-S., and Yu, W.-R. (2020). Electrospun carbon nanofibers as a functional composite platform: A review of highly tunable microstructures and morphologies for versatile applications. *Functional Composites and Structures*, 2(1), 012001.
- Lee, C., Kim, S. K., Chang, H., and Jang, H. D. (2019). Active electrode materials of graphene balls and their composites for supercapacitors: A perspective view. *Advanced Powder Technology*, 30(12), 3079–3087.
- Lee, H.-F., Wang, P.-C., and Chen-Yang, Y. W. (2019). An electrospun hygroscopic and electron-conductive core-shell silica-carbon nanofiber for microporous layer in proton-exchange membrane fuel cell. *Journal of Solid State Electrochemistry*, 23(3), 971–984.
- Lee, J. Y., Kim, N. Y., Shin, D. Y., Park, H.-Y., Lee, S.-S., Joon Kwon, S., Lim, D.-H., Bong, K. W., Son, J. G., and Kim, J. Y. (2017). Nitrogen-doped graphene-wrapped iron nanofragments for high-performance oxygen reduction electrocatalysts. *Journal of Nanoparticle Research*, 19(3), 98.
- Lee, J. H., Jung, H. W., Kim, I. S., Park, M., and Kim, H.-S. (2021). Electrochemical evaluation of surface modified free-standing cnt electrode for li-o₂ battery cathode. *Energies*, 14(14), 4196.
- Lewis, I. R., and Edwards, H. (2001). *Handbook of raman spectroscopy: From the research laboratory to the process line*. CRC press.
- Li, H.-F., Wang, C., Liu, L.-F., Xie, N., Pan, M., Wu, P., Wang, X.-D., Zeng, Z., Deng, S., and Dai, G.-P. (2020). Facile one-step synthesis of n-doped carbon nanotubes/n-doped carbon nanofibers hierarchical composites by chemical vapor deposition. *Journal of Nanoparticle Research*, 22, 1–10.
- Li, J., Zhao, W., Huang, F., Manivannan, A., and Wu, N. (2011). Single-crystalline ni(oH)₂ and nio nanoplatelet arrays as supercapacitor electrodes. *Nanoscale*, 3(12), 5103–5109.
- Li, K., Zhang, X., Qin, Y., and Li, Y. (2021). Construction of the cellulose nanofibers (cnfs) aerogel loading TiO₂ nps and its application in disposal of organic pollutants. *Polym.*, 13(11), 1841.
- Li, W., Liu, J., and Zhao, D. (2016). Mesoporous materials for energy conversion and storage devices. *Nature Reviews Materials*, 1(6), 1–17.
- Liang, H.-W., Guan, Q.-F., Chen, L.-F., Zhu, Z., Zhang, W.-J., and Yu, S.-H. (2012). Macroscopic-scale template synthesis of robust carbonaceous nanofiber hydro-

- gels and aerogels and their applications. *Angew. Chem., Int. Ed. Engl.*, 51(21), 5101–5105.
- Lichao, F., Ning, X., and Jing, Z. (2014). Carbon nanofibers and their composites: A review of synthesizing, properties and applications. *Materials*, 7(5), 3919–3945.
- Liu, C.-L., Dong, W.-S., Cao, G.-P., Song, J.-R., Liu, L., and Yang, Y.-S. (2007). Influence of koh followed by oxidation pretreatment on the electrochemical performance of phenolic based activated carbon fibers. *Journal of Electroanalytical Chemistry*, 611(1-2), 225–231.
- Liu, M., Qin, Z., Yang, X., Lin, Z., and Guo, T. (2019). Fabricating controllable hierarchical pores on smooth carbon sheet for synthesis of supercapacitor materials. *Vacuum*, 168, 108806.
- Liu, M., Chang, J., Sun, J., and Gao, L. (2013). A facile preparation of nio/ni composites as high-performance pseudocapacitor materials. *RSC advances*, 3(21), 8003–8008.
- Liu, X.-M., Zhang, X.-G., and Fu, S.-Y. (2006). Preparation of urchinlike nio nanostructures and their electrochemical capacitive behaviors. *Materials Research Bulletin*, 41(3), 620–627.
- Liu, X., Sun, J., Liu, Y., Liu, D., Chen, H., Zhuo, K., and Xu, C. (2022). Electrospun nio/c nanofibers as electrode materials for hybrid supercapacitors with superior electrochemical performance. *International Journal of Hydrogen Energy*, 47(38), 16985–16995.
- Lu, J., Zhang, J., Wang, X., Zhang, J., Tian, Z., Zhu, E., Yang, L., Guan, X., Ren, H., Wu, J., et al. (2024). A review of advanced electrolytes for supercapacitors. *Journal of Energy Storage*, 103, 114338.
- Lu, X., Li, M., Wang, H., and Wang, C. (2019). Advanced electrospun nanomaterials for highly efficient electrocatalysis. *Inorg. Chem. Front.*, 6, 3012–3040.
- Lu, X., Wang, C., Favier, F., and Pinna, N. (2017). Electrospun nanomaterials for supercapacitor electrodes: Designed architectures and electrochemical performance. *Adv. Energy Mater.*, 7(2), 1601301.
- Lu, Z., Chang, Z., Zhu, W., and Sun, X. (2011). Beta-phased ni (oh) 2 nanowall film with reversible capacitance higher than theoretical faradic capacitance. *Chemical Communications*, 47(34), 9651–9653.
- Lv, S., Shang, W., Wang, H., Chu, X., Chi, Y., Wang, C., Yang, J., Geng, P., and Yang, X. (2022). Design and construction of cu (oh) 2/ni3s2 composite electrode on cu foam by two-step electrodeposition. *Micromachines*, 13(2), 237.

- Ma, X., Liu, M., Gan, L., Zhao, Y., and Chen, L. (2013). Synthesis of micro-and mesoporous carbon spheres for supercapacitor electrode. *Journal of Solid State Electrochemistry*, 17, 2293–2301.
- McClure, J. P., Thornton, J. D., Jiang, R., Chu, D., Cuomo, J. J., and Fedkiw, P. S. (2012). Oxygen reduction on metal-free nitrogen-doped carbon nanowall electrodes. *Journal of the Electrochemical Society*, 159(11), F733.
- Meher, S. K., Justin, P., and Rao, G. R. (2011). Nanoscale morphology dependent pseudocapacitance of nio: Influence of intercalating anions during synthesis. *Nanoscale*, 3(2), 683–692.
- Melles, D. C., van Leeuwen, W. B., Snijders, S. V., Horst-Kreft, D., Peeters, J. K., Verbrugh, H. A., and van Belkum, A. (2007). Comparison of multilocus sequence typing (mlst), pulsed-field gel electrophoresis (pfge), and amplified fragment length polymorphism (aflp) for genetic typing of staphylococcus aureus. *Journal of Microbiological Methods*, 69(2), 371–375.
- Mevada, C., and Mukhopadhyay, M. (2023). Introduction to supercapacitors. In K. K. Kar (Ed.), *Handbook of nanocomposite supercapacitor materials iv: Next-generation supercapacitors* (pp. 1–17). Springer International Publishing.
- Miao, Y.-E., and Liu, T. (2019). Electrospun nanofiber electrodes: A promising platform for supercapacitor applications. In *Electrospinning: Nanofabrication and applications* (pp. 641–669). Elsevier.
- Mironova-Ulmane, N., Kuzmin, A., Steins, I., Grabis, J., Sildos, I., and Pārs, M. (2007). Raman scattering in nanosized nickel oxide nio. *Journal of Physics: Conference Series*, 93(1), 012039.
- Mitsutake, H., Poppi, R. J., and Breitreitz, M. C. (2019). Raman imaging spectroscopy: History, fundamentals and current scenario of the technique. *Journal of the Brazilian Chemical Society*, 30(11), 2243–2258.
- Mohd Abdah, M. A. A., Azman, N. H. N., Kulandaivalu, S., and Sulaiman, Y. (2019). Asymmetric supercapacitor of functionalised electrospun carbon fibers/poly (3, 4-ethylenedioxythiophene)/manganese oxide//activated carbon with superior electrochemical performance. *Scientific Reports*, 9(1), 16782.
- Moradlou, O., Ansarinejad, H., Hosseinzadeh, M., and Kazemi, H. (2018). High-performance solid state asymmetric supercapacitor based on electrochemically decorated 3d network-like co₃o₄ architecture on nio nanoworms. *Journal of Alloys and Compounds*, 755, 231–241.

- Mori, C., Passos, N., Oliveira, J., Altoé, T., Mori, F., Scolforo, J., Mattoso, L., and Tonoli, G. (2015). Nanostructured polylactic acid/candeia essential oil mats obtained by electrospinning. *Journal of Nanomaterials*, 2015.
- Motlak, M., Barakat, N. A., Akhtar, M. S., Hamza, A., Kim, B.-S., Kim, C. S., Khalil, K. A., and Almajid, A. A. (2015). High performance of nico nanoparticles-doped carbon nanofibers as counter electrode for dye-sensitized solar cells. *Electrochimica Acta*, 160, 1–6.
- Muduli, S., Pati, S. K., Pani, T. K., and Martha, S. K. (2023). One pot synthesis of carbon decorated nio nanorods as cathode materials for high-performance asymmetric supercapacitors. *Journal of Energy Storage*, 66, 107339.
- Muthurasu, A., and Ganesh, V. (2012). Electrochemical characterization of self-assembled monolayers (sams) of silanes on indium tin oxide (ito) electrodes—tuning electron transfer behaviour across electrode–electrolyte interface. *Journal of colloid and interface science*, 374(1), 241–249.
- Muzaffar, A., Ahamed, M. B., Deshmukh, K., and Thirumalai, J. (2019). A review on recent advances in hybrid supercapacitors: Design, fabrication and applications. *Renewable and sustainable energy reviews*, 101, 123–145.
- Nasrollahzadeh, M., Atarod, M., Sajjadi, M., Sajadi, S. M., and Issaabadi, Z. (2019). Plant-mediated green synthesis of nanostructures: Mechanisms, characterization, and applications. In *Interface science and technology* (pp. 199–322, Vol. 28). Elsevier.
- Neikov, O. D., and Yefimov, N. A. (2019). Chapter 1 - powder characterization and testing. In O. D. Neikov, S. S. Naboychenko and N. A. Yefimov (Eds.), *Handbook of non-ferrous metal powders (second edition)* (Second Edition, pp. 3–62). Elsevier.
- Nguyen, T. M. H., and Bark, C. W. (2020). Highly porous nanostructured nio@c as interface-effective layer in planar nip perovskite solar cells. *Journal of Alloys and Compounds*, 841, 155711.
- Novais, Â., Freitas, A. R., Rodrigues, C., and Peixe, L. (2019). Fourier transform infrared spectroscopy: Unlocking fundamentals and prospects for bacterial strain typing. *European Journal of Clinical Microbiology & Infectious Diseases*, 38, 427–448.
- Padmavathi, R., and Sangeetha, D. (2013). Synthesis and characterization of electrospun carbon nanofiber supported pt catalyst for fuel cells. *Electrochimica Acta*, 112, 1–13.
- Particle Technology Labs. (n.d.). Bet specific surface area analysis [Accessed: 2025-06-05].

- Patil, U., Salunkhe, R., Gurav, K., and Lokhande, C. (2008). Chemically deposited nanocrystalline nio thin films for supercapacitor application. *Applied Surface Science*, 255(5, Part 2), 2603–2607.
- Permatasari, F. A., Irham, M. A., Bisri, S. Z., and Iskandar, F. (2021). Carbon-based quantum dots for supercapacitors: Recent advances and future challenges. *Nanomaterials*, 11(1), 91.
- Pham, P. V. (2022, April). *21st century nanostructured materials*. IntechOpen.
- Prabhu, R., Jayarambabu, N., Anitha, N., Jitesh, P., Hitesh, B., and Rao, T. V. (2024). Size dependent electrochemical properties of green synthesized nio nanoparticles as a supercapacitor electrode. *Inorganic Chemistry Communications*, 160, 111836.
- Prasad, K. R., Koga, K., and Miura, N. (2004). Electrochemical deposition of nanostructured indium oxide: High-performance electrode material for redox supercapacitors. *Chemistry of materials*, 16(10), 1845–1847.
- Rahaman, M. S. A., Ismail, A. F., and Mustafa, A. (2007). A review of heat treatment on polyacrylonitrile fiber. *Polymer degradation and Stability*, 92(8), 1421–1432.
- Rakhimbek, I., Baikalov, N., Konarov, A., Mentbayeva, A., Zhang, Y., and Bakenov, Z. (2024). Nickel and nickel oxide nanoparticle-embedded functional carbon nanofibers for lithium sulfur batteries. *Nanoscale Advances*, 6(2), 578–589.
- Rakshit, S., Ghosh, S., Chall, S., Mati, S. S., Moulik, S., and Bhattacharya, S. C. (2013). Controlled synthesis of spin glass nickel oxide nanoparticles and evaluation of their potential antimicrobial activity: A cost effective and eco friendly approach. *RSC Advances*, 3(42), 19348–19356.
- Rani, S., Kumar, N., Tandon, A., and Sharma, Y. (2020). Fabrication of binder-free TiO₂ nanofiber electrodes via electrophoretic deposition for low-power electronic applications. *IEEE Transactions on Electron Devices*, 68(1), 251–256.
- Reddy, N. R., Reddy, P. M., Mandal, T. K., Reddy, K. R., Shetti, N. P., Saleh, T. A., Joo, S. W., and Aminabhavi, T. M. (2021). Synthesis of novel co₃o₄ nanocubes-nio octahedral hybrids for electrochemical energy storage supercapacitors. *Journal of Environmental Management*, 298, 113484.
- Ren, Y., and Gao, L. (2010). From three-dimensional flower-like α -ni (oh) 2 nanostructures to hierarchical porous nio nanoflowers: Microwave-assisted fabrication and supercapacitor properties. *Journal of the American Ceramic Society*, 93(11), 3560–3564.

- Richardson, J. T., Scates, R., and Twigg, M. V. (2003). X-ray diffraction study of nickel oxide reduction by hydrogen. *Applied Catalysis A: General*, *246*(1), 137–150.
- Roldán, L., Armenise, S., Marco, Y., and García-Bordejé, E. (2012). Control of nitrogen insertion during the growth of nitrogen-containing carbon nanofibers on cordierite monolith walls. *Physical Chemistry Chemical Physics*, *14*(10), 3568–3575.
- Rong, X., Qiu, F., Qin, J., Zhao, H., Yan, J., and Yang, D. (2015). A facile hydrothermal synthesis, adsorption kinetics and isotherms to congo red azo-dye from aqueous solution of nio/graphene nanosheets adsorbent. *Journal of industrial and engineering chemistry*, *26*, 354–363.
- Ruiz, V., Blanco, C., Granda, M., Menéndez, R., and Santamaría, R. (2008). Effect of the thermal treatment of carbon-based electrodes on the electrochemical performance of supercapacitors. *Journal of Electroanalytical Chemistry*, *618*(1-2), 17–23.
- Sajjad, M., Tao, R., Kang, K., Luo, S., and Qiu, L. (2021). Phosphine-based porous organic polymer/rgo aerogel composites for high-performance asymmetric supercapacitor. *ACS Appl. Energy Mater.*, *4*(1), 828–838.
- Saleemi, A. S., Saeed, M., Hussan, M., Rehman, S. U., Hafeez, M., Mehmood, S., Sial, M. A. Z. G., and Lee, S.-l. (2019). Anomalous non-linear to linear shift in magnetoresistance of amorphous carbon films. *Crystals*, *9*(12), 618.
- Salunkhe, P., AV, M. A., and Kekuda, D. (2021). Structural, spectroscopic and electrical properties of dc magnetron sputtered nio thin films and an insight into different defect states. *Applied Physics A*, *127*(5), 390.
- Sankar, S., Lee, H., Jung, H., Kim, A., Ahmed, A. T. A., Inamdar, A. I., Kim, H., Lee, S., Im, H., and Kim, D. Y. (2017). Ultrathin graphene nanosheets derived from rice husks for sustainable supercapacitor electrodes. *New Journal of Chemistry*, *41*(22), 13792–13797.
- Saswata, B., Tapas, K., Ananta, M., R., R., Hoon, K. N., and Joong, L. (2012). Carbon-based nanostructured materials and their composites as supercapacitor electrodes. *Journal of Materials Chemistry*, *22*, 767.
- Seo, E., Lee, T., Lee, K. T., Song, H.-K., and Kim, B.-S. (2012). Versatile double hydrophilic block copolymer: Dual role as synthetic nanoreactor and ionic and electronic conduction layer for ruthenium oxide nanoparticle supercapacitors. *Journal of Materials Chemistry*, *22*(23), 11598–11604.

- Shao, Y., El-Kady, M. F., Sun, J., Li, Y., Zhang, Q., Zhu, M., Wang, H., Dunn, B., and Kaner, R. B. (2018). Design and mechanisms of asymmetric supercapacitors. *Chemical reviews*, 118(18), 9233–9280.
- Shiraishi, S., and Tanaike, O. (2015). Application of carbon materials derived from fluorocarbons in an electrochemical capacitor. In *Advanced fluoride-based materials for energy conversion* (pp. 415–430). Elsevier.
- Simon, P., and Gogotsi, Y. (2008). Materials for electrochemical capacitors. *Nature materials*, 7(11), 845–854.
- Sing, K. S. (1998). Adsorption methods for the characterization of porous materials. *Advances in colloid and interface science*, 76, 3–11.
- Smith, B., Wills, R., and Cruden, A. (2020). Aqueous al-ion cells and supercapacitors — a comparison. *Energy Reports*, 6, 166–173.
- Song, K., Wu, Q., Zhang, Z., Ren, S., Lei, T., Negulescu, I., and Zhang, Q. (2015). Porous carbon nanofibers from electrospun biomass tar/polyacrylonitrile/silver hybrids as antimicrobial materials. *ACS applied materials interfaces*, 7.
- Song, X.-L., Guo, J.-X., Guo, M.-X., Jia, D.-Z., Sun, Z.-P., and Wang, L.-X. (2016). Free-standing needle-like polyaniline-coal based carbon nanofibers composites for flexible supercapacitor. *Electrochim. Acta*, 206, 337–345.
- Steach, J., Clark, J., and Olesik, S. (2010). Optimization of electrospinning an su-8 negative photoresist to create patterned carbon nanofibers and nanobeads. *Journal of Applied Polymer Science - J APPL POLYM SCI*, 118, 405–412.
- Stoller, M. D., and Ruoff, R. S. (2010). Best practice methods for determining an electrode material's performance for ultracapacitors. *Energy & Environmental Science*, 3(9), 1294–1301.
- Storck, J. L., Brockhagen, B., Grothe, T., Sabantina, L., Kaltschmidt, B., Tuvshinbayar, K., Braun, L., Tanzli, E., Hütten, A., and Ehrmann, A. (2021). Stabilization and carbonization of pan nanofiber mats electrospun on metal substrates. *C*, 7(1), 12.
- Tahir, M. B., Abrar, M., Tehseen, A., Awan, T. I., Bashir, A., and Nabi, G. (2020). Chapter 11 - nanotechnology: The road ahead. In T. I. Awan, A. Bashir and A. Tehseen (Eds.), *Chemistry of nanomaterials* (pp. 289–308). Elsevier.
- Tai, Z., Lang, J., Yan, X., and Xue, Q. (2012). Mutually enhanced capacitances in carbon nanofiber/cobalt hydroxide composite paper for supercapacitor. *Journal of The Electrochemical Society*, 159(4), A485.

- Tanapongpisit, N., Wongprasod, S., Laohana, P., Kim, S., Butburee, T., Meevasana, W., Maensiri, S., Bark, C. W., and Saenrang, W. (2022). Effects of the particle size of bamno_3 powders on the electrochemical performance of supercapacitor electrodes. *Materials Letters*, *319*, 132258.
- Tian, X., Zhao, N., Wang, K., Xu, D., Song, Y., Guo, Q., and Liu, L. (2015). Preparation and electrochemical characteristics of electrospun water-soluble resorcinol/phenol-formaldehyde resin-based carbon nanofibers. *RSC Adv.*, *5*, 40884–40891.
- Tibbetts, G. G., Lake, M. L., Strong, K. L., and Rice, B. P. (2007). A review of the fabrication and properties of vapor-grown carbon nanofiber/polymer composites. *Composites Science and Technology*, *67*(7), 1709–1718.
- Tran, C., and Kalra, V. (2013). Fabrication of porous carbon nanofibers with adjustable pore sizes as electrodes for supercapacitors. *Journal of Power Sources*, *235*, 289–296.
- Tyagi, A., and Gupta, R. (2015, June). Carbon nanostructures from biomass waste for supercapacitor applications.
- Vandenbroucke, A. (2015). *Abatement of volatile organic compounds by combined use of non-thermal plasma and heterogeneous catalysis* [Doctoral dissertation, Ghent University].
- Venkatachalam, S., Hall, S., Smith, P., and Bobba, R. (2004). Mesoporous anhydrous ruo_2 as a supercapacitor electrode material. *Solid State Ionics*, *175*, 511–515.
- Vijayakumar, S., Nagamuthu, S., and Muralidharan, G. (2013). Porous nio/c nanocomposites as electrode material for electrochemical supercapacitors. *ACS Sustainable Chemistry & Engineering*, *1*(9), 1110–1118.
- Wang, G., Zhang, L., and Zhang, J. (2012). A review of electrode materials for electrochemical supercapacitors. *Chemical Society Reviews*, *41*(2), 797–828.
- Wang, K., Zhang, W., Phelan, R., Morris, M. A., and Holmes, J. D. (2007). Direct fabrication of well-aligned free-standing mesoporous carbon nanofiber arrays on silicon substrates. *Journal of the American Chemical Society*, *129*(44), 13388–13389.
- Wang, M., Guo, H., Xue, R., Li, Q., Liu, H., Wu, N., Yao, W., and Yang, W. (2019). Covalent organic frameworks: A new class of porous organic frameworks for supercapacitor electrodes. *ChemElectroChem*, *6*(12), 2984–2997.
- Wang, Q., Jian, M., Wang, C., and Zhang, Y. (2017). Carbonized silk nanofiber membrane for transparent and sensitive electronic skin. *Advanced Functional Materials*, *27*, 1605657.

- Wang, W., Guo, S., Lee, I., Ahmed, K., Zhong, J., Favors, Z., Zaera, F., Ozkan, M., and Ozkan, C. (2014). Hydrous ruthenium oxide nanoparticles anchored to graphene and carbon nanotube hybrid foam for supercapacitors. *Scientific reports*, *4*, 4452.
- Wang, W., Xu, D., Cheng, B., Yu, J., and Jiang, C. (2017). Hybrid carbon@TiO₂ hollow spheres with enhanced photocatalytic CO₂ reduction activity. *J. Mater. Chem. A*, *5*, 5020–5029.
- Wu, M. S., and Hsieh, H. H. (2008). Nickel oxide/hydroxide nanoplatelets synthesized by chemical precipitation for electrochemical capacitors. *Electrochimica Acta*, *53*(8), 3427–3435.
- Wu, Z., Zhu, Y., Ji, X., and Banks, C. E. (2016). Transition metal oxides as supercapacitor materials. In K. I. Ozoemena and S. Chen (Eds.), *Nanomaterials in advanced batteries and supercapacitors* (pp. 317–344). Springer International Publishing.
- Xia, K., Gao, Q., Jiang, J., and Hu, J. (2008). Hierarchical porous carbons with controlled micropores and mesopores for supercapacitor electrode materials. *Carbon*, *46*(13), 1718–1726.
- Xiong, D., Li, W., and Liu, L. (2017). Vertically aligned porous nickel (ii) hydroxide nanosheets supported on carbon paper with long-term oxygen evolution performance. *Chemistry–An Asian Journal*, *12*(5), 543–551.
- Xu, W., Xin, B., and Yang, X. (2020). Carbonization of electrospun polyacrylonitrile (pan)/cellulose nanofibril (cnf) hybrid membranes and its mechanism. *Cellulose*, *27*, 3789–3804.
- Yang, K., Edie, D. D., Lim, D., Kim, Y., and Choj, Y. (2003). Preparation of carbon fiber web from electrostatic spinning of pmda-oda poly(amic acid) solution. *Carbon*, *41*(11), 2039–2046.
- Yang, X., Cui, Y., Qi, Y., Fu, L., Rezayan, A., Xu, C. C., Wang, J., Sui, D., and Zhang, Y. (2023). Self-supporting nio-coated activated carbon nanofibers based on atomic layer deposition for supercapacitor. *Journal of Alloys and Compounds*, *958*, 170513.
- Ye, S., and Guan, X. (2019). Hmt-controlled synthesis of mesoporous nio hierarchical nanostructures and their catalytic role towards the thermal decomposition of ammonium perchlorate. *Applied Sciences*, *9*(13), 2599.
- Yu, A., Chabot, V., and Zhang, J. (2013). *Electrochemical supercapacitors for energy storage and delivery: Fundamentals and applications*. Taylor & Francis.

- Yuan, C., Zhang, X., Su, L., Gao, B., and Shen, L. (2009). Facile synthesis and self-assembly of hierarchical porous nio nano/micro spherical superstructures for high performance supercapacitors. *Journal of Materials Chemistry*, 19(32), 5772–5777.
- Zan, L., Yunfeng, C., Yu, G., Javad, F., Yong, Z., Wang, C., Long, H., and Wallace, G. G. (2017). High-performance hybrid carbon nanotube fibers for wearable energy storage. *Nanoscale*, 9, 5063–5071.
- Zhang, C. (, Xie, Y., Zhao, M., Pentecost, A., Ling, Z., Wang, J., Long, D., Ling, L., and Qiao, W. (2014). Enhanced electrochemical performance of hydrous ruo₂/mesoporous carbon nanocomposites via nitrogen doping. *ACS applied materials & interfaces*, 6, 9751.
- Zhang, S.-J., Yu, H.-Q., and Feng, H.-M. (2006). Pva-based activated carbon fibers with lotus root-like axially porous structure. *Carbon*, 44(10), 2059–2068.
- Zhang, Y., Shen, Y., Xie, X., Du, W., Kang, L., Wang, Y., Sun, X., Li, Z., and Wang, B. (2020). One-step synthesis of the reduced graphene oxide@ nio composites for supercapacitor electrodes by electrode-assisted plasma electrolysis. *Materials & Design*, 196, 109111.
- Zhong, C., Yida, D., Hu, W., Qiao, J., Zhang, L., and Zhang, J. (2015). A review of electrolyte materials and compositions for electrochemical supercapacitors. *Chemical Society reviews*, 44, 7431–7920.
- Zhou, Z., Lai, C., Zhang, L., Qian, Y., Hou, H., Reneker, D. H., and Fong, H. (2009). Development of carbon nanofibers from aligned electrospun polyacrylonitrile nanofiber bundles and characterization of their microstructural, electrical, and mechanical properties. *Polymer*, 50(13), 2999–3006.
- Zhou, Z., and Wu, X.-F. (2013). Graphene-beaded carbon nanofibers for use in supercapacitor electrodes: Synthesis and electrochemical characterization. *Journal of Power Sources*, 222, 410–416.
- Zhu, D., Xu, C., Nakura, N., and Matsuo, M. (2002). Study of carbon films from pan/vgcf composites by gelation/crystallization from solution. *Carbon*, 40(3), 363–373.
- Zhu, Z., Ji, C., Zhong, L., Liu, S., Cui, F., Sun, H., and Wang, W. (2017). Magnetic fe-co crystal doped hierarchical porous carbon fibers for removal of organic pollutants. *J. Mater. Chem. A*, 5, 18071–18080.
- Zhu, Z., Xu, Y., Qi, B., Zeng, G., Wu, P., Liu, G., Wang, W., Cui, F., and Sun, Y. (2017). Adsorption-intensified degradation of organic pollutants over bifunctional α -fe@ carbon nanofibres. *Environ. Sci.: Nano*, 4(2), 302–306.

CURRICULUM VITAE

Name : Miss Suchunya Wongprasod

Date of Birth : February 17, 2000

Place of Birth : Nakhon Ratchasima, Thailand

Education :

2022 - 2025 School of Physics, Science, Suranaree University of Technology, Nakhon Ratchasima, Thailand (Master of Science)
Advisor: Assoc. Prof. Dr. Wittawat Saenrang

2018 - 2022 School of Physics, Science, Suranaree University of Technology, Nakhon Ratchasima, Thailand (Bachelor of Science)
Advisor: Assoc. Prof. Dr. Wittawat Saenrang

Awards & Honors :

2021 - 2025 DPST (Development and Promotion of Science and Technology Talents Project, Thai government scholarship)

Publications :

1. Tanapongpisit, N., **Wongprasod, S.** et al. (2022). *Materials Letters*, 319, 132258.
2. Phonsuksawang, P., **Wongprasod, S.** et al. (2024). *Materials Chemistry and Physics*, 3311, 128528.
3. **Wongprasod, S.** et al. (2024). *ACS Applied Nano Materials*, 7(6), 6712-6721.
4. Jindata, W., Musikajaroen, S., Wongpratrat, U., Jaisuk, C., **Wongprasod, S.** et al. (2024). *Applied Physics Letters*, 125(4).
5. Tanapongpisit, N., **Wongprasod, S.** et al. (2024). *Scientific Reports*, 14(1), 27811.
6. Techo, A., Kaewpikul, D., Sata, V., Tanapongpisit, N., **Wongprasod, S.** et al. (2024). *Scientific Reports*, 14(1), 28121.
7. Srikam, S., Laohana, P., Tanapongpisit, N., **Wongprasod, S.** et al. (2025). *Ionics*, 31(5), 5205-5216.
8. Khamsa, S., Ditta, Z. M., Tanapongpisit, **Wongprasod, S.** et al. (2025). *Results in Engineering*, 26, 104784.